

EFFICIENCY CALIBRATION MEASUREMENT AND GEANT SIMULATION  
OF THE DRAGON BGO GAMMA RAY ARRAY AT TRIUMF

by

Dario G. Gigliotti

B.Sc., University of Northern British Columbia, 2000

THESIS SUBMITTED IN PARTIAL FULFILLMENT OF

THE REQUIREMENTS FOR THE DEGREE OF

MASTER OF SCIENCE

in

MATHEMATICAL, COMPUTER, AND PHYSICAL SCIENCES

(PHYSICS)

THE UNIVERSITY OF NORTHERN BRITISH COLUMBIA

December 2004

© Dario G. Gigliotti , 2004

# Abstract

A gamma ray array to detect the characteristic gammas emitted from astrophysically significant, radiative proton and alpha capture reactions, was built as part of the Detector of Recoils And Gammas Of Nuclear reactions (DRAGON) spectrometer at ISAC/TRIUMF. The DRAGON array consists of a collection of 30 hexagonal BGO detectors measuring 7.62 cm long by 5.58 cm across the face. Experiments at DRAGON are affected by background due to unreacted or “leaky beam” which reaches the end detector along with the reaction products of interest. In many cases the cross sections of these reactions are so small that it is impossible to distinguish the reaction recoils from leaky beam by using only the electromagnetic separator (EMS) of DRAGON. Further suppression of leaky beam is achieved by demanding a time coincidence between reaction recoils and the associated gamma emitted from the reaction. To determine the rate of gamma/recoil ion coincidence events it is necessary to have an accurate estimate of the gamma array efficiency. Since it is impossible to measure this rate for all experimental conditions it is necessary to have a simulation which can estimate the efficiency of the array for a given set of experimental parameters (e.g. gamma energy). A simulation was built with the particle-tracking program GEANT v3.21. The efficiency of the array was measured using calibrated sources of various gamma energies and compared to simulated results. For the cases where the activity of the source was not well known the sources were calibrated using a standard NaI detector of known efficiency. The agreement between simulation and measured differences is more than adequate for proposed DRAGON experiments. The analysis and results of the comparison between measured and simulated efficiency will be discussed in this thesis.

# Contents

<b>Abstract</b>	<b>ii</b>
<b>Contents</b>	<b>iii</b>
<b>List of Tables</b>	<b>vii</b>
<b>List of Figures</b>	<b>ix</b>
<b>Acknowledgements</b>	<b>xiii</b>
<b>1 Introduction</b>	<b>1</b>
1.1 Big Bang Nucleosynthesis . . . . .	2
1.2 Hydrogen Burning . . . . .	2
1.3 The CNO Cycle . . . . .	4
1.4 Helium Burning . . . . .	6
1.5 Novae, X-ray Bursters and Supernovae . . . . .	7
1.6 Explosive Hydrogen Burning . . . . .	9
1.6.1 The NeNa and MgAl Cycles . . . . .	9
1.6.2 The Hot CNO Cycle . . . . .	9
1.6.3 The RP-Process . . . . .	12
<b>2 Radiation Spectroscopy with Scintillators</b>	<b>13</b>
2.1 Gamma Ray Interactions with Matter . . . . .	13
2.1.1 Photoelectric Absorption . . . . .	13
2.1.2 Compton Scattering . . . . .	15

2.1.3	Pair Production . . . . .	18
2.2	Scintillation Detector Principles . . . . .	20
2.3	Detector Energy Resolution . . . . .	22
2.4	Modelling the Detector Response . . . . .	24
2.4.1	Definition of the Interaction Length . . . . .	24
<b>3</b>	<b>The DRAGON Facility</b>	<b>30</b>
3.1	Electromagnetic Separator . . . . .	32
3.2	The DRAGON Gamma Ray Array . . . . .	34
3.3	Electronics and Data Acquisition System . . . . .	39
3.4	Dead-Time Correction Using Scalers . . . . .	41
<b>4</b>	<b>Radiative Capture Reaction Rates</b>	<b>43</b>
4.1	Stellar Reaction Rate Defined . . . . .	43
4.2	Non Resonant Reaction Rate . . . . .	44
4.3	Resonant Reaction Rate . . . . .	46
4.4	Experimental Yield . . . . .	48
<b>5</b>	<b>GEANT Simulation</b>	<b>51</b>
5.1	GEANT Background . . . . .	51
5.1.1	Introduction . . . . .	51
5.1.2	GEANT Physics Processes . . . . .	52
5.1.3	Simulating a Physics Process . . . . .	54
5.1.4	Simulating Pair Production by Photons in GEANT . . . . .	57
5.1.5	Simulating Compton Scattering by Photons in GEANT . . . . .	58
5.1.6	Simulating the Photoelectric Effect in GEANT . . . . .	59
5.1.7	Tracking Particles . . . . .	61
5.1.8	GEANT Geometry Package . . . . .	61
5.2	The Simulated DRAGON Gamma Ray Array . . . . .	64
5.2.1	Simulated Radioactive Gamma Source Characteristics . . . . .	68
5.3	Running Simulations . . . . .	70

<b>6</b>	<b>Data Analysis and Results</b>	<b>71</b>
6.1	Efficiency Measurement Technique . . . . .	71
6.2	Gamma Source Activity Calibration . . . . .	72
6.2.1	Fitting By Monte Carlo Methods . . . . .	74
6.2.2	Analysis of NaI Data . . . . .	78
6.3	Efficiency of a Single BGO Detector . . . . .	83
6.3.1	Single Detector Simulation Data . . . . .	86
6.3.2	Single BGO Gamma Ray Photopeak Efficiency Measurements . . . . .	87
6.4	Efficiency of the Full Gamma Ray Detector . . . . .	89
6.4.1	Full Array Simulation . . . . .	89
6.4.2	Photopeak Efficiency Measurements with the Full Gamma Ray Array . . . . .	92
6.4.3	$^{241}\text{Am}^9\text{Be}$ and $^{244}\text{Cm}^{13}\text{C}$ Measurement: Elevated Source . . . . .	97
6.4.4	$^{137}\text{Cs}$ Source Low Energy Measurement . . . . .	99
6.4.5	$^{241}\text{Am}^9\text{Be}$ Source Measurements with all 30 Detectors . . . . .	99
6.4.6	$^{244}\text{Cm}^{13}\text{C}$ Measurement: Source at Beam Position . . . . .	104
6.5	Summary of Error Analysis . . . . .	104
6.5.1	Source Activity Error Analysis . . . . .	110
6.5.2	Single BGO Error Analysis . . . . .	112
6.5.3	Full Array Error Analysis . . . . .	113
6.5.4	GEANT Simulation Error Analysis . . . . .	114
6.6	Re-fitting the Monte Carlo Data . . . . .	115
6.7	Summary of Results . . . . .	121
<b>7</b>	<b>Conclusion</b>	<b>123</b>
7.1	Possible Improvements to the Simulation . . . . .	124
<b>A</b>	<b>Glossary of Selected Terms and Acronyms</b>	<b>136</b>
<b>B</b>	<b>Tabulated Efficiency Data</b>	<b>138</b>

<b>C</b>	<b>Pre Run Gamma Array Setup Procedure</b>	<b>144</b>
C.1	Gain Matching the BGO Detectors . . . . .	144
C.2	Adjusting the Software Threshold . . . . .	147
C.3	Gain Drift . . . . .	150
C.3.1	Temperature Fluctuations . . . . .	150
C.3.2	Operating Voltages . . . . .	152
<b>D</b>	<b>Sample Code</b>	<b>153</b>
D.1	Sample .FFCARDS GEANT Input File . . . . .	153
<b>E</b>	<b>The GEANT Shapes</b>	<b>162</b>

# List of Tables

2.1	Examples of mass attenuation coefficients and interaction lengths for energies between 0.05-6.13 MeV in BGO and NaI . . . . .	26
3.1	Radiative capture reactions of astrophysical significance proposed for DRAGON [1] . . . . .	31
6.1	Source activities of various sources by NaI cross calibration technique. .	75
6.2	Efficiency of a single BGO detector for various gamma ray energies where $\mathcal{E}_D$ denotes the efficiency found from the measurement, $\mathcal{E}_S$ is the efficiency found by GEANT . . . . .	89
6.3	The resulting values of $A$ from refitting the Monte Carlo data to the measured data points . . . . .	115
6.4	Measured photopeak efficiencies. . . . .	122
B.1	Measured and calculated detector efficiencies from the $^{241}\text{Am}^9\text{Be}$ source for the east array half . . . . .	139
B.2	Measured and calculated detector efficiencies from the $^{241}\text{Am}^9\text{Be}$ source for the west array half . . . . .	139
B.3	Measured and calculated detector efficiencies from the $^{241}\text{Am}^9\text{Be}$ source 15 cm above the target . . . . .	140
B.4	Measured and calculated detector efficiencies from the $^{244}\text{Cm}^{13}\text{C}$ source 15 cm above the target . . . . .	141
B.5	Measured and calculated detector efficiencies from the $^{137}\text{Cs}$ source facing east . . . . .	141

B.6	Measured and calculated detector efficiencies from the $^{137}\text{Cs}$ source facing west . . . . .	142
B.7	Measured and calculated detector efficiencies from the $^{244}\text{Cm}^{13}\text{C}$ source facing east . . . . .	142
B.8	Measured and calculated detector efficiencies from the $^{244}\text{Cm}^{13}\text{C}$ source facing west . . . . .	143



# List of Figures

1.1	Energy generation rates for the pp-chain and CNO cycle . . . . .	5
1.2	The CNO cycle [2] . . . . .	5
1.3	Sequence of nuclear reactions and beta-decays involved in the “cold” and “hot” NeNa cycle and the MgAl cycle. [3] . . . . .	10
1.4	The hot CNO cycle [2] . . . . .	11
1.5	The transition from the hot CNO cycle to the rp-process at high tem- peratures. The shaded region comprises the stable nuclei. [4] . . . . .	12
2.1	Energy deposition by monoenergetic gammas interacting by the pho- toelectric effect in an ideal detector (i.e. perfect resolution) [5] . . . . .	15
2.2	The result of the gamma ray and target electron collision in a Compton scattering event. [5] . . . . .	16
2.3	Energy deposition in an ideal (i.e. perfect resolution) detector for in- teractions including solely Compton scattering and photoelectric effect. [5] [6] . . . . .	17
2.4	The energy deposited by a pair production event in an ideal detector. [5] . . . . .	19
2.5	The relative importance of the three major types of gamma ray inter- actions. . . . .	20
2.6	Components of a scintillation detector [5] . . . . .	21
2.7	Amplification of a photon signal in a scintillator by the PMT [7] . . . . .	22
2.8	Example of practical effects to the Compton and photopeak distribu- tion in a real scintillator, for a 0.662 MeV gamma ray . . . . .	24

2.9	Mass attenuation coefficients for BGO and NaI for the energy range 0.05-6.13 MeV . . . . .	26
2.10	Pulse height spectra of practical intermediate sized detectors . . . . .	29
3.1	The DRAGON detector. [8] . . . . .	31
3.2	Radioactive beams from ISAC impinge on a gas target. The heavy ion recoil leaves the target inside a cone $\phi$ defined by the reaction kinematics. . . . .	32
3.3	Leaky beam suppression example . . . . .	35
3.4	One of the gamma ray scintillation detectors composed of a BGO crys- tal coupled to a 51 mm diameter photomultiplier tube. [8] . . . . .	36
3.5	The DRAGON Gamma Ray Array . . . . .	38
3.6	Block diagram of the DRAGON gamma detector electronics. . . . .	39
4.1	The dominant energy-dependent functions for nuclear reactions be- tween charged particles. . . . .	45
4.2	The Maxwell-Boltzmann distribution for a given stellar temperature $T$ and the cross section for a narrow resonance ( $\Gamma \ll E_R$ ) [3] . . . . .	47
4.3	Thick target yield curve . . . . .	50
5.1	Simplified GEANT flow chart [9] . . . . .	53
5.2	GTGAMA block diagram . . . . .	62
5.3	Example of a daughter in a mother volume . . . . .	63
5.4	Three major components of the DRAGON gamma array . . . . .	65
5.5	GEANT DRAGON inner gas target . . . . .	66
5.6	BGO Detectors 2 and 3 shown moved back to allow the lead shielding to be inserted . . . . .	67
5.7	Simulated, individual BGO detectors showing the scintillator material, reflective coating, aluminum casing and PMT . . . . .	68
5.8	Schematic of the simulated BGO array . . . . .	69
6.1	Gamma levels in the ${}^9\text{Be}(\alpha, n){}^{12}\text{C}$ reaction [10] . . . . .	72
6.2	Gamma levels in the ${}^{13}\text{C}(\alpha, n){}^{16}\text{O}$ reaction [11] . . . . .	73

6.3	A photo of the source calibration setup showing the detector stand and source mount. The cylindrical source is visible on the shelf just to the right of the yellow radiation warning sign, 10 cm above the face of the 3" diameter detector. . . . .	74
6.4	Electronics diagram for the NaI scintillator setup . . . . .	75
6.5	High energy sources produce a complicated spectrum of a sum of Gaussian and Compton edges . . . . .	76
6.6	Monte Carlo fitting example . . . . .	79
6.7	Fitting results of the Monte Carlo fitting procedure for NaI source calibration . . . . .	80
6.8	$^{137}\text{Cs}$ spectrum showing regions used in the calculation of pile-up correction. See text for details. . . . .	81
6.9	Comparison of published NaI <i>total efficiency</i> values . . . . .	84
6.10	Comparison of published NaI <i>peak-to-total ratios</i> values of [12] and [13] to GEANT calculation. . . . .	85
6.11	Simulated source centred 10 cm axially from the face of the detector . .	86
6.12	Simulated spectra of pulse height vs. energy for a single BGO detector.	88
6.13	Fitting results for efficiency comparisons of a single BGO detector . . .	90
6.14	Single BGO efficiency measurement comparison between data and simulation . . . . .	91
6.15	Coordinate system used for all measurements of the full array . . . . .	92
6.16	Simulated photopeak efficiency for the DRAGON gamma ray as a function of detector number, where $z = 0$ is the the centre of the gas target	93
6.17	Simulated photopeak efficiency for the DRAGON gamma ray as a function of source position, where $z = 0$ is the centre of the gas target . . .	94
6.18	Lack of symmetry in gamma emittance in “back” of the capsule due to internal attenuation . . . . .	95
6.19	Removing the 10 crowning detectors yields an array symmetric in all three directions . . . . .	97
6.20	$^{241}\text{Am}^9\text{Be}$ and $^{244}\text{Cm}^{13}\text{C}$ sources were suspended 15 cm above the gas target . . . . .	98

6.21	Simulated photopeak efficiency, of east and west halves of the array . . .	99
6.22	A sample Monte Carlo fitting result for the $^{241}\text{Am}^9\text{Be}$ source. . . . .	100
6.23	Efficiency results for the $^{241}\text{Am}^9\text{Be}$ source suspended 15 cm above the target. . . . .	101
6.24	Efficiency results for the $^{244}\text{Cm}^{13}\text{C}$ source suspended 15 cm above the target. . . . .	102
6.25	Efficiency results for the $^{137}\text{Cs}$ source facing each array half. . . . .	103
6.26	Two measurements with the $^{241}\text{Am}^9\text{Be}$ source were necessary. Array detectors have been pulled back by $\approx 31.5$ cm to reduce dead time . . .	105
6.27	Efficiency results for the $^{241}\text{Am}^9\text{Be}$ facing each array half. . . . .	106
6.28	$^{244}\text{Cm}^{13}\text{C}$ source positioning inside the gas target . . . . .	107
6.29	A sample Monte Carlo fitting result for $^{244}\text{Cm}^{13}\text{C}$ source inside the gas target a $z = 0$ . . . . .	108
6.30	Efficiency results for the $^{244}\text{Cm}^{13}\text{C}$ source positioned inside the gas target box. . . . .	109
6.31	Re-fit efficiency results for the $^{241}\text{Am}^9\text{Be}$ facing each array half. . . . .	116
6.32	Re-fit efficiency results for the $^{241}\text{Am}^9\text{Be}$ source suspended 15 cm above the target. . . . .	117
6.33	Re-fit efficiency results for the $^{244}\text{Cm}^{13}\text{C}$ source suspended 15 cm above the target. . . . .	118
6.34	Re-fit efficiency results for the $^{137}\text{Cs}$ source facing each array half. . . . .	119
6.35	Re-fit efficiency results for the $^{244}\text{Cm}^{13}\text{C}$ source positioned inside the gas target box. . . . .	120
C.1	Result of gain matching the 30 BGO detectors . . . . .	148
C.2	2 MeV software threshold placed on a sample spectra from $^{244}\text{Cm}^{13}\text{C}$ . . .	151
E.1	BOX,TRD1,TRD2,TRAP . . . . .	163
E.2	TUBE,TUBS,CONE,CONS . . . . .	164
E.3	SPHE,PARA,PGON,PCON . . . . .	165
E.4	GTRA . . . . .	166

# Acknowledgements

I am fortunate enough to have worked and met with many interesting people over the course of my MSc work but there are two people who I have had the privilege to be both friend and co-worker with.

I could go on for pages about the loyalty and support I have received from my supervisor Ahmed Hussein as far back as my undergraduate years. Although we have had our share of differing opinions and difficult times but outside my family there are few other people's opinions and ideas I respect more than yours, Ahmed. For always being in my corner and being honest with me I would like to say thank-you.

Sometimes when working at a lab like TRIUMF a student can find himself overwhelmed and intimidated by the numbers of intelligent people who are constantly challenging your physics knowledge. If a student has the privilege to work with a person like Joel Rogers to support him it can make things much easier. Your work ethic and dedication to the search for truth is an inspiration to me and something I will always remember. For always being there to answer my questions and encouraging me in this sometimes harsh environment I would like to say thank-you.

I would also like to thank John D'Auria for encouraging me in my work to complete my master's thesis with the DRAGON group. Thanks to Dave Hutcheon and Dave Ottewell for their assistance and guidance while doing my source measurements. To the rest of the DRAGON group and especially to Chris R., Alison, Mike, and Chris W. for the relaxing lunch time conversation. To Aaron for making 2003 at TRIUMF a much more entertaining place to be. To Alan for the interesting conversation during late night DRAGON shifts. Thanks to Shawn and Jonty for some words of encouragement at a crucial time while completing my thesis. Special thanks goes to Dan

Melconian for his assistance with data fitting. Thanks to Peter Gumplinger for his efforts in helping build the gamma array simulation and for handling my constant questions.

I also want to say thanks to somebody very special in my life. Somebody who had to put up with my bad moods and short fuse while I completed my thesis, but was still always supportive. Thanks Sandi.

And of course, most importantly, I will never forget the people who have always been supportive from the beginning. When you have a family like mine you never feel alone or depressed or unappreciated. It is a wonderful feeling when you know that no matter what challenges may come your way in life there will always be somebody you can trust to see you through it. They are the ones who have always stood by me and the ones I could always rely on. They are the ones who will continue to support me in whatever I choose to do in the future. To Mom and Dad and my two brothers Dino and Davide, you are a constant reminder that there really is only one important thing in life...family.

*To my family.*

# Chapter 1

## Introduction

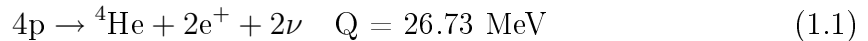
When Galileo produced the first telescope capable of viewing the moons of Jupiter in November of 1609, he succeeded in developing a significant tool with which to collect new astronomical data that was previously unreachable. What we think of today as a modest instrument provided a means of finding evidence to support theories, such as the Copernican system of planetary motion. Galileo's time is regarded by most as the birth of modern astronomy, a field which would later branch out into other fields such as nuclear astrophysics. In more modern times the mechanisms of stellar evolution in the field of stellar nucleosynthesis was pioneered by von Weizsacker [14] [15] and Bethe and Critchfield [16] and was later developed further by Burbidge, Burbidge, Fowler and Hoyle [17] into the present day science of nuclear astrophysics. Some of the questions which still exist about nucleosynthesis in explosive events such as novae, type Ia supernovae and X-ray bursters can be answered by carrying out experiments using the EMS and BGO gamma-ray array of DRAGON. The same scientific quest for truth that drove Galileo to build his telescope still exists today and is why we continue to build new scientific instruments to help us answer the basic question in all physicists minds: "How does that work?"

## 1.1 Big Bang Nucleosynthesis

Shortly after the Big Bang, when the universe expanded and cooled to  $7.5 \times 10^9$  K, the ratio of neutrons to protons froze at a ratio of  $\frac{1}{7}$  [18] until the temperature dropped to  $1 \times 10^9$  K. At this temperature thermonuclear reactions would proceed resulting in the synthesis of  $^4\text{He}$  and, to a much lesser extent, other light nuclides such as  $^2\text{H}$ ,  $^3\text{He}$ , and  $^7\text{Li}$  [3]. Within a few minutes after the light nuclides were produced the universe expanded further so that lower densities and temperatures did not permit the production of heavier elements such as carbon [3]. For the temperatures and densities of Big Bang nucleosynthesis virtually all of the neutrons present would end up in  $^4\text{He}$ . Once the temperature dropped far below  $1 \times 10^9$  K, neutrons were converted into protons or incorporated into  $^4\text{He}$ . At this point nucleosynthesis involving charged particles stopped because thermal energies were not sufficient to overcome the Coulomb barrier. Immediately after the Big Bang what emerged was 75% hydrogen and 23%  $^4\text{He}$  with the remaining 2% being divided among  $^2\text{H}$ ,  $^3\text{He}$ ,  $^6\text{Li}$  and  $^7\text{Li}$ . [19]. To produce elements heavier than  $^7\text{Li}$ , stellar models required [3] a time period of  $10^9$  years after the Big Bang before stellar burning and subsequent explosive nucleosynthesis could proceed.

## 1.2 Hydrogen Burning

Hydrogen burning dominates in first generation stars formed after the Big Bang. The basic hydrogen burning process is [3]



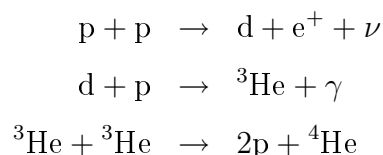
Since the probability of simultaneously fusing four protons in a stellar environment is extremely low, Equation 1.1 proceeds through series of intermediate steps to produce the final alpha particle products. The process governing hydrogen burning in stars is referred to as the proton-proton (pp) chain and it proceeds through three possible reaction chains referred to as p-p-I, p-p-II, and p-p-III. Each chain contributes to overall power generation of a star and in the sun the branching ratios have been



calculated to be 86% for the p-p-I chain, 14% for the p-p-II chain and 0.02% for the p-p-III chain [20] and [21] .

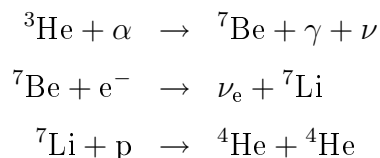
The  $p+p \rightarrow d+e^++\nu$  proceeds through the weak interaction and was proposed by Bethe and Critchfield [16] as a way to explain the apparent impasse of  ${}^4\text{He}$  production brought about by the stable equilibrium of the  $p+p \rightarrow {}^2\text{He}$  reaction and the instability of the  ${}^3\text{Li}$  nucleus. The primary power generating reactions in the sun, the p-p-I chain, is governed by the weak  $p+p \rightarrow d+e^++\nu$  interaction which has a cross section of the order 20 times smaller [3] than cross sections associated with strong interactions. For this reason the slow rate of this reaction dictates the rate at which stars consume their nuclear fuel and is the reason why they still exist today.

The p-p-I chain proceeds through the following set of reactions [3]



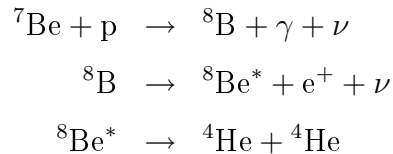
The net result is the conversion of four protons to  ${}^4\text{He}$  and the liberation of  $Q = 26.73$  MeV with 2.0 % of this being lost from the star as it is carried away by the neutrinos. This reduces the effective energy remaining in the stellar interior (i.e. an effective Q-value) due to this set of reactions to 26.20 MeV.

The second chain, the p-p-II chain proceeds through the following set of reactions [3]



Again, the net result is the conversion of 4 protons to  ${}^4\text{He}$  and the liberation of  $Q = 26.73$  MeV but this time 4.0% is lost to the neutrinos resulting in an effective Q-value of 25.66 MeV for this set of reactions.

The p-p-III chain is [3]



Four protons are converted to  ${}^4\text{He}$  and again  $Q = 26.73$  MeV is liberated with 28.3% of the energy being carried away by the neutrinos giving an effective Q-value of 19.17 MeV for this set of reactions.

The star continues to burn its hydrogen fuel until only a  ${}^4\text{He}$  core and a thin outer hydrogen layer is left. This core slowly contracts causing an increase in thermal pressure which pushes the thin hydrogen envelope surrounding the core away from the centre. The thin outer layer is forced to continuously expand until its surface temperature actually falls, shifting the radiation emitted to longer wavelengths and making the star appear red. The star has now reached the Red Giant phase which is the entrance to the helium burning stage, which will be discussed later.

### 1.3 The CNO Cycle

Most of the stars that we see today are second generation, Population I stars [3] that were formed from the elements produced in massive first generation stars whose elements were blown into space at the end of their lives. As a consequence, in the hydrogen burning phase of second generation stars a catalyst,  ${}^{12}\text{C}$ , exists which is involved in a second set of reactions that compete with the pp-chain (See Fig. 1.1). Below  $1.8 \times 10^7$  K the pp-chain dominates but above this temperature the CNO cycle becomes the leading method of energy production.

The favoured set of reactions involve those heavier elements with the smallest Coulomb barrier and the highest abundances. These are carbon and nitrogen as lithium, beryllium and boron do not have the sufficient abundances. Through (p, $\alpha$ ), (p, $\gamma$ ) and beta decay reactions the net result of the CNO cycle is, as in the pp-chain,

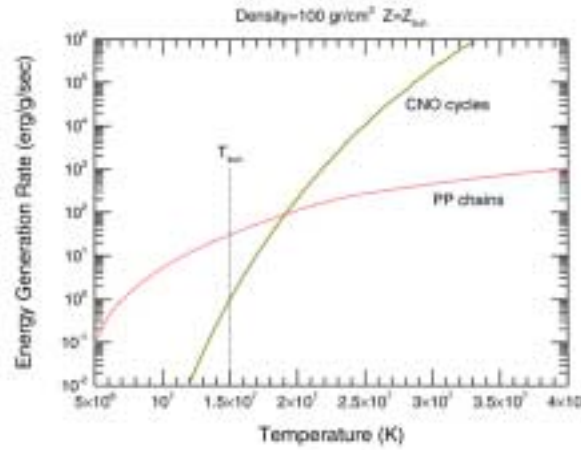


Figure 1.1: Energy generation rates. The rates for the pp-chain and CNO cycle are compared as a function of temperature for Population I stars. Note the crossover at about 18 million K. [22]

a conversion of four protons to produce  ${}^4\text{He}$  with a  $Q = 26.73$  MeV (See Fig. 1.2). The catalyst  ${}^{12}\text{C}$  is formed at the end of the cycle. Recent work [23] has looked at the critical reaction,  ${}^{14}\text{N}(p, \gamma){}^{15}\text{O}$ , which determines the rate of energy production in the CNO cycle.

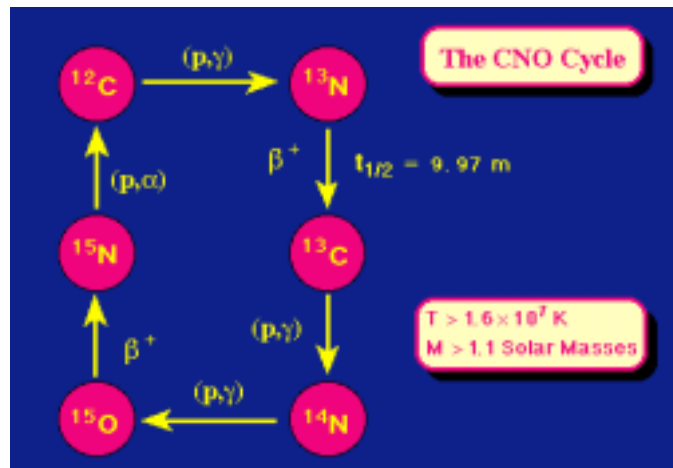


Figure 1.2: The CNO cycle [2]

## 1.4 Helium Burning

Helium burning occurs in massive stars of  $M \geq 0.5M_{\odot}$  where the helium cores reach temperatures of  $T = 1 - 2 \times 10^8$  K and densities of  $\rho = 10^2 - 10^5$  g cm<sup>-3</sup> [3]. Nuclear reactions begin with what is known as the “triple-alpha” reaction where the outcome is  $3\alpha \rightarrow {}^{12}\text{C}$

Although the direct interaction of three alpha-particles is energetically possible, the probability for this direct process is much too small to account for the observed  ${}^{12}\text{C}$  abundances. The solution to this problem was given by Salpeter and Opik [24] who proposed that  ${}^{12}\text{C}$  was formed by a two step process. The first step would be the combination of two alpha-particles to form  ${}^8\text{Be}$ .  ${}^8\text{Be}$  is unstable against decay into two alpha-particles ( $Q = -92.1$  keV) with a lifetime of  $1 \times 10^{-16}$  seconds [25]. Salpeter pointed out that this lifetime is actually long compared to the  $10^{-19}$  second transit time of alpha-particles across a  ${}^8\text{Be}$  nucleus. A small amount of  ${}^8\text{Be}$  is built up from the equilibrium formed between free alpha-particles and  ${}^8\text{Be}$ . The result is that  ${}^8\text{Be}$  can capture an alpha to form  ${}^{12}\text{C}$  and therefore complete the triple-alpha process. Also, Hoyle [26] explained that the only way the triple-alpha process could explain the large abundance of  ${}^{12}\text{C}$  was if alpha capture on  ${}^8\text{Be}$  proceeded through a resonance.

As the  ${}^{12}\text{C}$  is built up by the triple-alpha process it becomes possible to have alpha capture on  ${}^{12}\text{C}$  to create  ${}^{16}\text{O}$ . It is found that  ${}^{12}\text{C}(\alpha, \gamma){}^{16}\text{O}$  burning rate is controlled almost completely by the tails of two sub-threshold resonances which are very difficult to measure [3]. With present experimental uncertainties the reaction rate has been found to vary by factors as large as 10 [27]. Efforts are being made at TRIUMF with DRAGON to measure this reaction rate to better precision.

In principle, the alpha-capture process could continue on  ${}^{16}\text{O}$  to produce  ${}^{20}\text{Ne}$ ,  ${}^{24}\text{Mg}$ ,  ${}^{28}\text{Si}$ , etc., but the increase in the Coulomb barrier and properties of the resonances in the critical energy region for the  ${}^{16}\text{O}(\alpha, \gamma){}^{20}\text{Ne}$  make it impossible [3]. Helium burning will continue in the Red Giant star and the core will continue to contract as fuel is burned. The remnant of the helium burning phase will be a white dwarf, neutron star or black hole depending on the initial mass of the star.

## 1.5 Novae, X-ray Bursters and Supernovae

It has been explained in references [4], [28], [29] and others, that novae outbursts occur as the companion star in a binary system accretes matter onto the degenerate surface of a white dwarf star (which has a mass of the order  $1M_{\odot}$ ) which previously burned all its hydrogen and helium fuel into carbon and oxygen [3] (C-O white dwarf). If the progenitor of the white dwarf was more evolved so that oxygen, neon and magnesium are present (O-Ne-Mg white dwarf), the mass of the white dwarf is in the range  $1.2$ - $1.4M_{\odot}$  [4]. Due to the high gravitational field, matter which falls onto the star travels at high rates resulting in extremely high temperatures on impact. Temperatures in the C-O white dwarf have a peak range of  $1 - 2 \times 10^8$  K and O-Ne-Mg are in the range  $4 - 5 \times 10^8$  K [4]. These temperatures allow runaway fusion reactions to ensue in the accreted layer and the stellar atmosphere erupts violently in a nova explosion which lasts 100-200 s. The energy is released suddenly because the reactions proceed as in a degenerate gas [3]. If a gas was normally ignited it would expand causing the temperature of the gas to drop. Reactions involving degenerate matter proceed at an ever increasing rate which creates the explosion. These explosions can actually happen many times if more material flows from the red giant onto the white dwarf. The period between explosive events is about  $10^3 - 10^5$  years [4].

A similar phenomenon to novae outbursts are X-ray bursts. X-ray bursts also occur in binary star systems except that they differ from novae because the companion star accretes matter onto a neutron star or possibly a black hole rather than a white dwarf [3]. The immense gravitational field of a neutron star (100 billion times that on earth) draws matter from the companion star into an accretion disk. The material in the disk spirals towards the neutron star with such high acceleration that it emits radiation, typically in the X-ray region. Due to the high acceleration the hydrogen rich matter accreting onto the surface of the neutron star will create temperatures which could lead into nucleosynthesis of elements with atomic masses equal to 80 [3]. Typically the X-ray burst event lasts only 5-10 s, but peak temperatures may be in the range of  $7 - 15 \times 10^8$  K. It is believed [4] that X-ray bursts are not strong contributors to galactic abundances because material is not ejected due to high gravitational fields.

Supernovae are split into two classes, supernovae Type I and supernovae Type II. Supernovae of Type I are not associated with the normal stellar evolution of a star but rather with a white dwarf that accretes matter from a companion star in a binary system [3]. In contrast, supernovae of Type II are associated with the explosive deaths of stars in the mass range of  $8\text{-}100M_{\odot}$  [3].

Supernovae of Type I were proposed by Fowler and Hoyle [30] to occur from explosive carbon burning in the degenerate cores. A model proposed in reference [31] described a white dwarf accreting matter from a nearby companion star and igniting hydrogen and helium burning and increasing the mass of the carbon and oxygen core. The carbon eventually ignites and burns outward in a supersonic wave triggering a detonation whereby no remnant is left [3]. The nuclear reactions taking place as the wave moves through the star produce elements up to and including  $^{56}\text{Ni}$  which eventually decay to  $^{56}\text{Co}$  and  $^{56}\text{Fe}$ . Another model described as the deflagration model [32] also involves a wave moving through the star but this time at sub-sonic speeds. The results of this model are the same as the detonation except that the observed abundances of oxygen, silicon and calcium are better explained [3]. There are concerns which may invalidate the deflagration model, such as the required speed of the wave, and at present efforts are being made to explain the mechanism using other means [33].

Red supergiants develop oxygen and carbon in their cores during the normal evolution. At the end of the helium burning cycle the core contracts raising the temperature of the core enough to allow carbon and oxygen to fuse to produce neon and magnesium. Neon, magnesium and oxygen then fuse to produce sulfur and silicon and finally iron. The silicon in the core continues to burn until the mass of iron in the core passes  $1.4M_{\odot}$  (the Chandrasekhar limit) where inward forces of gravity exceed the outward pressure of electron degeneracy and within 0.1 s the core collapses in on itself [34]. A supernova of Type II is initiated. Gamma radiation in the core is energetic enough for photo-disintegration to occur which breaks apart the iron atoms into free protons, neutrons and electrons. Due to the extreme densities, neutronization can occur which combines electrons and protons to form a core composed entirely of neutrons [34]. The layers that surrounded the iron core now fall onto the neutron core at speeds of

15% the speed of light and then bounce back. The shock-wave, caused by the outer layers impacting the neutron core, moves through the star igniting thermonuclear reactions of the hot CNO cycle (described later) on the unburned layers. The material created during the event is released into space. As an example, in the case where the supernova event involves the collapse of a star of  $25M_{\odot}$  the peak temperatures reached in the 5-10 s event are in the range  $2 - 10 \times 10^8$  K [4].

## 1.6 Explosive Hydrogen Burning

### 1.6.1 The NeNa and MgAl Cycles

Stars of  $\approx 8-10M_{\odot}$  can go through a stage of heavy ion burning after they exhaust their helium fuel. In these stars (temperatures  $\approx 7 \times 10^8$  K) carbon-carbon burning takes place ultimately resulting in a white dwarf depleted of carbon and rich in oxygen and neon. If these O-Ne white dwarfs occur in a binary star system the accreting material falls on the dwarf triggering a nova event and igniting proton capture reactions on  $^{20}\text{Ne}$ . The reactions proceed through a set of reactions known as the NeNa and MgAl cycles (See Fig. 1.3). At the peak temperatures ( $1 - 2 \times 10^8$  K) of the nova event proton capture on  $^{21}\text{Na}$  becomes faster than the beta-decay and the “hot” NeNa Cycle is opened (See Fig. 1.3). This reaction caught the interest of the scientific community because  $^{22}\text{Mg}$  beta decays to  $^{22}\text{Na}$  which then beta decays to the first excited state in  $^{22}\text{Ne}$  which promptly decays by the emission of the 1.28 MeV gamma. The 1.28 MeV line should be detectable by orbiting gamma ray observatories providing direct measurements with which to compare to theoretical models. For this reason one of the first radioactive beam experiments performed at DRAGON was the  $^{21}\text{Na}(p, \gamma)^{22}\text{Mg}$  and is of continuing interest [35], [36] and [37].

### 1.6.2 The Hot CNO Cycle

In astrophysical sites such as supermassive stars, supernovae, novae and accreting neutron stars (See §1.5), hydrogen burning takes place at temperatures of  $1 - 15 \times 10^8$  K. At temperatures  $1 - 4 \times 10^8$  K typical of C-O and O-Ne-Mg novae, the dominant

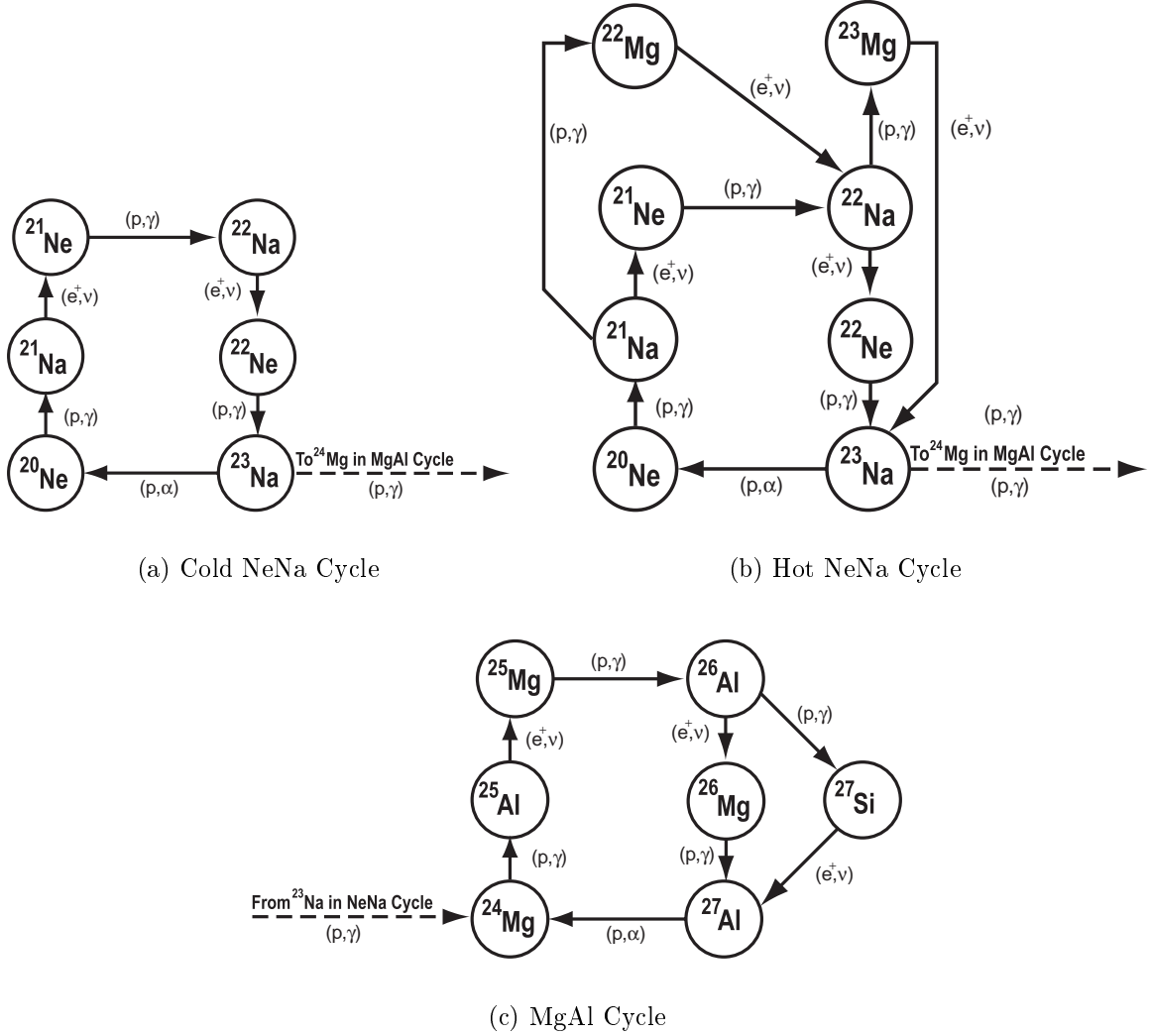


Figure 1.3: Sequence of nuclear reactions and beta-decays involved in the "cold" and "hot" NeNa cycle and the MgAl cycle. [3]



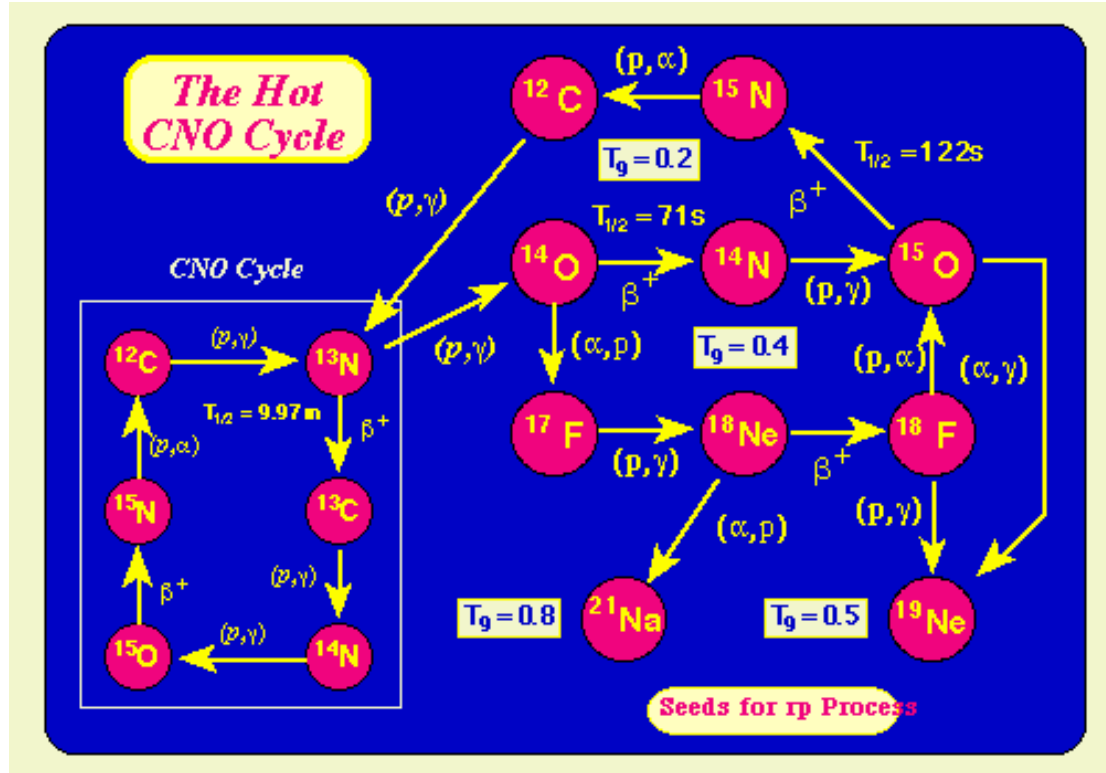


Figure 1.4: The hot CNO cycle [2]

means of energy production is the “hot” CNO cycle [38] because the beta decay of  $^{13}\text{N}$ , in the normal CNO cycle, is bypassed by the  $^{13}\text{N}(p,\gamma)^{14}\text{O}$  reaction. The rate of the hot CNO cycle (See Fig. 1.4 is governed by the lifetimes of  $^{14}\text{O}$  and  $^{15}\text{O}$  ( $T_{1/2} = 71 \text{ s}$  and  $122 \text{ s}$  respectively), rather than the proton capture rate of  $^{14}\text{N}$  as in the CNO cycle. At temperatures approaching  $1 \times 10^5 \text{ K}$  “break-out” from the hot CNO cycle may be possible by alpha-capture reactions on  $^{15}\text{O}$  or  $^{18}\text{Ne}$  [4], or by proton capture on  $^{18}\text{F}$ . Break-out is required in most models to produce elements heavier than  $^{16}\text{O}$ . Measuring the rate of the  $^{15}\text{O}(\alpha,\gamma)^{19}\text{Ne}$  and  $^{18}\text{F}(p,\gamma)^{19}\text{Ne}$  reactions are two key experiments slated for the DRAGON program.

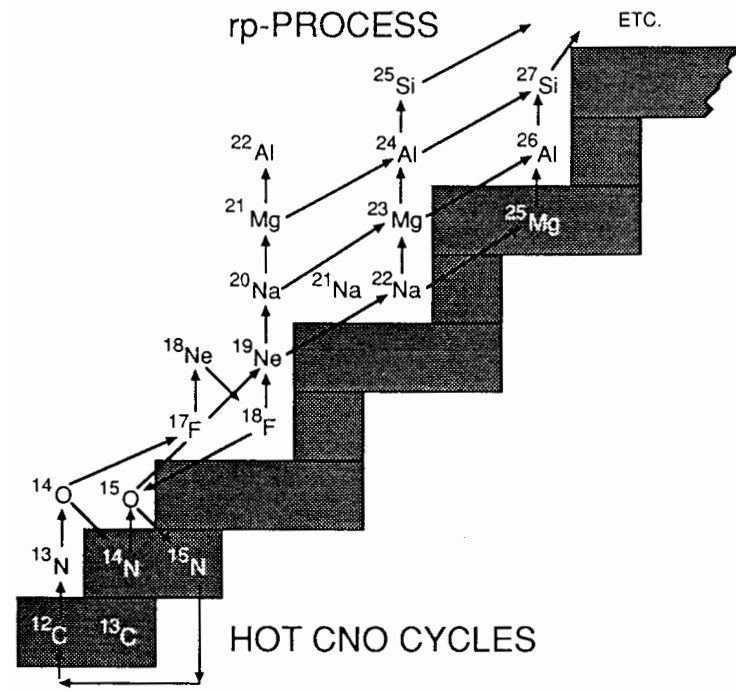


Figure 1.5: The transition from the hot CNO cycle to the rp-process at high temperatures. The shaded region comprises the stable nuclei. [4]

### 1.6.3 The RP-Process

If break-out, via  $^{15}\text{O}(\alpha, \gamma)^{19}\text{Ne}$ ,  $^{18}\text{F}(\text{p}, \gamma)^{19}\text{Ne}$  and  $^{18}\text{Ne}(\alpha, \gamma)^{21}\text{Na}$  reactions, occurs then  $^{19}\text{Ne}$  and  $^{21}\text{Na}$  become catalysts in another series of rapid proton and alpha induced reactions known as the rp-process [38] (See Fig. 1.5). It may also be possible that an rp-process may be triggered by a sufficient pre-explosion abundance of Ne, Na or Mg without being seeded by the hot CNO cycle [4]. The rp-process proceeds along a path between the line of stability and proton drip line (i.e. region of proton-unbound nuclei) where there is a competition between the beta-decay of a nucleus and successive proton captures. As progressively larger masses are formed the rp-process is hindered by an ever increasing Coulomb barrier. Crude estimates of the reaction rates in the rp-process indicate the nucleosynthesis of heavy elements up to and beyond the iron regime are possible [4]. This rate proceeds at 100 times the rate of the hot CNO cycle and may be sufficient to power an X-ray burst [4].

## Chapter 2

# Radiation Spectroscopy with Scintillators

### 2.1 Gamma Ray Interactions with Matter

Gamma rays interact with matter through three important reaction mechanisms that are important in radiation measurement [5]: photoelectric absorption, Compton scattering, and pair production. Through each of these processes gamma rays convert their energy, either partially or fully, to the mass of the electron and its kinetic energy. Cross sections for these processes are the fundamental properties with which gamma detector systems are built.

#### 2.1.1 Photoelectric Absorption

The photoelectric effect involves the absorption of a photon by an atomic electron with the subsequent ejection of the electron (i.e. photoelectron) from the atom [39].

$$\gamma + \text{atom} \rightarrow \text{ion} + e^{-} \quad (2.1)$$

This process is the predominant mode of interaction for gamma rays of relatively low energies of 100 keV or less.

For gamma rays of sufficient energy, the most probable origin of the photoelectron is the most tightly bound electron of the K shell of the atom. The energy of the ejected photoelectron is given by [5],

$$E_{e-} = h\nu - E_b \quad (2.2)$$

where  $E_b$  is the binding energy of the photoelectron in its original shell. Since a free electron cannot absorb the energy of a photon and still conserve momentum the interaction must happen with bound electrons, with the nucleus absorbing the recoil momentum [39]. As a result of the photoelectron leaving the medium an ionized atom with a vacancy in one of its bound shells is left. As this is an unstable situation the vacancy in the shell of the atom is filled by capture of a free electron from the medium and/or rearrangement of electrons from other shells of the atom. The net effect of photoelectric absorption is the liberation of a photoelectron, with energy equal to the kinetic energy of the incident photon minus the binding energy of the electron in its original shell. The binding energy is released in the form of X-rays or Auger electrons. (e.g. In iodine a characteristic X-ray is emitted for about 88% of the absorptions [40]) The characteristic X-rays are re-absorbed through less tightly bound electron shells of the absorber atom. Thus, the overall effect of photoelectric absorption is the liberation of a photoelectron, which carries off most of the gamma ray energy, together with one or more low-energy electrons corresponding to absorption of the original binding energy of the photoelectron. For large detectors nothing escapes from the detector so, the sum of the kinetic energies of the electrons that are created must equal the original energy of the gamma ray photon [5].

Because there is a one to one relationship between the incoming gamma energy and the kinetic energy of the photoelectrons, the photoelectric effect is a very good way to measure gamma energies. If, for example, we were using monoenergetic gammas then one would expect the differential distribution of electron kinetic energy from a series of absorption events would look like Fig. 2.1.

The cross section for the photoelectric effect is dependent on the atomic number of the absorbing material as well as the energy of the incoming gamma ray. No analytic expression exists which describes the cross section for the photoelectric effect at all

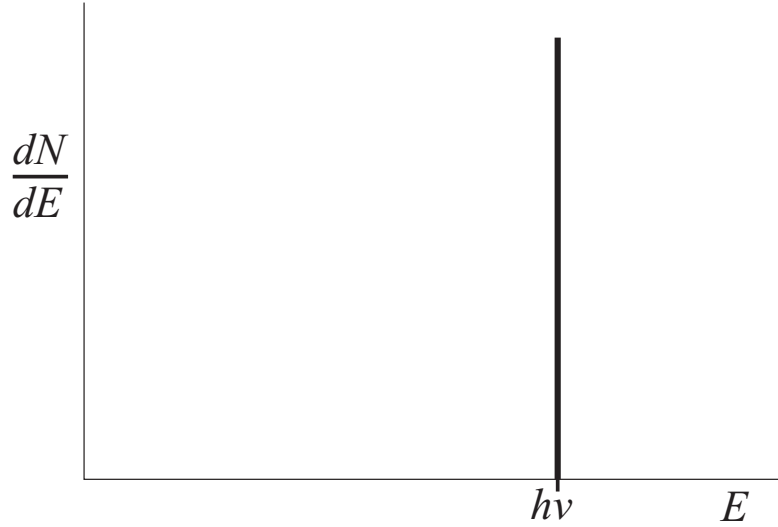


Figure 2.1: Energy deposition by monoenergetic gammas interacting by the photoelectric effect in an ideal detector (i.e. perfect resolution) [5]

energies, but in the MeV range the cross section can be approximated by [5],

$$\sigma_{\text{photo}} \propto \frac{Z^n}{E_\gamma^{3.5}} \quad (2.3)$$

where the exponent  $n$  varies between 4 and 5 [5]. Numerical approximations for the cross sections can be made for use in gamma ray related simulations. More details on this is given in §5.1.6.

### 2.1.2 Compton Scattering

Compton scattering takes place between the incident gamma ray photon and an electron in the absorbing material. It is most often the predominant interaction mechanism for gamma ray energies typical of radioisotope sources [5]. When the gamma ray collides with one of the loosely bound outer electrons of the absorbing material, it is scattered by an angle  $\theta$ . For this reason the gamma photon may transfer a fraction of its energy to the electron. The scattered electron is called the *recoil electron*.

$$\gamma + e^- \rightarrow \gamma + e^- \quad (2.4)$$

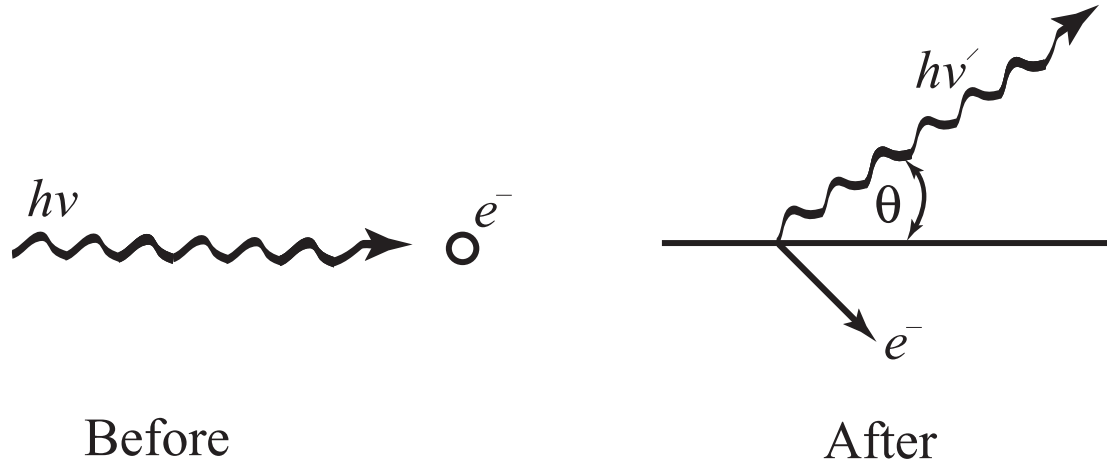


Figure 2.2: The result of the gamma ray and target electron collision in a Compton scattering event. [5]

By referring to Fig. 2.2 and by using conservation of energy and momentum it can be shown [41] that

$$h\nu' = \frac{h\nu}{1 + \frac{h\nu}{m_0c^2}(1 - \cos \theta)} \quad (2.5)$$

where  $m_0c^2$  is the rest-mass energy of the electron (i.e. 0.511 MeV). The kinetic energy of the recoil electron is therefore

$$E_{e^-} = h\nu - h\nu' \quad (2.6)$$

$$= h\nu \left[ \frac{(h\nu/m_0c^2)(1 - \cos \theta)}{1 + (h\nu/m_0c^2)(1 - \cos \theta)} \right] \quad (2.7)$$

As we can see from Equation (2.7) it is not possible that all the gamma energy is transferred to the electron.

The probability of Compton scattering from the passage of gammas through the absorber is dependent on the density of electrons available to scatter from. The amount of target electrons increases linearly with increasing  $Z$  [5]. The angular dependent differential cross section of Compton scattering is expressed by the *Klein-Nishina formula* [42]

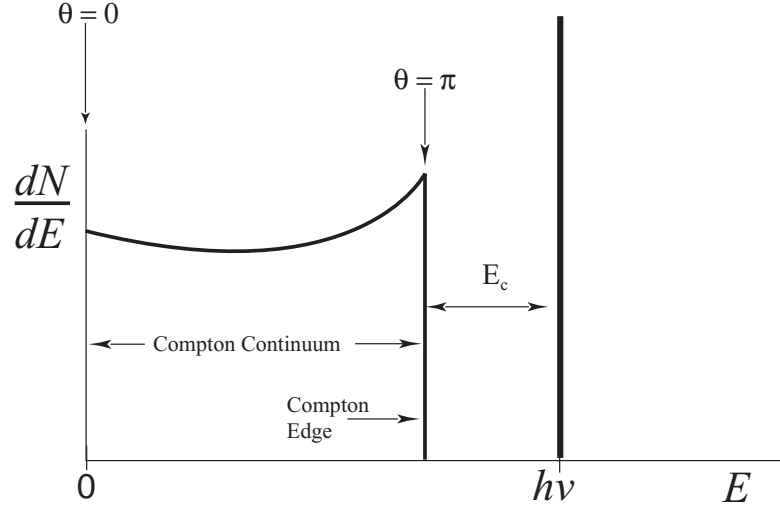


Figure 2.3: Energy deposition in an ideal (i.e. perfect resolution) detector for interactions including solely Compton scattering and photoelectric effect. [5] [6]

$$\frac{d\sigma}{d\Omega} = Zr_0^2 \left[ \frac{1}{1 + \alpha(1 - \cos \theta)} \right]^2 \left[ \frac{1 + \cos^2 \theta}{2} \right] \left[ 1 + \frac{\alpha^2(1 - \cos \theta)^2}{(1 + \cos^2 \theta)[1 + \alpha(1 - \cos \theta)]} \right] \quad (2.8)$$

where  $\alpha = \frac{h\nu}{m_0c^2}$  and  $r_0$  is the classical electron radius.

Integrating over  $d\Omega$  gives the cross section for Compton scattering as [39]

$$\sigma_{\text{comp}} = 2\pi r_0^2 \left\{ \frac{1 + \alpha}{\alpha^2} \left[ \frac{2(1 + \alpha)}{1 + 2\alpha} - \frac{1}{\alpha} \ln(1 + 2\alpha) \right] + \frac{1}{2\alpha} \ln(1 + 2\alpha) - \frac{1 + 3\alpha}{(1 + 2\alpha)^2} \right\} \quad (2.9)$$

If a gamma enters a crystal and interacts solely by the photoelectric effect and Compton scattering the differential distribution versus gamma energy would look like Fig. 2.3, for the ideal situation in which we assumed that the recoil electrons were originally free.

From equations Equation (2.5) and Equation (2.7) two extreme cases can be identified:

1. The angle  $\theta$  is small (i.e. close to zero). This would mean that the scattered gamma ray has nearly the same amount of energy as the incident one, and the recoil Compton electron has very little energy.
2. The angle  $\theta$  is equal to  $\pi$ . Here, the incident gamma recoils in the direction from which it came and the electron is scattered in the forward direction. This extreme represents the maximum energy which can be imparted to the photo-electron

### 2.1.3 Pair Production

If the gamma ray entering the absorbing material exceeds twice the rest mass energy of the electron (i.e. 1.022 MeV) then pair production becomes possible. When a gamma ray of at least 1.022 MeV enters the Coulomb field of a nucleus it is converted into a positron and an electron.

$$\gamma + \text{nucleus} \rightarrow e^+ + e^- + \text{nucleus} \quad (2.10)$$

The interaction must happen in the presence of a nucleus to conserve momentum. If the photon energy exceeds 1.022 MeV the excess energy is shared between the positron/electron pair. The kinetic energy of the positron/electron pair is given by,

$$E_{\text{pair}} = h\nu - 2m_0c^2 \quad (2.11)$$

These two particles travel through the bulk of the absorbing material before the positron loses enough energy to annihilate with an electron and create two 511 keV photons.

The cross section of pair production per nucleus will vary as follows,

$$\sigma_{\text{pair}} \propto Z^2 \quad (2.12)$$

where  $Z$  is the atomic number of the absorber. Numerical approximations for the cross section can be made for use in gamma ray related simulations. More details on this are given in §5.1.4.



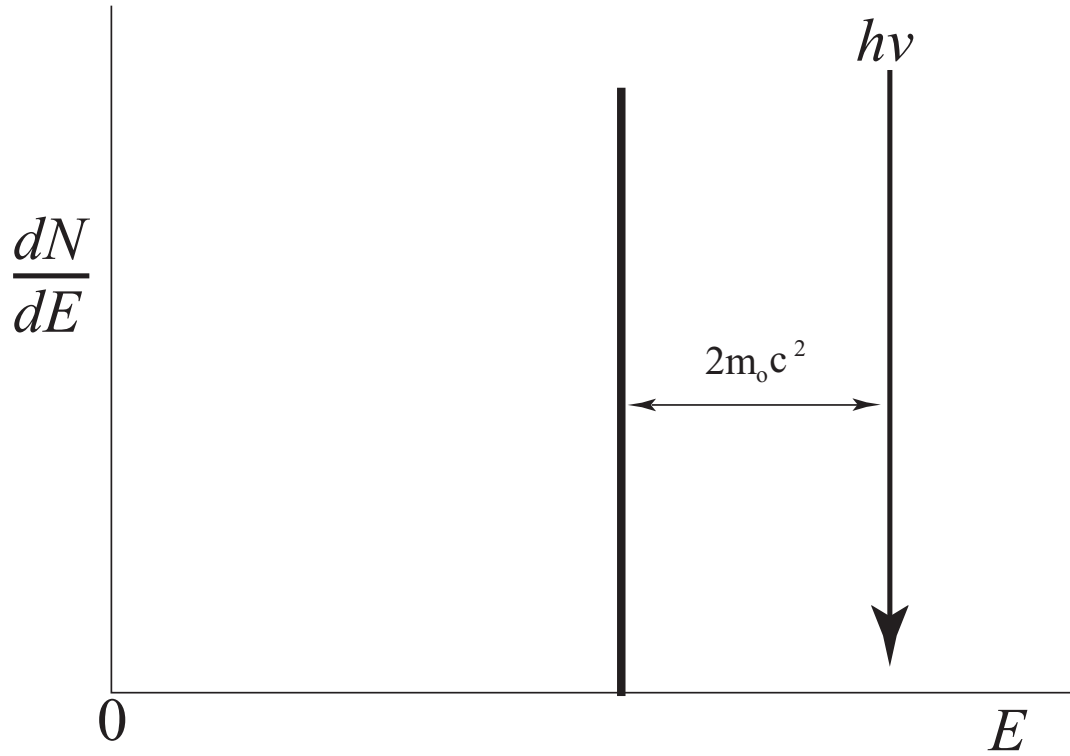


Figure 2.4: The energy deposited by a pair production event in an ideal detector. [5]

As with the photoelectric effect the energy that the pair deposit is given (in an ideal detector) by a delta function as seen in Fig. 2.4. Of particular note is that the energy deposited is now located  $2m_0c^2$  below the incident gamma ray energy. This will be described in more detail in §2.4.1.

The relative importance of the three processes described above (i.e. photoelectric effect, Compton scattering and pair production) for different absorber materials can be illustrated by Fig. 2.5. The line at the left represents the energy at which photoelectric absorption and Compton scattering are equally probable as a function of the absorber atomic number. The line at the right represents the energy at which Compton scattering and pair production are equally probable. The three areas are thus defined on the plot within which photoelectric absorption, Compton scattering, and pair production each predominate [5]

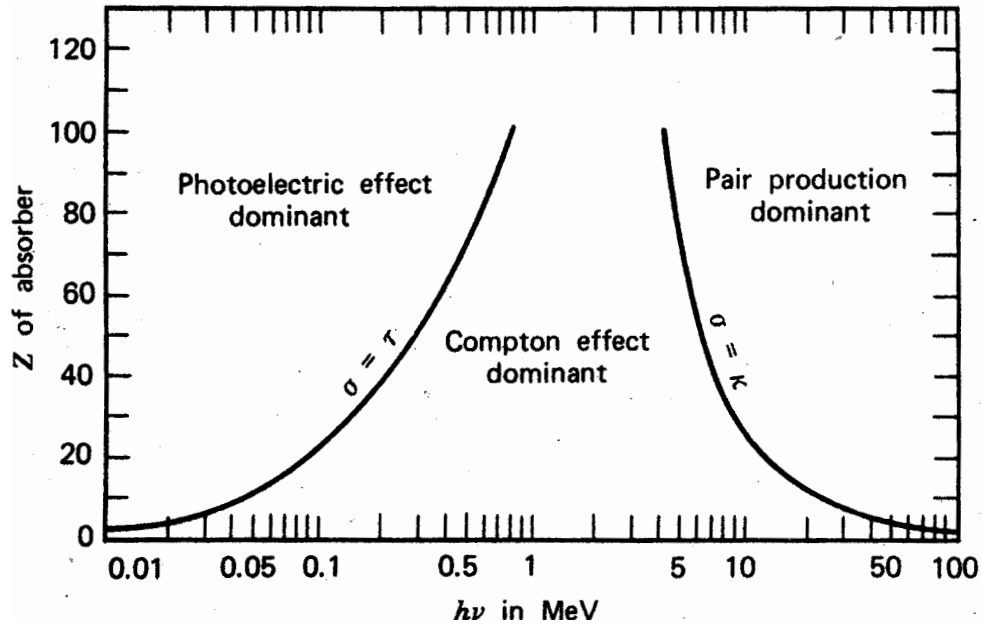


Figure 2.5: The relative importance of the three major types of gamma ray interactions. The lines show the values of  $Z$  and  $h\nu$  for which the two neighbouring effects are just equal. [41]

## 2.2 Scintillation Detector Principles

The basic components of a scintillation detector, Fig. 2.6 are a scintillating material which is optically coupled to a photomultiplier tube (PMT) either directly or through a light guide. As radiation passes through the scintillator, it creates energetic electrons which in turn excite the atoms and molecules making up the scintillator causing light to be emitted. This light is then transmitted to the PMT through the light-coupling system (designed to pass the light with minimum losses) where it is converted into a weak current of photoelectrons, via the photoelectric effect, which is then further amplified by an electron multiplier structure in the tube. Photoelectrons are accelerated toward a dynode maintained at a positive potential relative to the photocathode and the energy gained by the electron results in the ejection of more than one electron upon impact on the dynode, see Fig. 2.7. The process is repeated for a series of dynodes producing more and more electrons (i.e. a cascade) and resulting in signal amplification. The efficiency of light collection by the photocathode is independent of

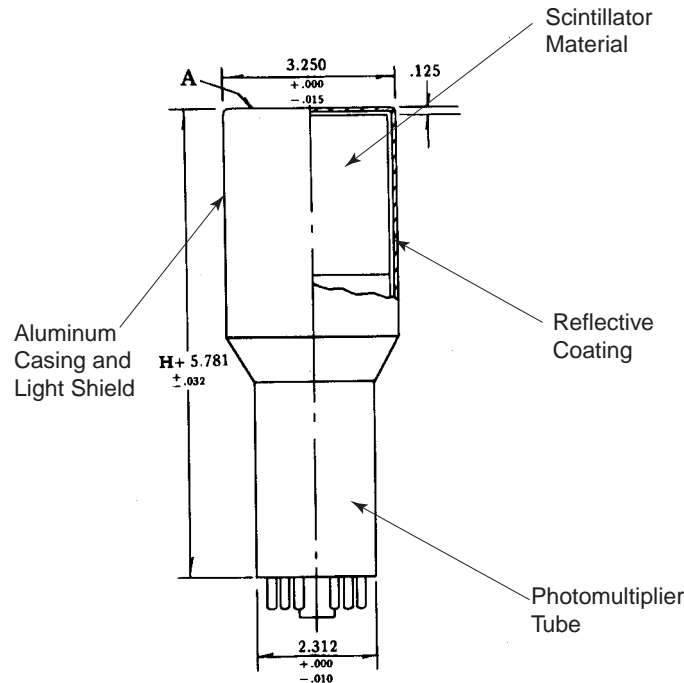


Figure 2.6: Components of a scintillation detector [5]

the location of the pulse in the crystal, and the same number of electrons are emitted from the photocathode for each photon striking it, so the output pulse-height is proportional to the scintillation intensity. Electron amplification by the photomultiplier tube is  $10^5$  to  $10^7$  [7], depending on the dynode voltage. The resulting current signal is then analyzed by a data acquisition system containing an ADC for each PMT.

Scintillators have a property known as *luminescence*. Luminescent materials, when exposed to certain forms of energy, for example, light, heat, radiation (e.g. gamma rays) absorb and re-emit the energy in the form of visible light. If the re-emission occurs immediately after, or almost immediately after, the absorption process is called *fluorescence*. If the re-emission is delayed then *phosphorescence* or *afterglow* occurs. Phosphorescence corresponds to the emission of longer wavelength light than fluorescence, and with a characteristic time that is generally much longer. Afterglow occurs due to the existence of a metastable state in the molecules of the material. This delay time between absorption and re-emission is characterised by a decay constant

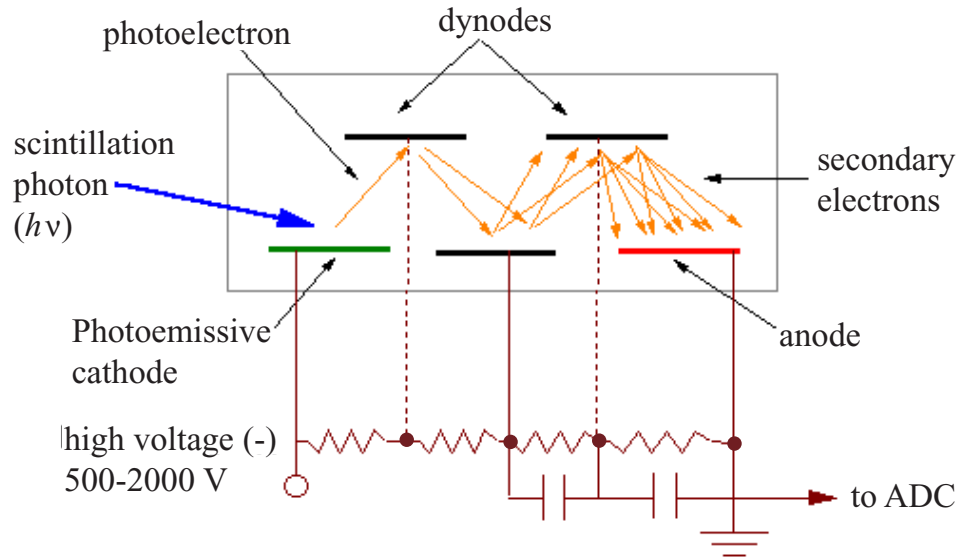


Figure 2.7: Amplification of a photon signal in a scintillator by the PMT [7]

$\tau$ , different for each scintillator material.

Although there are many scintillation materials which exist, not all of them are suitable for the purposes of radiation detection. A good scintillator should have the following characteristics:

1. High efficiency for the conversion of incoming radiation to scintillation light.
2. High efficiency light collection and transfer of photons to the photocathode.
3. A matching of scintillation light wave length to the cathode of existing PMT's.
4. A short decay constant  $\tau$ , appropriate to the experiment's need for accurately timing the gamma ray's arrival.

## 2.3 Detector Energy Resolution

The energy resolution of a scintillation detector measures the ability to distinguish two gamma rays closely spaced in energy. Resolution is quantified by the standard

deviation, or full width at half maximum (FWHM) of the full energy peak or photopeak in a spectrum (such as in Fig. 2.8) divided by the mean peak position on the pulse-height scale [12]. The photopeak is the part of the spectrum that represents gamma rays that have been fully absorbed in the crystal by interaction through the photoelectric effect. The resolution is typically expressed as a percentage. For example, the signals from a 1000 channel ADC are histogrammed in a pulse height versus count spectrum; then a photopeak with a FWHM of 12 channels, with a mean position at channel 100 would give a resolution equal to 12%. The resolution of a detector is primarily due to statistical fluctuations in scintillation photon and photoelectron numbers following the initial event which produces ionization in the detector [12]. These effects include:

1. Conversion of the gamma energy to scintillation light,
2. Efficiency of light collection and transfer of photons to the photocathode,
3. Efficiency of the photocathode in the conversion of photons to photoelectrons,
4. Efficiency of the electron optics in the phototube to focus the photoelectrons onto the secondary-electron-emitting dynode,
5. Electron multiplication in the dynode structure,

These effects mean that the detector response does not exactly resemble the ideal situations described previously and shown in Fig. 2.1, Fig. 2.3 and Fig. 2.4. Fig. 2.8 shows an actual spectrum of relative count rate vs. PMT pulse-height. Here we can see the energy resolution effects broaden the photopeak and Compton edge. All counts to the right of the peak in Fig. 2.8 are pile-up events. Pile-up may also occur in the region to the left of the peak but these events are not possible to distinguish from real events. Pile-up occurs when two photons arrive in a scintillator with a time separation that is short compared to the response of the scintillator or the resolving time of the pulse-processing electronics that follow.

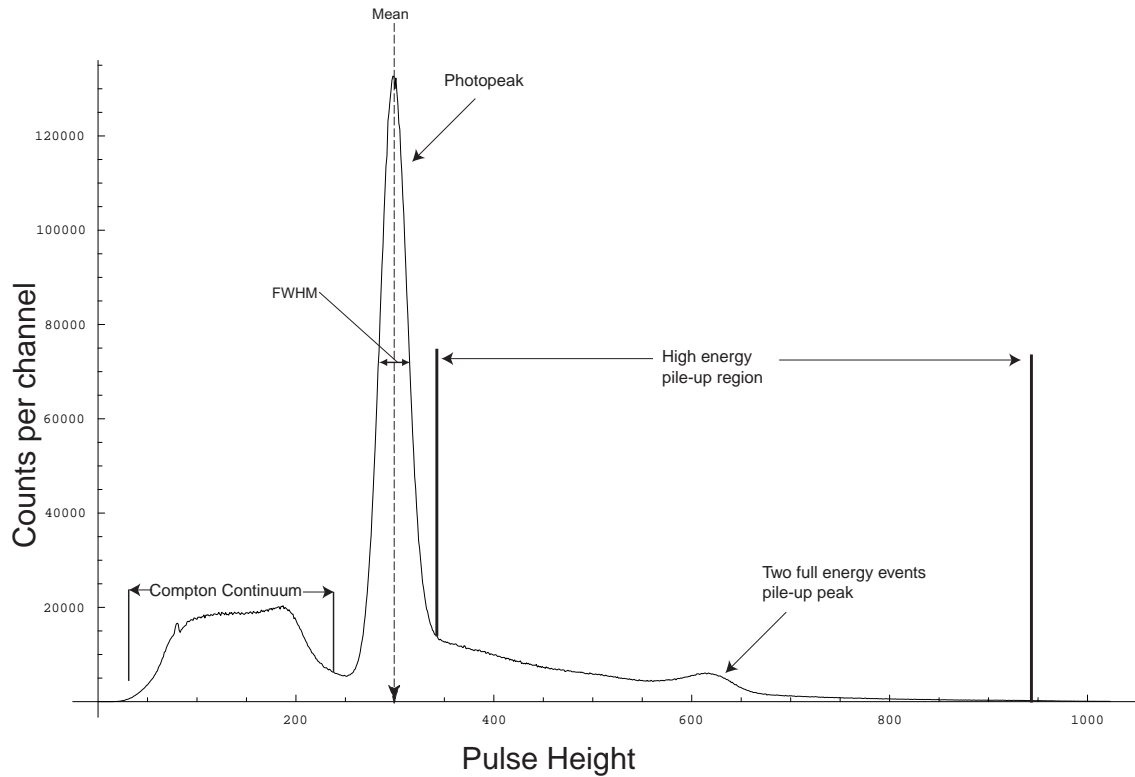


Figure 2.8: Example of practical effects to the Compton and photopeak distribution in a real scintillator, for a 0.662 MeV gamma ray

## 2.4 Modelling the Detector Response of Various Scintillators

### 2.4.1 Definition of the Interaction Length

In describing the size of scintillators an important quantity is the *interaction length* (also known as the absorption length). A beam of monoenergetic gamma rays will be exponentially attenuated by any absorber as a function of its thickness. Each of three interaction processes (photoelectric effect, Compton scattering or pair production) remove the gamma rays from the beam either through scattering or absorption, with a fixed probability of occurrence per unit length. The sum of these probabilities [5],

$$\mu = \tau_{\text{photoelectric}} + \sigma_{\text{Compton}} + \chi_{\text{pair}} \quad (2.13)$$

is called the linear attenuation coefficient. To avoid complications where the density of the absorber varies, the quantity called the mass attenuation coefficient defined as [5],

$$\mu_m = \frac{\mu}{\phi} \quad (2.14)$$

where  $\phi$  is density of the absorber, is more commonly used in place of  $\mu$ . In a compound or mixture such as BGO the mass attenuation coefficient can be calculated from [5],

$$\left(\frac{\mu}{\phi}\right)_c = \sum_i w_i \left(\frac{\mu}{\phi}\right)_i \quad (2.15)$$

The attenuation of the beam of gamma rays can then be expressed in terms of the mass attenuation coefficient  $\mu_m$ , the absorber thickness  $t$  and the density of the material by [5],

$$\frac{I}{I_0} = e^{-\mu_m \phi t} \quad (2.16)$$

The average distance the gamma rays travel within an absorber  $\lambda_m$ , called the *interaction length* or absorption length can then be defined as the reciprocal of the mass attenuation coefficient [5],

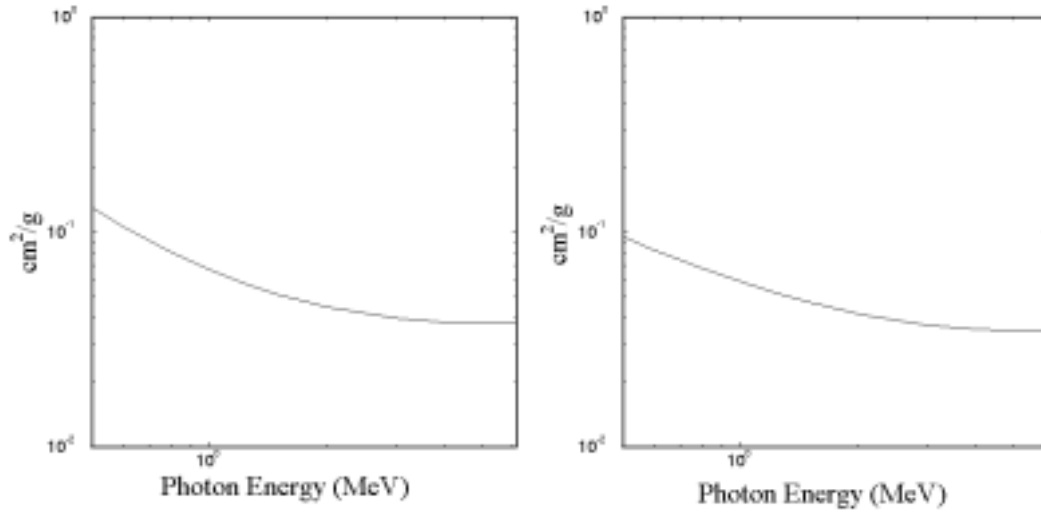
$$\lambda_m = \frac{\phi}{\mu} = \frac{1}{\mu_m} \quad (2.17)$$

Table (2.1) gives examples of how  $\lambda_m$  varies in BGO and NaI as a function of the mass attenuation coefficient, and it illustrates that a NaI crystal would need to be about two times larger than a BGO crystal to have the same efficiency. Fig. 2.9 shows how the mass coefficients of BGO and NaI vary over the range of energies used throughout this work.

Detectors exposed to gamma radiation can be classified according to their interaction (or absorption) length. On one extreme, “small” detectors have very short interaction lengths, which means that the probability of full energy deposition of an

Energy (MeV)	$\mu_m$ (cm <sup>2</sup> /g) BGO	$\lambda_m$ (cm) BGO	$\mu_m$ (cm <sup>2</sup> /g) NaI	$\lambda_m$ (cm) NaI
0.050	5.640	0.025	10.500	0.026
0.511	0.127	1.104	0.093	2.920
0.662	0.096	1.469	0.077	3.557
1.170	0.060	2.357	0.054	5.093
1.130	0.055	2.564	0.050	5.461
1.800	0.047	3.003	0.043	6.307
4.440	0.038	3.730	0.035	7.807
6.130	0.038	3.720	0.035	7.807

Table 2.1: Examples of mass attenuation coefficients and interaction lengths for energies between 0.05-6.13 MeV in BGO and NaI



(a) Mass attenuation coefficient for BGO

(b) Mass attenuation coefficient for NaI

Figure 2.9: Mass attenuation coefficients for BGO and NaI for the energy range 0.05-6.13 MeV



incoming gamma ray is very low, and the probability of escape of annihilation photons is high. At the other extreme, “large” detectors have long interaction lengths, which means that the probability of full energy deposition of an incoming gamma ray is high, and the probability of escape of annihilation photons is low. In between these two extremes are “intermediate” detectors which have interaction lengths that are more typical of the detectors used in gamma ray spectroscopy. Some typical scintillators are NaI with an absorption length of  $\approx 8$  cm at  $E_\gamma = 6$  MeV, plastic scintillator with  $\approx 43$  cm at  $E_\gamma = 6$  MeV, and BGO with  $\approx 3.5$  cm at  $E_\gamma = 6$  MeV.

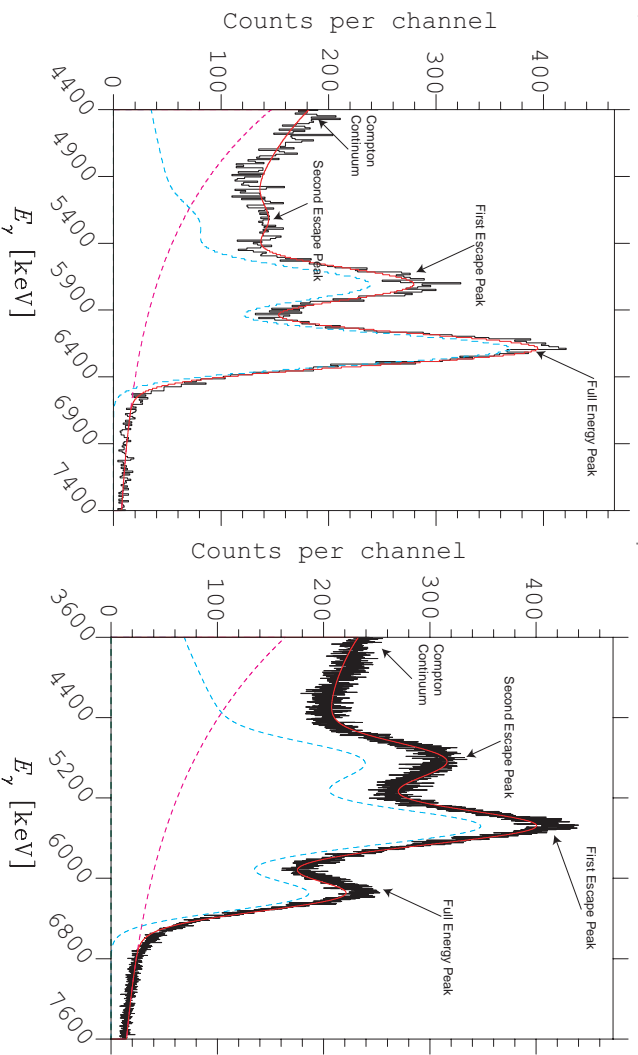
In the small detectors the probability that secondary radiation will escape the detector is high enough so that the ratio of the area under the photopeak to the area under the Compton continuum is small. Most incoming radiation will enter the crystal and undergo one or more Compton scattering events and then exit the crystal without ever interacting by the photoelectric effect. The result is that these events will only contribute to the Compton continuum and no full energy photopeak events will be seen. On more rare occasions it is possible that after several Compton scattering events a photoelectric interaction may take place and this will contribute to the full energy photopeak. By definition, the probability that the incoming gamma ray will immediately interact by the photoelectric effect when entering the crystal, is very low for small detectors. In addition, if the energy of the incident gamma is high enough for pair production to occur then only the kinetic energy of the electron and positron are deposited in the detector and the secondary annihilation radiation escapes. The net effect is to add a *double escape peak* in the spectrum lying on top of the Compton continuum at an energy of  $2m_0c^2$  below the photopeak.

In large detectors the photon will undergo several interaction lengths so the probability of escape of either primary or secondary radiation is very low. A typical event may be a single photoelectric event depositing all energy or a combination of pair production events, Compton scattering events, and a photoelectric absorption. Because the primary and secondary gamma rays travel at the speed of light in the medium the total time for an event to occur would be on the order of less than a nanosecond [5]. This time is much less than the inherent response time of most practical detectors so in essence the pair production, Compton events, and photoelectric absorption will be

collected as one event. Therefore, the pulse produced is a sum of the energies of the electrons produced by each interaction and is proportional to the full energy of the incident photon. In the end, the pulse produced looks as though a single full energy photoelectric absorption occurred. The spectrum would in general look like Fig. 2.1, before adding energy-resolution effects.

In the middle of these two extremes exist most typical detectors. For a typical detector the ratio of the area under the photopeak to area under the Compton continuum is a combination of small and large detector results. Whether they behave more like a small detector or a large detector is dependent on the incoming gamma ray energy. For example, as the incident gamma energy decreases, the detector behaves more like a large detector and the ratio of photopeak to Compton area becomes large. If the energy of the incident radiation is high enough to allow pair production, a more complicated situation may occur. The annihilation photons may either be both absorbed, only one may be absorbed, or both may escape. If both escape, the effect is a *double escape peak* as was mentioned above for small detectors. If only one annihilation photon escapes the effect would be another peak, a *single escape peak* at an energy  $m_0c^2$  below the full energy peak. In still other cases the annihilation photons may undergo Compton scattering and then escape, and contribute to the Compton continuum in the region between the double escape peak and full energy peak.

One should remember that the interaction length is not only dependent on the size of the scintillator but on the density as well. For example, two scintillators one of sodium iodide (NaI) and one bismuth germanate (BGO) [43] of similar size, will have different responses due to their different densities. Typically one sees two escape peaks in NaI much more prominently than in BGO. See Fig. 2.10.



(a) Response of BGO scintillator to 6.13 MeV radiation

(b) Response of NaI scintillator to 6.13 MeV radiation

Figure 2.10: Pulse height spectra of practical intermediate sized detectors

## Chapter 3

# The DRAGON Facility

DRAGON (See Fig. 3.1), the Detector of Recoils And Gammas Of Nuclear reactions was built to measure radiative proton and alpha capture reactions of astrophysical significance (See Table (3.1)). Both radioactive and stable isotope beams are delivered to DRAGON by the TRIUMF Isotope Separator and ACcelerator (ISAC) at any energy from 0.153 to 1.53 MeV/u [44]. It is necessary to measure the reactions in inverse kinematics because it would be impossible to assemble a target of the radioactive isotopes of interest due to their short half lives. Instead, accelerated radioactive beams from ISAC impinge on a differentially pumped windowless gas target, circulating helium or hydrogen, positioned at the “head” (See Fig. 3.1) of DRAGON. The momentum of the incoming beam particles is essentially the same as the recoil, differing slightly due to the emission of the gamma ray (See Fig. 3.2). Because of the reaction kinematics, both unreacted beam AND recoils enter the separator. This, combined with the small reaction cross sections, requires a separator to suppress the higher intensity beam particles from the lower intensity recoils, with a suppression factor of  $\approx 10^{-12}$  or less [1].

The target contains a solid state detector that measures the rate of elastic scattering by detecting hydrogen or helium recoil ions [8]. With a knowledge of the gas pressure, this rate can be used as a normalization of the beam current. Surrounding the gas target is an array of 30 hexagonal BGO crystals to detect the characteristic gammas emitted from the capture reactions.

Reaction	Astrophysical Process	Comments	Proposal
$^{15}\text{O}(\alpha, \gamma)^{19}\text{Ne}$	Hot CNO Break-out		E813
$^{13}\text{N}(\text{p}, \gamma)^{14}\text{O}$	Hot CNO Cycle	data exists	E805
$^{17}\text{F}(\text{p}, \gamma)^{18}\text{Ne}$	Hot CNO Cycle	upper limit	
$^{19}\text{Ne}(\text{p}, \gamma)^{20}\text{Na}$	Hot CNO Cycle	upper limit	
$^{18}\text{F}(\text{p}, \gamma)^{19}\text{Ne}$	Hot CNO Break-out	upper limit	E811
$^{20}\text{Na}(\text{p}, \gamma)^{21}\text{Mg}$	rp process		
$^{21}\text{Na}(\text{p}, \gamma)^{22}\text{Mg}$	Hot NeNa Cycle/Ne-E		E824
$^{22}\text{Mg}(\text{p}, \gamma)^{23}\text{Al}$	$^{22}\text{Na}$ Production		Letter
$^{23}\text{Mg}(\text{p}, \gamma)^{24}\text{Al}$	Hot NeNa Break-Out		E810
$^{23}\text{Al}(\text{p}, \gamma)^{24}\text{Si}$	$^{22}\text{Na}$ Production		Letter
$^{25}\text{Al}(\text{p}, \gamma)^{26}\text{Si}$	$^{26}\text{Al}$ production/rp process		
$^{26}\text{Al}(\text{p}, \gamma)^{27}\text{Si}$	$^{26}\text{Al}$ production/rp process		

Table 3.1: Radiative capture reactions of astrophysical significance proposed for DRAGON [1]



Figure 3.1: The DRAGON detector. [8]

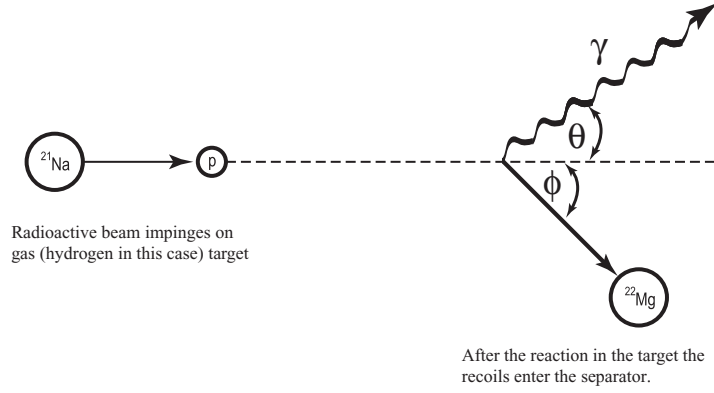


Figure 3.2: Radioactive beams from ISAC impinge on a gas target. The heavy ion recoil leaves the target inside a cone  $\phi$  defined by the reaction kinematics.

### 3.1 Electromagnetic Separator

During their interaction with the target gas, ions go through charge changing processes which result in the recoils emerging from the target with a distribution of charge states. How an ion loses or gains electrons as it encounters an atom is a complicated process and is the subject of another DRAGON thesis [45]. Both beam and recoils, having nearly the same momentum, are then separated by the first magnetic dipole, MD1, according to their charge. The force on a charged particle as it traverses a magnetic field is given by,

$$F = qvB \quad (3.1)$$

where  $q$  is the charge and  $v$  is the velocity of the particle, and  $B$  is the magnetic field then,

$$ma = qvB \quad (3.2)$$

$$m \frac{v^2}{r} = qvB \quad (3.3)$$

$$r = \frac{mv}{qB} \quad (3.4)$$

$$r = \frac{p}{qB} \quad (3.5)$$

where  $m$  is the mass and  $p$  the momentum of the particle, and  $r$  is the radius of the particle's travel in the field. From Equation (3.5) we can see that if the magnetic field and the particle's momentum are both constant, then for different values of the charge the bending radius of the particles will vary accordingly. The most probable charge state is chosen by selecting the correct field for MD1 and other charge states are removed from the beam by intercepting them with mechanical slits (known as the "charge slits") positioned at the exit of MD1. Beam AND recoils of charge  $q$ , which have nearly the same momentum will pass through the slits. Quadrupoles focus the beam and recoils into an electrostatic dipole which separates the particles according to their mass. If the force on a charged particle, as it traverses an electric field, is given by,

$$F = qE \quad (3.6)$$

where  $q$  is the charge on the particle and  $E$  is the electric field then,

$$ma = qE \quad (3.7)$$

$$m \frac{v^2}{r} = qE \quad (3.8)$$

$$r = \frac{mv^2}{qE} \quad (3.9)$$

$$mr = \frac{m^2 v^2}{qE} \quad (3.10)$$

$$r = \frac{p^2}{mqE} \quad (3.11)$$

where  $m$  is the mass and  $p$  is the momentum of the charged particle. At this point, beam and recoils have the same charge and nearly the same momentum, but have masses which differ by a few percent [1]. From Equation (3.11) we can see that if the electric field is kept constant, then for different particle masses the bending radius will vary accordingly. The beam is intercepted by a second set of mechanical slits (i.e. the "mass slits") placed after the electrostatic dipole and the recoils are allowed to pass along the optical axis.

A second stage of magnetic and electrostatic dipoles help to further separate beam from recoils which may have leaked through the first separation stage because:

1. The focus of the magnetic elements of the separator is not perfect so it is possible that beam passed through the “charge slits” and/or the “mass slits” rather than hitting the slits and being removed.
2. Beam particles may have undergone charge changing or scattering (i.e. energy loss) reactions as they pass through DRAGON.

The recoils are steered (using magnetic steerers) and focussed by quadrupoles to the end of DRAGON and deposited on a double-sided, silicon-strip, heavy-ion detector. The detector is segmented into 16 horizontal by 16 vertical strips, each 3 mm in width. The front strips can be used to monitor the focus of the beam at the end station. Further details on the operation and characteristics of the DSSSD can be found in another thesis [46].

The gamma ray signal can be used as a start signal and the DSSSD as a stop signal to produce gamma-recoil time-of-flight measurement to further suppress beam from recoils. Because each reaction produces a characteristic gamma ray energy the BGO array can be used to “tag” this gamma ray to the recoil ion produced in the reaction. Beam particles are distinguished from recoils because they do not have any characteristic gamma ray associated with them. Using DRAGON in non-coincidence mode has shown to give suppression factors of  $10^{-9}$  [8]. Operating DRAGON using the gamma ray array and heavy ion detector to detect heavy ions and characteristic gamma rays in time coincidence raises the observed suppression to  $10^{-13}$  [8]. An example showing the ability to suppress the heavy recoils from unreacted or “leaky” beam (a significant source of background) is shown in Fig. 3.3.

## 3.2 The DRAGON Gamma Ray Array

The DRAGON gamma ray array is composed of 30 hexagonal shaped scintillators, (one of which is shown in Fig. 3.4), measuring 5.78 cm across the face and coupled



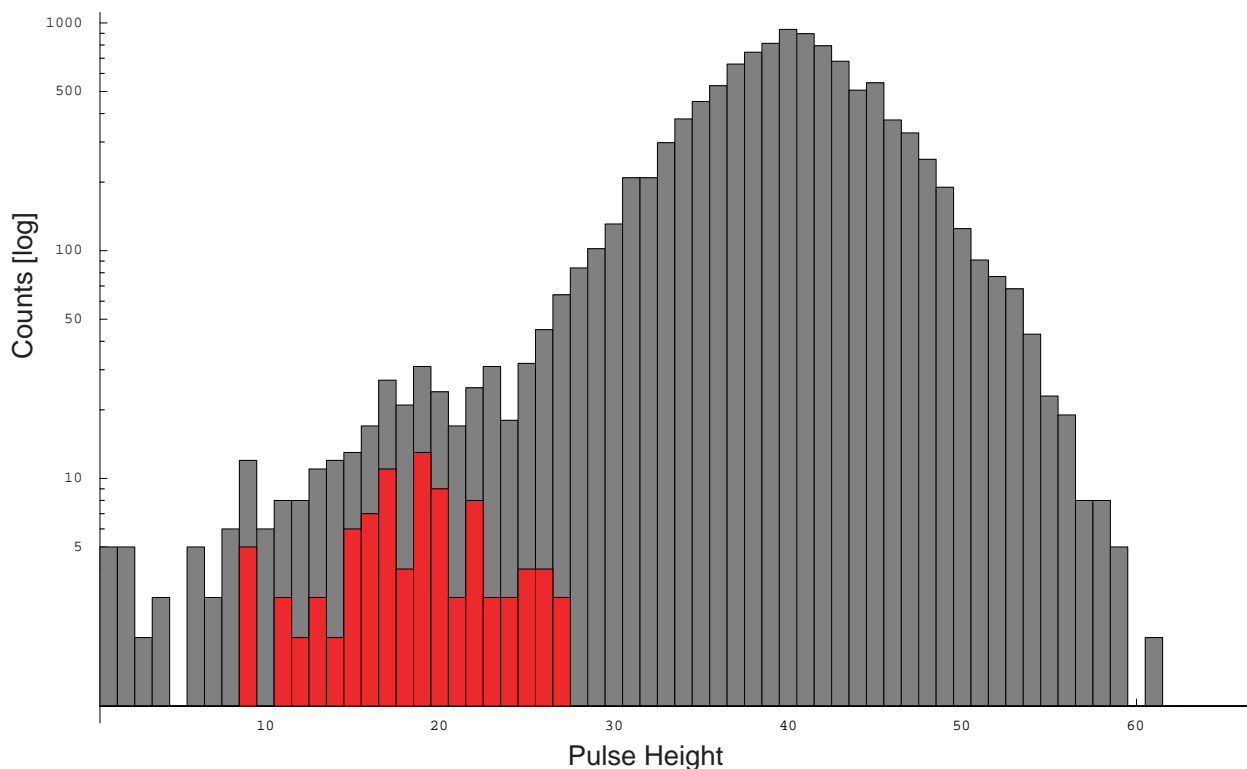


Figure 3.3: An example of how gamma coincidences are used to separate out the “leaky” beam from the recoils of interest in the stable beam reaction  $^{24}\text{Mg}(p,\gamma)^{25}\text{Al}$ . The leaky beam is the larger peak and part of the low energy tail, while the recoils are shown very well separated in red, to the left

to Hamamatsu R1828-01 or Electron Tubes Ltd. (ETL) 9214 photomultiplier tubes. Seven detectors were bought from Bicron [47] while the remaining twenty-three, plus one spare, were acquired from Scionix [48]. The mixture of brand names accommodates price to performance requirements. On average the Bicron detectors perform between 6-10% better in energy resolution than the Scionix ones [49]. The more favourable performance occurs at the typical gamma ray capture energy of 4 MeV. During development of the array seven of each brand name were tested and it was decided that the small performance increase of the Bicron detector was not required, and therefore did not justify the extra cost. The remaining sixteen plus one spare were then purchased from Scionix. The Bicron and Scionix detectors also differ slightly in

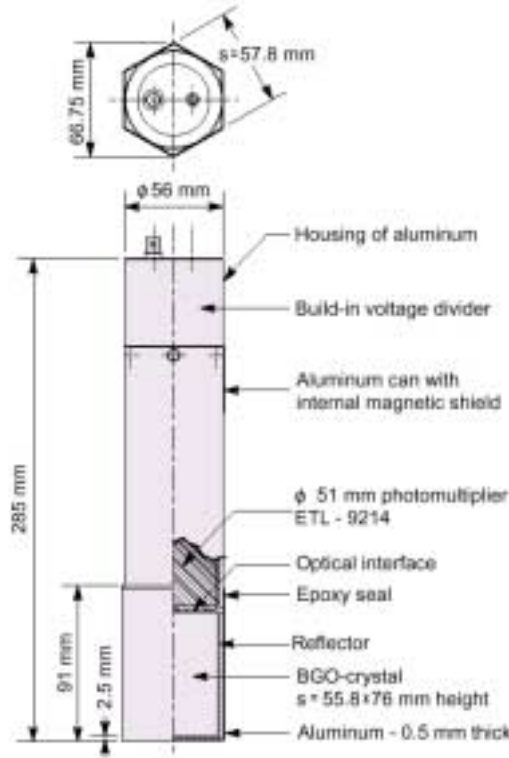


Figure 3.4: One of the gamma ray scintillation detectors composed of a BGO crystal coupled to a 51 mm diameter photomultiplier tube. [8]

their geometry. The aluminum casing of the Bicorn detectors is slightly thicker at 0.535 mm as opposed to the Scionix ones at 0.500 mm. The Bicorn casing runs the entire length of the detector, scintillator and PMT, resulting in a module which has a hexagonal shape along its entire length. The Scionix detector aluminum casing is hexagonal in shape around the scintillator but then a cylindrical casing covers the PMT.

The BGO detectors of the array are positioned in a highly compact arrangement which covers between 89-92% of the solid angle (See Fig. 3.5). Some geometrical coverage is lost when lead shielding is placed at the entrance of the gas target, needed during radioactive beam runs. The lead helps to reduce the background of 511 keV gammas created by beam particles that are deposited on the apertures leading up to

the gas target. When the radioactive beam stops on the aluminum apertures, it beta-plus decays and then through positron/electron annihilation produces a flux of 511 keV gammas. Two of the detectors nearest the gas target aperture must be moved back to accommodate the lead shielding resulting in a loss of  $\approx 3\%$  in geometrical coverage. In the future the lead could be replaced by a beam pipe of “heavy metal” which would allow the detectors to be positioned so that coverage is at the higher 92%. Among the 30 detectors the gamma energy resolution at 6.13 MeV averages 7% full-width half maximum [8]. The efficiency of this array to gammas in the 1-10 MeV range is the subject of this thesis and will be discussed below.

Although many scintillation materials exist, not all of them are suitable for the purposes of particular experiments. For the DRAGON array there were some specific criteria in choosing the scintillation material which ultimately determined the choice of BGO over other scintillators such as  $\text{BaF}_2$ , GSO, NaI, or LSO.

Background gammas caused by decay of the beam occur at a high rate and require a material with a short decay constant. Most of the beams of interest for the radiative capture program decay by emission of a positron, which subsequently annihilates, producing two 511 keV gamma rays. If as little as 0.01% of a beam of intensity  $10^{11}$  particles/s is stopped in the entrance or exit aperture of the central gas cell, it would constitute a background of  $2 \times 10^7$  511 keV gammas/s, a short time (sec's to min's) after the beam is turned on [49]. Severe pile-up of 511 keV gammas could mimic the few-MeV gammas of interest [50]. During the  $^{21}\text{Na}$  beam runs with maximum intensity of  $10^9$ /s, a 511-keV gamma rate of  $1 \times 10^6$ /s was observed in some detectors [8]. Detectors have been tested to handle a 500 Kcps rate [49] with a resolution of 12.5% or better at 667 keV and a gain shift of  $<1\%$  [8]. BGO has the advantage over other scintillators mentioned previously as it emits light with a simple exponential time constant of 300 ns without longer components or afterglow [51]. A dense material, with a short interaction length, is favourable for the efficient detection of high-energy gammas produced in DRAGON experiments. With its high density (7.1 g/cc), modest decay time (300ns), and modest cost per interaction length BGO was the best compromise between efficiency, decay time and cost [43].



Figure 3.5: The DRAGON Gamma Ray Array

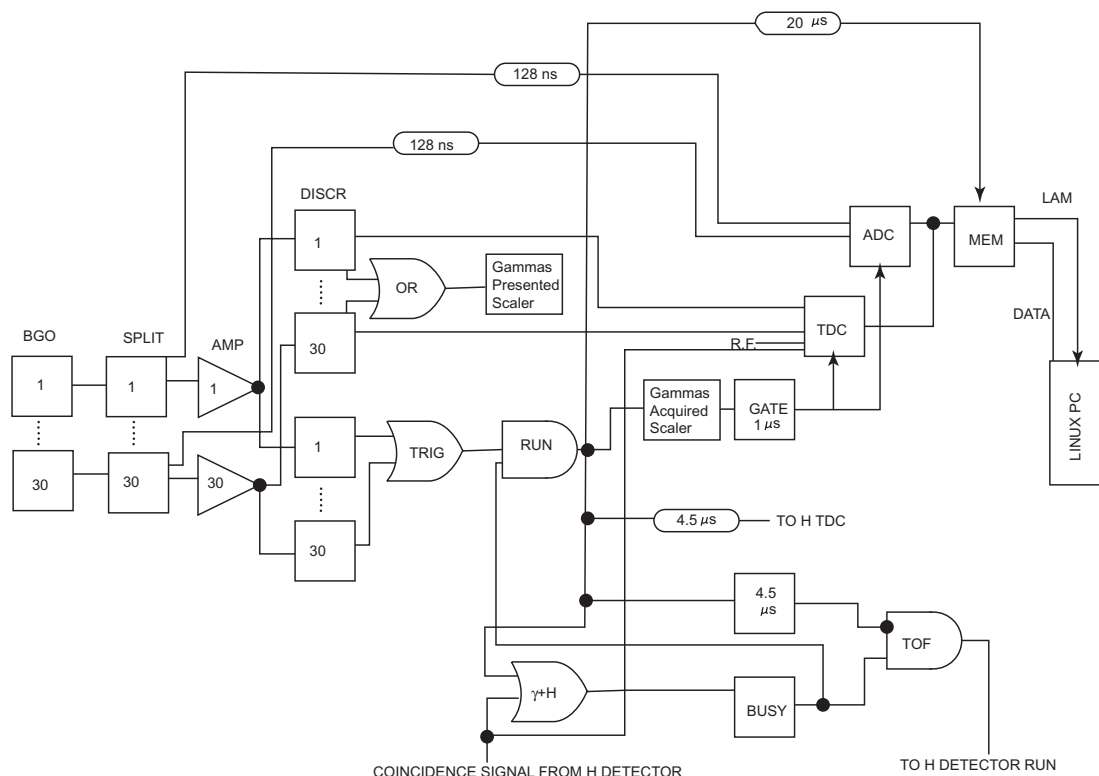


Figure 3.6: Block diagram of the DRAGON gamma detector electronics. Definition of terms: ADC=Analogue to digital converter, AMP=amplifier, BGO=Bismuth Germanate gamma detectors, DISCR=discriminator, MEM=memory, TDC=time to digital converter, H DETECTOR=heavy ion end detector [8]

### 3.3 Electronics and Data Acquisition System

The DRAGON data acquisition system is a MIDAS [52] based data acquisition system written in C by J.G. Rogers of the DRAGON group. The code runs on a P-III PC running Linux 7.3. The acquisition system accesses all hardware electronics through a single Lecroy 8025 CAMAC crate. All electronic modules are housed within the CAMAC crate, 2 NIM bins and a EUROCRATE and includes electronics for both the BGO gamma detectors and DSSSD heavy ion detector. A more complete description of the electronics of the DSSSD detector is given in [8].

The high voltage for the gamma detectors is supplied by a Lecroy HV4032A high voltage supply which can be set manually or by computer control. The high voltage

supplied to the detectors controls the gain which is chosen according to experimental preferences. This procedure is outlined in §C.1.

The signal from each of the 30 detectors is transported through a BNC cable to a linear fan-out where it is split into two signals, one going to a Lecroy FERA charge-sensitive ADC while the other goes to an amplifier. The second signal is amplified a factor of ten, and sent to two separate outputs. One output is fed into a leading edge discriminator while the other passes through an 8MHz low pass filter before proceeding into a constant fraction discriminator. The output from the constant fraction discriminator is used in a scaler to provide a “gammas presented” rate. This rate can be used to monitor gamma detector dead-time by using this rate together with a “gammas collected” rate recorded just before the ADC. The rate has also been used as a beam spill diagnostic. A high rate in this scaler indicates “misteered” beam which collides with collimators or beam pipes rather than passing unobstructed through the gas target. The resulting rate of 511 gammas produced by decay of the beam off these components is proportional to the beam spill.

All 30 signals from the constant fraction discriminators (CFD’s) are gathered together into a logical “OR” to generate a gamma master gate signal which provides the gate signal for the ADC’s. The OR also provides start signals for the two 32 channel TDC’s as well as providing a “HOLD” on further data transmission. Once the HOLD is initiated a time of 20  $\mu$ s is required for the ADC’s and TDC’s to convert and transfer their data into memory.

Charge-sensitive ADC’s require an integration time to be set and in our case this gate is set by the length of the master-gate signal provided by the OR. The gate width, which can be set manually or by computer control, is a compromise between fast collection time and good energy resolution. Due to its 300 ns decay constant BGO would require a minimum gate of 300 ns to provide adequate charge integration. A time shorter than this would degrade energy resolution but at the same time would allow faster counting rates. A rate of 650-1000 ns has been used for experiments to date, as a compromise between fast charge collection and good energy resolution [8].

The logical OR from the 30 CFD signals starts a single event collection when a gamma ray exceeding the specified threshold is detected. This signal triggers the

master gate to be opened during which time all ADC's are able to convert data. During the time that the ADC's are gated on, at least one gamma will be recorded (i.e. the one that caused the trigger) but others may also be counted if they arrive in the detectors during the time that the ADC gate is open. Compton scattering or pair production within the BGO may cause secondary gammas to be generated and collected in other detectors during the gate time. In another case, during experiments a cascade decay of a nucleus may provide other gamma rays besides the triggering one to be collected.

Gamma singles are acquired along with gamma/heavy-ion coincidences. The computer sorts events as either singles or coincidences based on gamma/heavy-ion TDC values which the software requires must be less than  $4.5 \mu s$  for coincidence events.

### 3.4 Dead-Time Correction Using Scalers

Gamma dead-time corrections for the measurements done in this thesis were the done in the same manner as all other measurements performed by the DRAGON group. As mentioned previously a "gammas presented" scaler, (See Fig. 3.6), and a "gammas acquired" scaler were used to calculate the dead-time in each measurement carried out. The gammas presented scaler recorded any gamma event above a set discriminator value that entered the system. Just prior to conversion by the ADC's, the second, gammas acquired scaler gave the number of gamma events that went to output. The difference in the two rates is caused by the HOLD that is put on further data transmission during the time that the ADC's and TDC's are converting and transferring their data into memory. During this time the gammas presented scaler will continue to accumulate gamma counts but the gammas acquired will not, therefore giving a representation of the total system dead-time (live-time). The ratio of gammas acquired to gammas presented gives  $1/\text{dead-time}$  or the total live-time of the system. The system for dead-time correction was implemented and tested by Joel Rogers of the DRAGON group, and it was approved and used by the group for all gamma dead-time corrections to this point. The system was tested by measuring the peak counts with a 6.13 MeV source at various gamma thresholds. The dead-time

ranged from 8% to 54% and the gamma rate did not change, after scaler dead-time corrections were made [53].



## Chapter 4

# Radiative Capture Reaction Rates

The rate of the reactions, involved in the processes of Chapter 1, determines the path along which nucleosynthesis will occur. Understanding these reaction paths is important in determining the mechanisms creating observed stellar environments. Theorists have produced complicated models through which they hope to be able to simulate these mechanisms but the models require data for a basis and for test purposes. The experiments proposed for DRAGON were chosen to provide direct measurements of some of key reactions in the stellar mechanisms and in addition provide theorists with the data they require for their models.

### 4.1 Stellar Reaction Rate Defined

The thermonuclear reaction rate  $\langle\sigma v\rangle$  is the product of the relative velocities  $v$  of the interacting particles and the cross section  $\sigma(v)$  for a single target nucleus folded with the velocity distribution  $\phi(v)$  of the particles [3],

$$\langle\sigma v\rangle = \int_0^\infty \phi(v)v\sigma(v) dv \quad (4.1)$$

In a non-degenerate stellar gas in thermodynamic equilibrium the velocities of the particles is described by a Maxwell-Boltzmann velocity distribution [3]. Using the centre of mass energy  $E = \frac{1}{2}\mu v^2$  the thermonuclear reaction rate  $\langle\sigma v\rangle$  per particle

pair is [3]:

$$\langle \sigma v \rangle = \sqrt{\frac{8}{\pi \mu}} \frac{1}{(kT)^{\frac{3}{2}}} \int_0^\infty E \sigma(E) \exp\left(-\frac{E}{kT}\right) dE \quad (4.2)$$

Where,

$\mu$  = is the reduced mass of the two colliding particles

$k$  = is Boltzmann's constant

$T$  = is the temperature of the stellar gas

$E = \frac{\mu v^2}{2}$  is the kinetic energy in the centre of mass

$\sigma(E)$  = is the nuclear cross section

## 4.2 Non Resonant Reaction Rate

If the fusion of two particles ( $Z_1$  and  $Z_2$ ) in a stellar environment happens through a non-resonant reaction then the cross section is given by [3],

$$\sigma(E) = \frac{S(E)}{E} \exp\left(-\frac{2\pi Z_1 Z_2 e^2}{\hbar v}\right) \quad (4.3)$$

where the function  $S(E)$ , defined by Equation (4.3), contains all the strictly nuclear effects [3]. For non-resonant reactions this factor, called the astrophysical S-factor, is a smoothly varying function of energy which by design varies much less than the cross section. This property make the S-factor useful in extrapolating cross sections to astrophysical energies. Substituting Equation (4.3) into Equation (4.2) gives [3],

$$\langle \sigma v \rangle = \sqrt{\frac{8}{\pi \mu}} \frac{1}{(kT)^{\frac{3}{2}}} \int_0^\infty S(E) \exp\left[-\frac{E}{kT} - \frac{b}{E^{\frac{1}{2}}}\right] dE \quad (4.4)$$

where,

$$b = 0.989 Z_1 Z_2 \sqrt{\mu} \left( \frac{1}{MeV} \right)$$

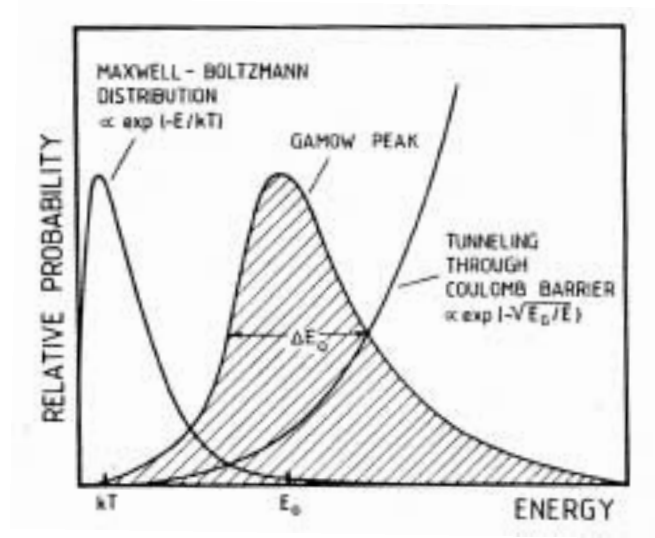


Figure 4.1: The dominant energy-dependent functions are shown for nuclear reactions between charged particles. While both the energy distribution function (Maxwell-Boltzmann) and the Coulomb barrier penetrability function are small for the overlap region, the convolution of the two functions results in the Gamow Peak near the energy  $E_0$ , giving a sufficiently high probability to allow reactions to occur. [3]

and the quantity  $b^2$  is called the Gamow energy. For a given stellar temperature  $T$ , nuclear reactions take place in the relatively narrow “Gamow window”. The Gamow window is where the product of the Maxwell Boltzmann distribution and Coulomb barrier penetrability terms is largest, within the integrand of Equation (4.4) (See Fig. 4.1) [3]. It is often found that the S-factor is nearly constant over the Gamow window and so it can be taken out of the integral, then *the stellar reaction rate per particle pair for a **non-resonant reaction*** is [3],

$$\langle \sigma v \rangle = \sqrt{\frac{8}{\pi \mu}} \frac{1}{(kT)^{\frac{3}{2}}} S(E) \int_0^{\infty} \exp \left[ -\frac{E}{kT} - \frac{b}{E^{\frac{1}{2}}} \right] dE \quad (4.5)$$

### 4.3 Resonant Reaction Rate

A resonance reaction occurs if a nuclear reaction between two particles happens such that the newly formed particle is produced in a bound, excited state, termed a compound nucleus, in which case the following holds [3],

$$E_R = E_r - Q \quad (4.6)$$

where  $E_R$  is the energy of the projectile,  $E_r$  is the excitation energy of the compound nucleus, and  $Q$  is the Q-value of the reaction. Reactions which proceed through this mechanism show several orders of magnitude increase in cross sections as compared to the non-resonant mechanism. This increase can be thought of as coming about because the amplitudes of the wave functions of the two particle system and the compound nucleus are optimally matched [54].

The cross section for reactions occurring under non interfering, isolated resonance conditions is given by the Breit-Wigner formula [3],

$$\sigma(E) = \pi\lambda^2 \frac{2J+1}{(2J_1+1)(2J_2+1)} (1+\delta_{12}) \frac{\Gamma_a\Gamma_b}{(E-E_R)^2(\Gamma/2)^2} \quad (4.7)$$

Where we have used,

$E$  = is the energy in the centre of mass

$\lambda$  = is the reduced de Broglie wavelength in the centre of mass

$\Gamma_a\Gamma_b$  = are the partial widths of the incoming particles

$J_1$  = spin of the projectile nucleus

$J_2$  = spin of the target nucleus

$J$  = angular momentum of the excited state in the compound nucleus

$\Gamma$  =  $\Gamma_a + \Gamma_b$

$E_R$  = is the resonance energy

The term  $(1+\delta_{12})$  is included because the cross section increases by a factor of 2 in the case of identical particles in the entrance channel [3].

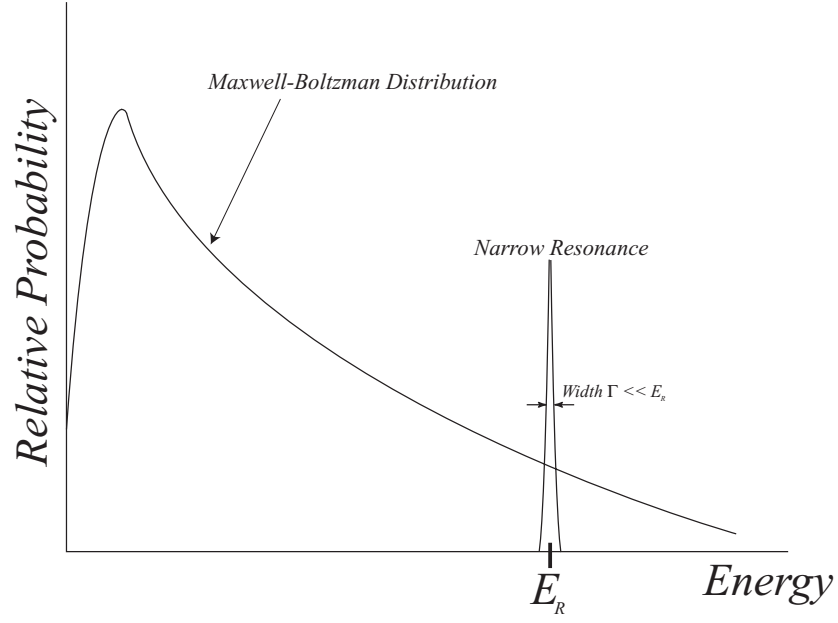


Figure 4.2: The Maxwell-Boltzmann distribution for a given stellar temperature  $T$  and the cross section for a narrow resonance ( $\Gamma \ll E_R$ ) [3]

Assuming we are dealing with a narrow resonance where  $\Gamma \ll E_R$  then the Maxwell Boltzmann function of Equation (4.2) varies very little over the resonance energy (See Fig. 4.2) so it can be taken outside the integral to give [3],

$$\langle \sigma \nu \rangle = \sqrt{\frac{8}{\pi \mu}} \frac{1}{(kT)^{\frac{3}{2}}} E \exp\left(-\frac{E}{kT}\right) \int_0^\infty \sigma(E)_{BW} dE \quad (4.8)$$

where  $\sigma(E)_{BW}$  is the Breit-Wigner cross section. Evaluation of the integral in Equation (4.8) yields [3],

$$\int_0^\infty \sigma(E)_{BW} dE = 2\pi^2 \lambda_R^2 \omega \gamma \quad (4.9)$$

where,

$$\omega = \frac{2J+1}{(2J_l+1)(2J_2+1)}(1+\delta_{12}) \quad (4.10)$$

$$\gamma = \frac{\Gamma_a \Gamma_b}{\Gamma} \quad (4.11)$$

$$\lambda_R^2 \simeq \lambda^2 \text{ for a narrow resonance} \quad (4.12)$$

$$\lambda = \text{the reduced de Broglie wavelength} \quad (4.13)$$

We can then combine Equation (4.8), Equation (4.9), Equation (4.11) and Equation (4.13) to give *the stellar reaction rate per particle pair for a **narrow resonance*** [3]:

$$\langle \sigma \nu \rangle = \left( \frac{2\pi}{\mu kT} \right)^{3/2} \hbar^2 (\omega \gamma)_R \exp \left( -\frac{E_R}{kT} \right) \quad (4.14)$$

The quantity  $\omega \gamma$  is termed the resonance strength. When a nuclear reaction has several narrow resonances their contributions to  $\langle \sigma \nu \rangle$  are summed.

## 4.4 Experimental Yield

The stellar reaction rate is connected to laboratory experiments by the yield of the nuclear reaction, directly measured as the rate of production of the desired final state recoils and gammas. By finding the experimental yield, the resonance strength  $\omega \gamma$  can be calculated and used to find the stellar reaction rate. Each incoming beam particle to the DRAGON gas target has a probability (i.e. the cross section of the reaction) to react with the nuclei in the gas target. Each target nucleus has associated with it an effective area  $\sigma$  such that each incoming beam particle passing within this area will react with the target with 100% probability. If the target is thin, (i.e. the individual effective areas do not overlap) then the yield is given by the “thin target yield equation” [3],

$$Y = \sigma \frac{dE}{\epsilon} \quad (4.15)$$

where,  $dE$  is the energy loss of the incoming beam particles as they pass through the target, and  $\epsilon$  is the stopping cross section, and  $\sigma$  is the reaction cross section.

If the target does not fulfill the condition for a thin target (i.e. the effective areas DO overlap) then the yield is calculated by integrating the thin target yield equation over the entire thickness of the target [3],

$$Y(E_0) = \int_{E_0-\Delta}^{E_0} \frac{\sigma(E)}{\epsilon(E)} dE \quad (4.16)$$

where,  $\Delta$  is the energy loss of the projectiles in the target and  $E_0$  is the incident particle energy. If experimental yield involves a narrow resonance ( $\Gamma \ll E_R$ ) then  $\sigma(E)$  is the Breit-Wigner cross section given in Equation (4.7). If  $\Delta \gg \Gamma$ , and the energy dependence of  $\lambda^2, \Gamma_a, \Gamma_b$  and  $\epsilon$  is negligibly small over the region of the resonance then the integral in Equation (4.16) can be evaluated to give [3],

$$Y = \frac{\lambda^2}{2\pi} \omega \gamma \frac{1}{\epsilon} \frac{M_T + M_B}{M_T} \left[ \arctan \left( \frac{E_0 - E_R}{\Gamma/2} \right) - \arctan \left( \frac{E_0 - E_R - \Delta}{\Gamma/2} \right) \right] \quad (4.17)$$

Where,

$M_T$  = the mass of the target particle

$M_B$  = the mass of the beam particle

and when  $E_0 \gg E_R$  the yield reaches a maximum  $Y_{max}(\infty)$  at  $E_0 = E_R + \Delta/2$  which represents the integral over the entire resonance region [3],

$$Y = \frac{\lambda^2}{2} \omega \gamma \frac{1}{\epsilon} \frac{M_T + M_B}{M_T} \quad (4.18)$$

In the lab the resonance energy  $E_R$ , can be found by mapping out the thick target yield curve (See Fig. 4.3) to find the 50% point in yield. The points at 25% and 75% represent the width ( $\Gamma$ ) of the resonance (assuming no beam spread).

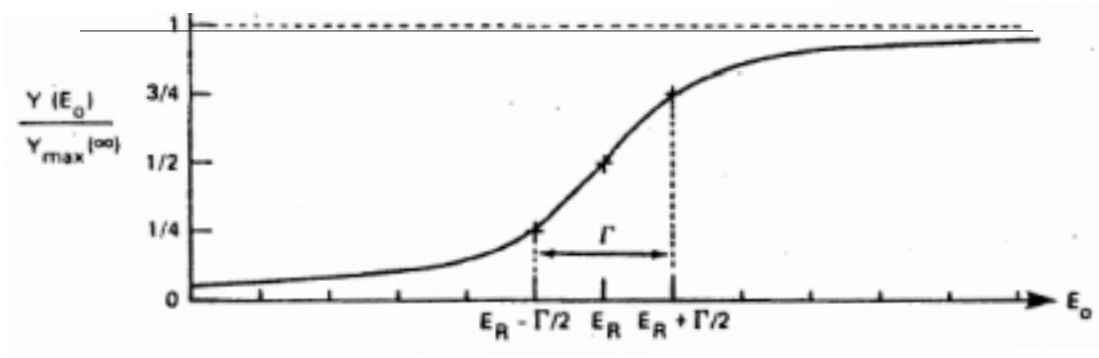


Figure 4.3: Thick target yield curve where the 50% yield point represents the resonance energy and the points at 25% and 75% represent the width ( $\Gamma$ ) of the resonance (assuming no beam spread). [3]



# Chapter 5

## GEANT Simulation

### 5.1 GEANT Background

#### 5.1.1 Introduction

GEANT is a Fortran computer program which simulates the interaction of energetic particles through different media, using Monte Carlo techniques. The program can be run in two different modes, batch mode or interactive mode. Both modes generate, track and record the appropriate information of a specified number of particles as they traverse specified media. The event data can then be read by the user directly from the various memory banks and used accordingly or all the events can be histogrammed into frequency distributions by software packages such as HBOOK. The interactive mode provides visualization of the simulation by drawing the geometrical detector components and the paths of the particles as they traverse the media. Graphical representation is slower in execution speed, so the user must decide which mode is appropriate for the given application.

Data structures in GEANT are stored in the /GCBANK/ common block. The structures are accessed by using a pointer with names starting with the letter “J”. For example, data about detector volumes is stored in a data structure named “JVOLUM”. A user written main program allocates dynamic memory blocks and then turns control over to the three phases of any GEANT simulation run. The three phases are

initialization, event processing and termination. In any of these three phases the user can provide his own code for the appropriate subroutine.

The routine UGINIT initializes the GEANT common blocks, fills the appropriate data structures with the particle and material properties, initializes the drawing package by drawing the volumes specified in the UGEOM (see §5.1.8), and specifies sensitive volumes.

In the event processing phase an event is triggered and processed by the routines GTRIGI and GTRIG. A check to see if more events are to be processed is then performed by GTRIGC. The GTRIG routine calls the GUKINE routine to define the event kinematics and proceeds through to GUTREV which performs the tracking of the particles (§5.1.7) through the media. GUSTEP performs the necessary operations during each step of the particle along a track. GUDIGI then simulates the detector response for that event by digitizing the “hit” information and storing it in the JDIGI data structure. GUOUT does the final processing of the events and outputs the required data structures. The final termination phase can be controlled by the user with a call to GLAST, which computes some statistical information.

The subroutine calling sequence shown in Fig. 5.1 provides a useful visualization of the processes and the order they are called during program execution.

### 5.1.2 GEANT Physics Processes

GEANT has the capability of simulating dominant electromagnetic interactions in the 10 keV to 10 TeV range, while particles are tracked through different media. The simulation proceeds by evaluating the probability of a process by sampling the total cross section, and then generating the final state by sampling the differential cross section of the process. GEANT 3.21 implements the following major categories of physical processes:

1. Processes involving photons (e.g.  $e^-/e^+$  pair conversion, Compton scattering, photoelectric effect, photo fission of heavy elements, Rayleigh effect)
2. Processes involving  $e^-/e^+$  (e.g. multiple scattering, ionization and delta rays)

MAIN	user routine
GZEBRA	initialisation of ZEBRA system, dynamic core allocation
UGINIT	user routine
GINIT	initialisation of GEANT variables
GFFGO	interpretation of data records
GZINIT	initialisation of ZEBRA core divisions and link areas
GPART/GSPART	creation of the <i>particle</i> data structure JPART
GMATE/GSMATE	creation of the <i>material</i> data structure JMATE
<i>user code</i>	description of the geometrical setup, of the sensitive detectors, creation of data structures JVOLUM, JTMED, JROTM, JSETS
GPHYSI	preparation of cross-section and energy-loss tables for all used materials
GRUN	loop over events
GTRIGI	initialisation for event processing
GTRIG	event processing
GUKINE	(user) generation (or input) of event initial kinematics
GUTREV	(user)
GTREVE	loop over tracks, including any secondaries generated
GUTRAK	(user)
GTRACK	control tracking of current track
GFINDS	find current volume in the geometry tree
GUSTEP	(user) recording of hits in data structure JHITS and of space points in data structure JXYZ
GUPARA	called if the particle falls below the tracking threshold
GTGAMA/GTELEC/...	tracking of particle according to type
GFSTAT	fill banks for volume statistics
GSTRAC	store information of the current track segment
GUSTEP	(user) recording of hits in data structure JHITS and of space points in data structure JXYZ
GTMEDI	finds in which volume/medium the current space point is
GUSTEP	(user) recording of hits in data structure JHITS and of space points in data structure JXYZ
GUDIGI	computation of digitisations and recording in data structure JDIGI
GUOUT	output of current event
GTRIGC	clearing of memory for next event
UGLAST	(user)
GLAST	standard GEANT termination

Figure 5.1: Simplified GEANT flow chart [9]

production, Bremsstrahlung, positron annihilation, Cerenkov light, synchrotron radiation)

3. Processes involving  $\mu^-/\mu^+$  (e.g. decay in flight, multiple scattering, ionization and delta rays production, Bremsstrahlung, ionization of heavy ions,  $e^-/e^+$  pair production, nuclear interaction, Cerenkov light)
4. Processes involving hadrons (e.g. decay in flight, multiple scattering, Cerenkov light, ionization and delta rays production, hadronic interactions)

The details of only the processes significant in gamma ray spectroscopy [5] namely, (1) and (2) above are discussed here.

### 5.1.3 Simulating a Physics Process

The simulation of the processes which may occur to a particle traversing a medium is carried out in steps. Once a new particle or “track” is created the number of interaction lengths the particle will travel before undergoing a physical process is sampled and stored. Next, the individual tracking routines (e.g. GTGAMA for photons §5.1.7) evaluate the distance to the next interaction point. The distance the particle will travel, or “step”, is dependent on the cross section for that process to occur in the current medium, and also on geometric boundaries, user defined step size, energy thresholds and time cuts. Each of these processes will terminate the current step. The particle is transported along either a straight path (no magnetic field or neutral particle) or helical path and the energy of the particle is updated if a continuous process is in effect, otherwise a discrete process will generate the final state. The new number of interaction lengths before the next interaction is then calculated assuming the particle survived the last process. Control of the simulation will then loop back to the individual tracking routines (e.g. §5.1.7) until the particle drops below the energy threshold, it disappears in an interaction, it exceeds the time cut, or it leaves the detector.

### The Interaction Length

If the **total *microscopic* cross section** is represented by  $\sigma(E, Z, A)$  then in general the mean free path, which is tabulated at initialization time as a function of kinetic energy of the particle,  $\lambda$  is given by,

$$\lambda = \frac{1}{\Sigma} \quad (5.1)$$

Where,  $\Sigma$  is defined as the **total *macroscopic* cross section** in  $[cm^{-1}]$  and represented for an element by,

$$\Sigma = \frac{N_{AV} \rho \sigma(E, Z, A)}{A} \quad (5.2)$$

And for a compound, such as a NaI scintillator, by,

$$\Sigma = \frac{N_{AV} \rho \sum_i n_i \sigma(E, Z_i, A_i)}{\sum_i n_i A_i} \quad (5.3)$$

$$= N_{AV} \rho \sum_i \frac{p_i}{A_i} \sigma(E, Z_i, A_i) \quad (5.4)$$

Where,

$N_{AV}$  = Avogadro's number ( $6.02486 \times 10^{23}$ )

$Z$  = atomic number

$A$  = atomic weight

$\rho$  = density

$\sigma$  = total cross section for the reaction

$n_i$  = proportion by number of the  $i^{th}$  element in the material

$p_i$  =  $n_i A_i / \sum_j n_j A_j$ , proportion by weight of the  $i^{th}$  element in the material

For electromagnetic processes which depend linearly on atomic number  $Z$  we can write,

$$\Sigma = N_{\text{AV}} \rho \sum_i \frac{p_i}{A_i} \sigma(E, Z_i) \quad (5.5)$$

$$= N_{\text{AV}} \rho \sum_i \frac{p_i}{A_i} Z_i f(E) \quad (5.6)$$

$$= N_{\text{AV}} \rho f(E) \sum_i \frac{p_i}{A_i} Z_i \quad (5.7)$$

$$\Sigma = N_{\text{AV}} \rho f(E) Z_{\text{eff}} \quad (5.8)$$

where,

$$Z_{\text{eff}} = \sum_i \frac{p_i}{A_i} Z_i \quad (5.9)$$

is calculated by the GPROBI routine.

If the user wishes to measure and define their own microscopic cross section in barns where  $1\text{b} = 1 \times 10^{-24} \text{cm}^{-2}$  then  $\Sigma[\text{cm}^{-1}]$  can be expressed as,

$$\Sigma = 0.602486 \frac{\rho[\text{g cm}^{-3}]}{A} \sigma(E, Z, A)[\text{b}] \quad (5.10)$$

### The Point of Interaction

The point of interaction of a particle, with mean free path  $\lambda$ , moving through a medium is given by,

$$N_\lambda = \int \frac{dx}{\lambda(x)} \quad (5.11)$$

If  $N_R$  is a random number variable denoting the number of mean free paths from some starting point to the point where the interaction takes place, then it can be shown [55] that  $N_R$  has a distribution function of the form

$$P(N_R < N_\lambda) = 1 - \exp(-N_\lambda) \quad (5.12)$$

The point of interaction  $N_\lambda$  can then be found by sampling from this distribution by

$$N_\lambda = -\log(\eta) \quad (5.13)$$

where  $\eta$  is uniformly distributed between (0,1).

The total number of mean free paths which a particle will travel must then be updated after each step  $\Delta x$ , by,

$$N_\lambda = N'_\lambda - \frac{\Delta x}{\lambda(x)} \quad (5.14)$$

### Tabulated Material Properties

Values for cross sections,  $dE/dx$  and range  $R(E_{kin})$  for all materials, defined as a “medium”, which the user wishes to track particles through are tabulated for various energies by the routine GPHYSI. To evaluate a quantity for a specific kinetic energy  $E_0$ , a linear interpolation is used such that for  $i$ ,  $E_i < E_0 \leq E_{i+1}$ . If the quantity  $C$  has been tabulated so that  $C_i = C(E_i)$  then the value  $C_0 = C(E_0)$  is calculated as [55]:

$$C_0 = C_i + \frac{E_0 - E_i}{E_{i+1} - E_i}(C_{i+1} - C_i) \quad (5.15)$$

$$= C_i \left( 1 - \frac{E_0 - E_i}{E_{i+1} - E_i} \right) + C_{i+1} \frac{E_0 - E_i}{E_{i+1} - E_i} \quad (5.16)$$

As mentioned previously in §5.1.1 energy loss tables are calculated at initialization time for all materials defined as a medium. For the special case of mixtures/compounds the rule [56] is to combine the energy loss tables according to the proportion by weight of the elements, that is:

$$\frac{dE}{dx} = \rho \sum_i \frac{p_i}{\rho_i} \left( \frac{dE}{dx} \right)_i \left[ \frac{\text{GeV cm}^2}{\text{g}} \right] \quad (5.17)$$

#### 5.1.4 Simulating Pair Production by Photons in GEANT

Using the definitions of  $\lambda$  and  $\Sigma$  from §5.1.3 the parameterized total cross section for pair production in a medium is defined as,

$$\sigma(Z, E_\gamma) = Z(Z+1)(F_1(X) + F_2(X)Z + \frac{F_3(X)}{Z} \left[ \frac{\text{barn}}{\text{atom}} \right]) \quad (5.18)$$

Where,

$$\begin{aligned}
 X &= \ln \frac{E_\gamma}{m} \\
 m &= \text{electron mass} \\
 E_\gamma &= \text{photon energy} \\
 F_i(x) &= \sum_{n=0}^5 c_n X^n
 \end{aligned}$$

The parameters,  $c_n$  in Equation (5.18), are from a least squares fit to data contained in reference [57]. The parameterization is found to be good within the range  $1 \leq Z \leq 100$ , and  $1.5 \text{ MeV} \leq E_\gamma \leq 100 \text{ GeV}$ , where

$$\frac{\Delta\sigma}{\sigma} \leq 5\% \text{ with a mean value of } \frac{\Delta\sigma}{\sigma} \approx 2.2\% \quad (5.19)$$

The simulation of pair production, implemented by the routine GPAIRG and called by GTGAMA (See §5.1.7), uses the random number techniques of references [58] [59] to sample the electron/positron energies from the Coulomb corrected Bethe-Heitler [60] differential cross section.

The angular distribution of the pair is sampled by the routine GBTETH which generates the polar angles of the electron with respect to an axis defined along the direction of the parent photon. The electron and positron are assumed to have a symmetric distribution described by Tsai in [61] [62].

### 5.1.5 Simulating Compton Scattering by Photons in GEANT

The mean free path,  $\lambda$ , for a photon to interact via Compton scattering is given by

$$\lambda = \frac{1}{\Sigma} = \frac{A}{N_{\text{AV}} \phi} \frac{1}{\sigma(Z, E)} \quad (5.20)$$



where

$N_{AV}$  = Avogadro's number

$Z, A$  = atomic and mass number of the medium

$\phi$  = density of the medium

$\sigma$  = total cross-section per atom for Compton scattering

$E$  = energy of the photon

The empirical cross sectional  $\sigma(Z, E)$  used in GEANT was found [55] by fitting to data with  $Z$  values between 1 and 100 and energy range between 10 keV and 100 GeV. The accuracy of the fit [55] was estimated to have a value for  $\Delta\sigma/\sigma$  of approximately 10% in the 10-20 keV range and less than 5% for energies above 20 keV.

As it was done for pair production, the random number techniques of [58] were used to sample the Compton scattered photon energy according to the Klein-Nishina [42] distribution. A detailed description of the Monte Carlo methods used for Compton scattering in GEANT are contained in the works of Butcher and Messel [58], Messel and Crawford [63], and Ford and Nelson [60]. The basis of the method is the quantum mechanical Klein-Nishina [42] formula, which is only valid if the energy of the recoil electron is large compared to its binding energy, which is ignored. Rossi [64] points out that violating this requirement produces negligible error because of the small number of recoil electrons produced at very low energies.

### 5.1.6 Simulating the Photoelectric Effect in GEANT

The total cross section for the photoelectric effect in a material is divided into two parts in GEANT: elements or mixtures with  $Z \leq 100$  and those with  $Z > 100$ , which do not occur in our detectors. For materials or mixtures where  $Z \leq 100$  the total cross section is parameterized according to [65] which was fitted [55] with a linear combination of reciprocal powers of the photon energy  $E_\gamma$ . The fits were performed in different intervals of the photon energy, and the cross section in this interval is as follows,

$$\Sigma = \rho\mu \left[ \frac{1}{\text{cm}} \right] \quad (5.21)$$

$$\Sigma = \frac{N_{\text{AV}}\rho\sigma(Z, E_\gamma)}{A} \left[ \frac{1}{\text{cm}} \right] \quad (5.22)$$

And for a compound or mixture as in the case of BGO,

$$\Sigma = \frac{N_{\text{AV}}\rho \sum_i \sigma(Z, E_\gamma)}{\sum_i n_i A_i} \quad (5.23)$$

$$= N_{\text{AV}}\rho \sum_i \frac{p_i}{A_i} \sigma(Z_i, E_\gamma) \left[ \frac{1}{\text{cm}} \right] \quad (5.24)$$

Where,

$N_{\text{AV}}$  = Avogadro's number

$Z_i$  = atomic number of the  $i_{th}$  component of the medium

$A_i$  = atomic mass of the  $i_{th}$  component of the medium

$\rho$  = density

$n_i$  = proportion by number of the  $i_{th}$  element in the material

( $n_i = Wp_i/A_i$  where  $p_i$  is the corresponding proportion  
by weight and  $W$  is the molecular weight)

$\sigma(Z, E_\gamma)$  = the total cross section for the photoelectric effect

$\sigma$  was found [55] from a fit of 301 data points chosen between  $5 \leq Z \leq 100$  and in an energy range 10-50000 keV. The accuracy of this fit was estimated to be [55],

$$\frac{\Delta\sigma}{\sigma} \leq 25\%$$

### 5.1.7 Tracking Particles

Particles in GEANT are tracked through a seven dimensional space  $(x, y, z, t, p_x, p_y, p_z)$  by integrating the equations of motion from one trajectory point to another. To be able to simulate these processes in a reasonable time, continuous processes are approximated by calculating the 7 coordinates at discrete intervals [66]. The size of the interval between points, called the “step size”, is controlled by a set of user-defined, energy dependent thresholds. The tracking package contains routines to track various particles (e.g. gammas, electrons, hadrons, etc), store their space-coordinates, and calculate their momenta in each event. The particle step size during any event is dependent primarily on the intrinsic properties of the particle and the characteristics of the medium it passes through. In addition, a step size may be limited by the distance to the next volume boundary, which signals a change in medium type (see below). All steps terminate at such a boundary and a new step begins in the new volume [66].

The subroutine GTRACK transports the particle through the geometrical volumes and identifies each new volume with a call to GTMEDI. GTRACK calls GTVOL which calculates the distance to the next volume and references the particle type to invoke specific particle tracking routines. Type “1” represents a gamma ray, so GTGAMA is called. The function of GTGAMA is to choose which interaction processes involving the gamma ray will occur. The block diagram Fig. 5.2 explains the function of GTGAMA.

### 5.1.8 GEANT Geometry Package

The GEANT geometry package provides the user with the tools to define the structure of a detector and target cell via the UGEOM.F user routine. For the simulation of the DRAGON gamma array this routine included definitions of detector enclosures, “sensitive” volumes, and other (e.g. target) tracking media. Sensitive volumes in GEANT are defined as volumes from which tracking information (e.g. energy, momentum, etc.) can be collected. In general GEANT volumes are built in a hierarchy where smaller volumes are placed inside larger volumes, like in a Russian doll. These volumes are called “mother” and “daughter” volumes where the daughter volumes are

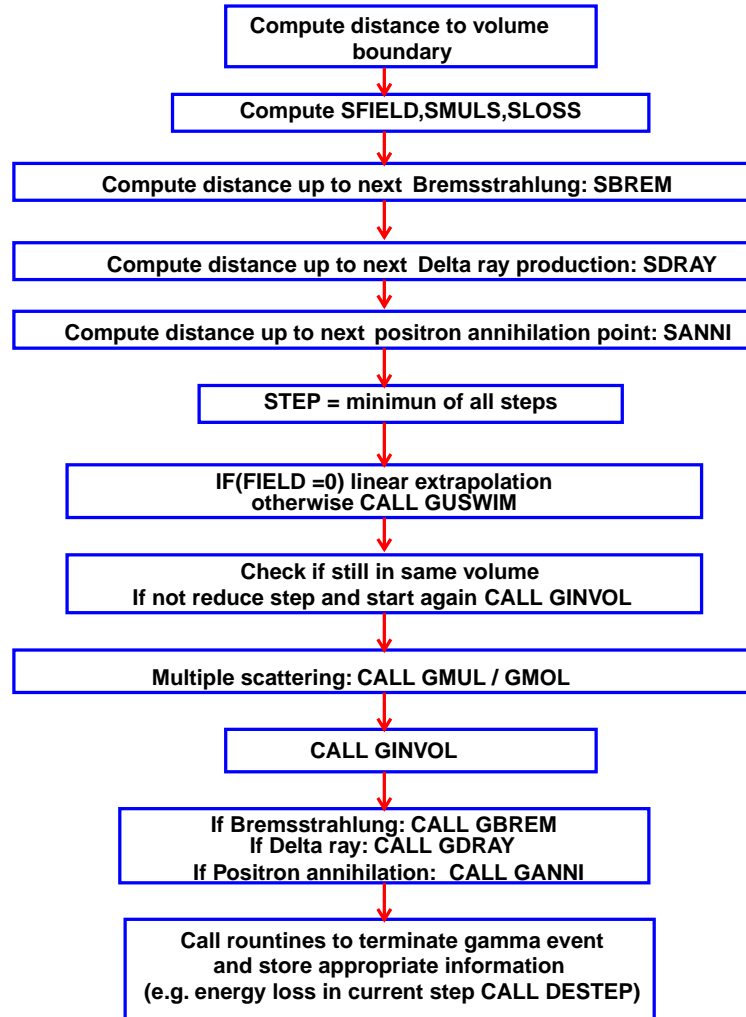


Figure 5.2: GTGAMA block diagram

placed inside the mother volumes. There are 13 predefined shapes, given in Appendix E with their default coordinate system, from which a detector may be built. For the DRAGON array, BOX, TRAP, TUBE and PGON volumes were used. Each volume is given a name and dimensions, through a call to the routine GSVOLU. The volume is then positioned in the  $x, y, z$  coordinate system **of the mother volume**, and rotated (if any is required) into the correct orientation with a call to GSPOS. Each shape is created in a default coordinate system (seen in the figures of Appendix E) and must

be rotated according to the mother volume reference system. For example, a TUBE volume is created with its length along  $z$ , if the tube is required to be positioned so its length is along the  $x$  of the mother volume then a rotation will be required.

In most cases only one daughter volume exists in any other mother volume. In Fig. 5.3 the DRAGON target box is depicted. Here the daughter trapezoidal volume is seen within the mother rectangular one. In this instance the rectangular volume is defined first and is filled with a certain medium type (e.g. vacuum). The trapezoidal volume is created second, filled with another medium (e.g. hydrogen), and placed within the rectangular one. The medium that fills the daughter volume has precedence here so in essence the trapezoidal hydrogen volume “cuts” out the vacuum of the rectangular volume.

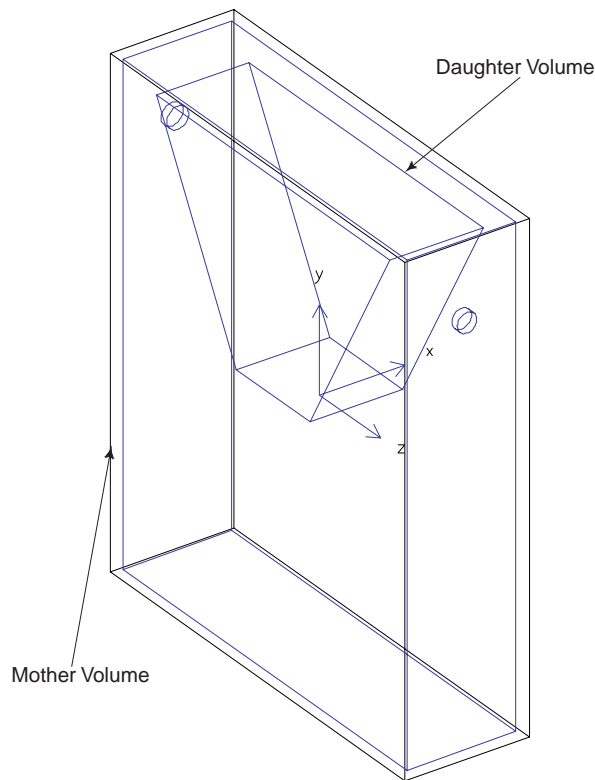


Figure 5.3: Example of a daughter in a mother volume

## 5.2 The Simulated DRAGON Gamma Ray Array

The GEANT gamma array was modelled as three main components, shown in Fig. 5.4: the individual BGO detectors one of which is shown, the gas target and the pumping tubes including lead shielding.

The simulation included all components of the gas target which are thick enough to significantly attenuate gammas. The outer aluminum box with the actual wall thickness, and the inner gas trapezoidal target of correct dimensions are both simulated. The simulation of the gamma array was later added to a much larger simulation of the full DRAGON spectrometer and therefore it was also necessary to include other components in and around the array. Openings in the ends of the inner gas target have been produced to simulate the 6 mm and 8 mm upstream and downstream pumping tubes respectively, as seen in Fig. 5.5. Pumping tubes have been simulated in three sections, as in the real target. Their dimensions (from upstream to downstream) are 1 cm, 0.9 cm, 0.8 cm for the upstream pipe and (downstream to upstream) 0.9 cm, 1.04 cm, 1.18 cm for the downstream pipe. The upstream pumping tube was simulated including a lead shield added during experimental runs to cut down on the effects of background coming from “mis-tuned” radioactive beam deposited on upstream target collimators. The lead shielding required moving two of the array’s BGO detectors back by 7.3 cm to allow the lead to fit. See Fig. 5.6, where the detectors moved are in red. The move reduced the solid angle coverage of the array from 92% to 89%.

The simulation of the individual gamma ray detectors themselves were inherited from the work of Peter Gumplinger of TRIUMF [67]. The detectors are represented in the simulation as hexagonal crystals measuring 7.62 cm long by 5.58 cm across the face. The scintillator material is covered by a layer of reflective material, 0.3175 cm thick on the face and 0.0355 cm on the sides, and then surrounded by an aluminum casing 0.0635 cm thick. The difference in thicknesses of the aluminum casing between Bicron and Scionix detectors was not implemented and may introduce a systematic error when the efficiency of the simulation is compared to measurements. Coupled to the BGO crystals are PMT’s, both of which are described as sensitive volumes (See §5.1.8), and are shown in Fig. 5.7. Gamma rays interact with the BGO detectors

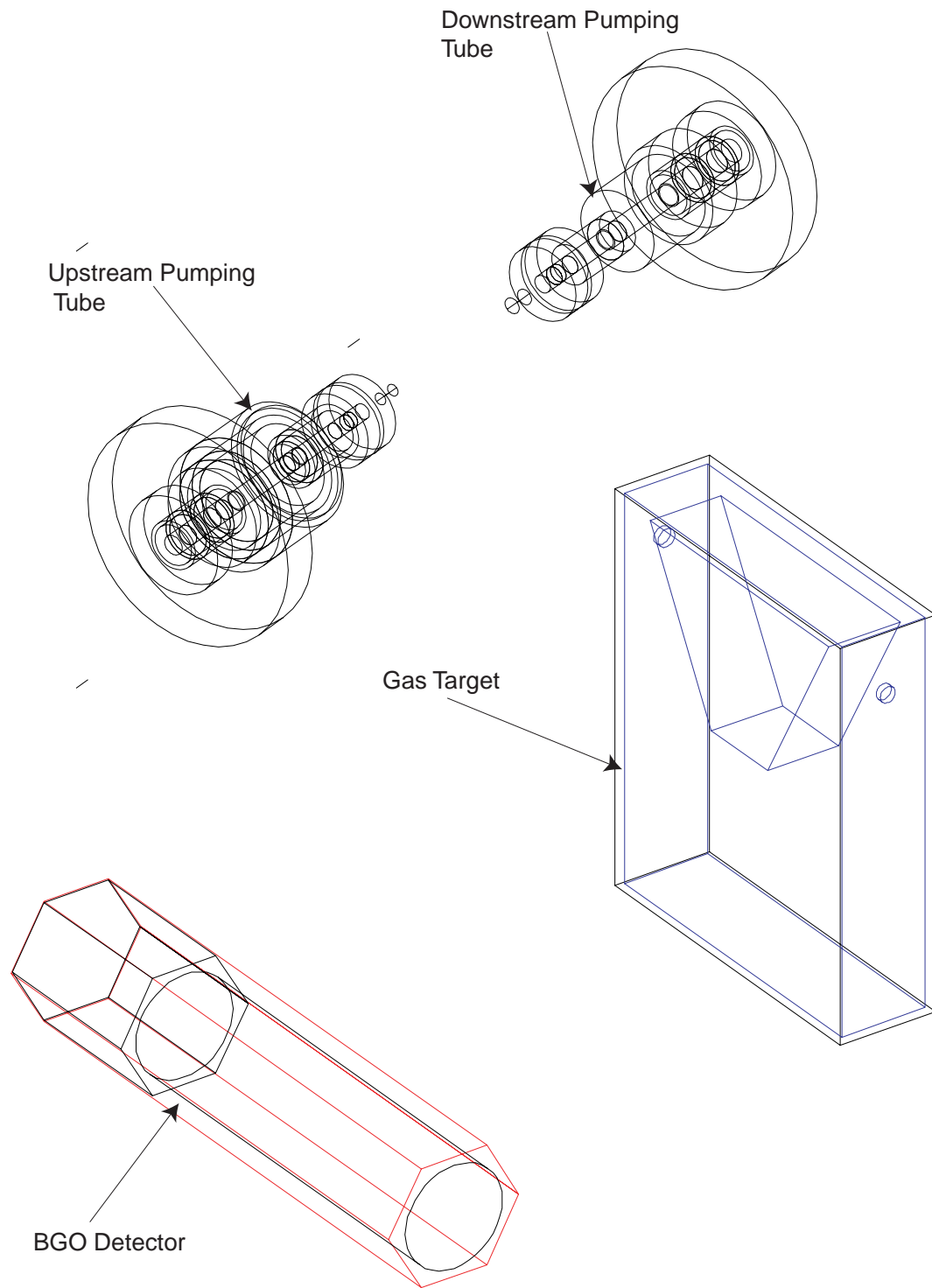


Figure 5.4: Three major components of the DRAGON gamma array

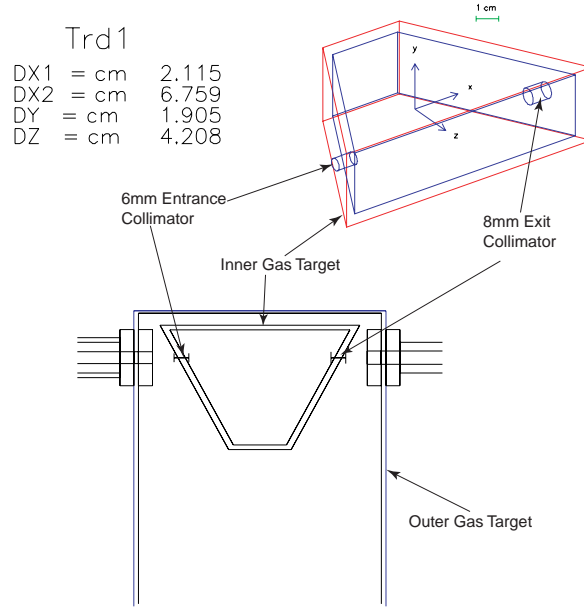


Figure 5.5: GEANT DRAGON inner gas target

and then produce light photons which are tracked through the crystal and into the PMT. The PMT's were made of very thin material, but in the simulation the actual dimensions were used for design purposes when space was a consideration.

The 30 BGO crystals in the array are of identical dimensions and so only one crystal, copied 29 times, was specified in the simulation. The crystals are described by 10 parameters, using the GEANT “PGON” shape. The crystals were placed in the simulation, and numbered according to increasing  $z$  and then increasing  $y$ . Each array half is made up of a central section consisting of ten detectors each, arranged in a 3,4,3 pattern so that the top row has three detectors which sit on a middle row of four which sit on a lower row of three. This pattern is duplicated on both sides. The remaining 10 crystals are arranged so that they “crown” the two sides. They are centred at  $x = 0$  and numbered in increasing  $z$ . The numbering scheme and detector arrangement is shown in Fig. 5.8.



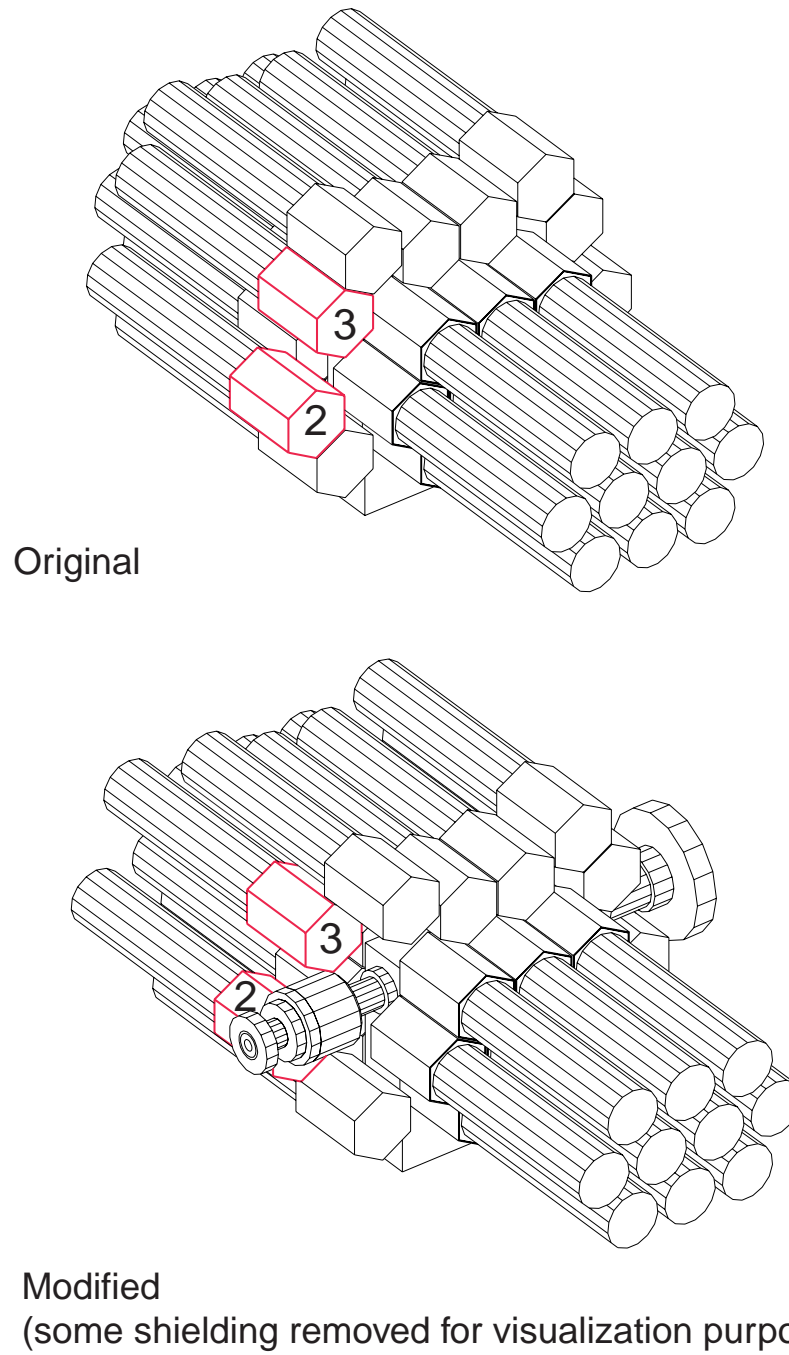


Figure 5.6: BGO Detectors 2 and 3 shown moved back to allow the lead shielding to be inserted

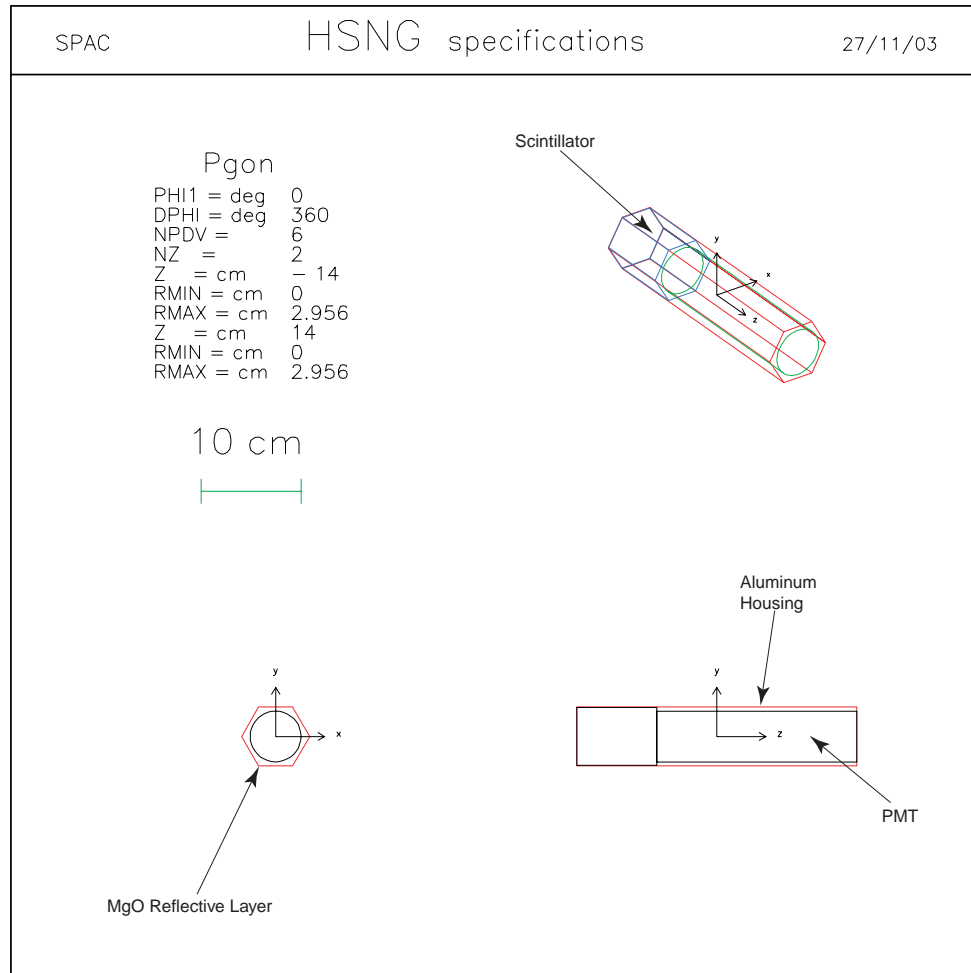


Figure 5.7: Simulated, individual BGO detectors showing the scintillator material, reflective coating, aluminum casing and PMT

### 5.2.1 Simulated Radioactive Gamma Source Characteristics

To approximate the radioactive sources used in the measurements, each source was simulated as a point source at a user specified position. A random number generator chose angles  $\theta$  and  $\phi$  to determine the direction in which the simulated gamma ray was released. Each gamma ray was varied in direction from the starting point and the total number of gammas was specified by the user. The angular distribution of the gamma rays was taken to be isotropic, approximating the actual source.

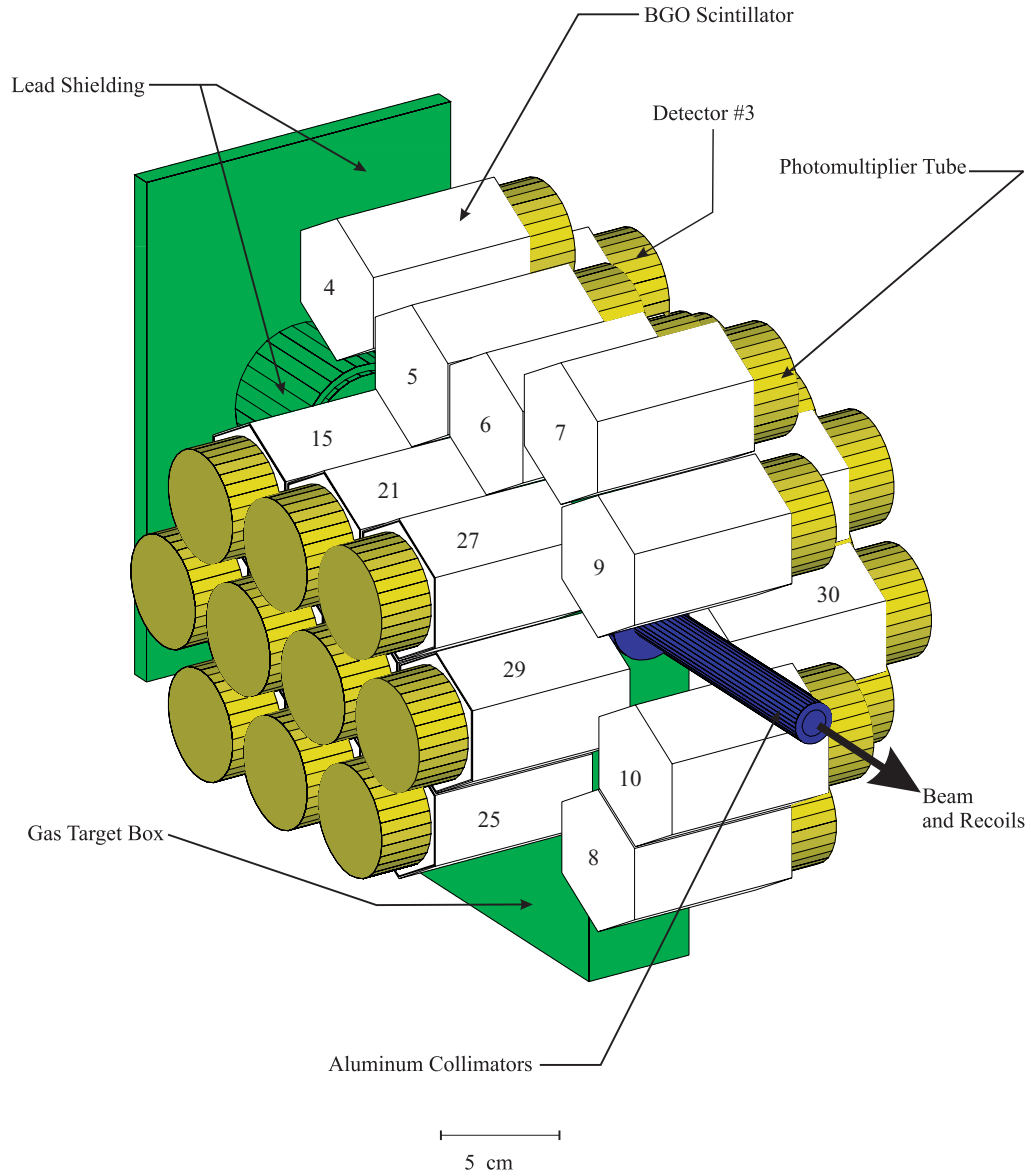


Figure 5.8: Arrangement of individual BGO detectors in the simulation along with the numbering scheme for the detectors. The length of the PMT's in yellow has been reduced for clarity. [68]

### 5.3 Running Simulations

The parameters used to describe the different components of the GEANT simulation can be entered by two different methods. Either hard-coded into the program or user specified. The user specified parameters are in a text file with the filename extension “.ffcards”. This method is convenient for testing and development when one parameter may be changed several times. Detector geometry, aluminum wall thicknesses, and collimator diameters, are examples of parameters which needed to be changed often. Once these types of parameters were established their values were hard-coded. Other parameters such as gamma ray energies, source positions, number of events to trigger, always required changes.

While doing the efficiency simulations the most varied records in the ffcards file were:

1. RUNG giving a unique descriptor filename for the resulting histogram file that is created,
2. TRIG used to specify the number of gamma events which will be triggered for a simulation run,
3. RNDM specifying the random seed value for the random number generator. (If the random seed is kept the same then the resulting histograms that are produced as output will often have the same appearance, assuming other conditions are constant.),
4. KINE which determining the simulation kinematics, is an 11 parameter record giving the source position in  $x, y$ , and  $z$ , and source energy

Many other parameters in the ffcards file were changed very rarely. A more detailed description of these parameters are shown in the example ffcards file in Appendix D.

# Chapter 6

## Data Analysis and Results

### 6.1 Efficiency Measurement Technique

The gamma rays of interest for the DRAGON experimental program range in energy between 1-10 MeV [1]. Therefore, it is necessary to have an efficiency calibration of the array in a similar energy range. Radioactive sources of high precision exist and are readily available for energies less than 3 MeV. Calibration at higher energies is normally done through beam experiments using proton capture reactions on solid targets, as described in the works of Mehroff et al. [69], Kolle et al. [70], Elekes et al. [71], Yoshimori et al. [72], Drake et al. [73], Waibel and Grosswendt [74], and Dryak et al. [75]. The ISAC accelerator was not designed to deliver protons. Instead, a method using radioactive gamma ray sources, similar to the methods of [70] and [75], was developed and is described below.

Reactions producing high energy gammas of interest are available from two sources. The first is from intimately mixed powders of  $^{241}\text{Am}$  and  $^9\text{Be}$  [76]. The alpha decay of  $^{241}\text{Am}$  impinges on the  $^9\text{Be}$  target, and initiates  $^9\text{Be}(\alpha, n)^{12}\text{C}^*$ . The  $^{12}\text{C}^*$  decays to the ground state through emission of a 4.44 MeV gamma (See Fig. 6.1). The alpha particle emitted from  $^{241}\text{Am}$  has only sufficient energy to populate the first excited state of  $^{12}\text{C}$  [10].

The second gamma source is an intimate mixture of  $^{244}\text{Cm}$  and  $^{13}\text{C}$ . The  $^{244}\text{Cm}$  produces alpha's which impinge on the  $^{13}\text{C}$ , and initiates  $^{13}\text{C}(\alpha, n)^{16}\text{O}^*$ .  $^{16}\text{O}^*$  decays

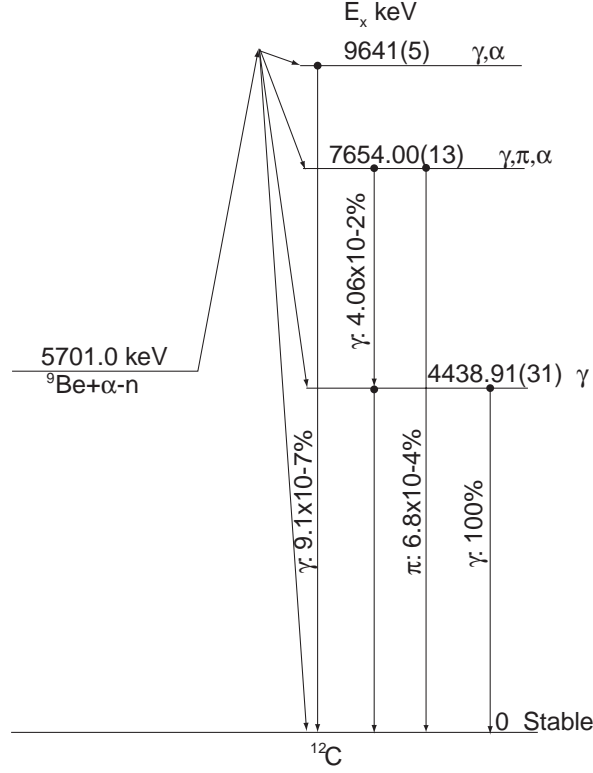


Figure 6.1: Gamma levels in the  ${}^9\text{Be}(\alpha, n){}^{12}\text{C}$  reaction [10]

by emission of a 6.13 MeV gamma to the ground state [77] (See Fig. 6.2). The 5.80 MeV alpha produced by  ${}^{244}\text{Cm}$  is below the threshold for excitation of other gamma emitting states in  ${}^{16}\text{O}$  [11]. The result is a mono-energetic source of 6.13 MeV gammas. The difficulty with these sources is that they are generally used for neutron calibration and not gamma calibration, so the rate of gamma emission from these sources is not specified by the manufacturers to better than 20% [78]. To resolve this issue a cross calibration technique, using a NaI detector of known efficiency, was employed to determine the gamma rate of these sources with sufficient accuracy.

## 6.2 Gamma Source Activity Calibration

Using a method similar to that described in [12], the gamma source activity was measured using a standard  $3'' \times 3''$  NaI detector. The sources were positioned at 10

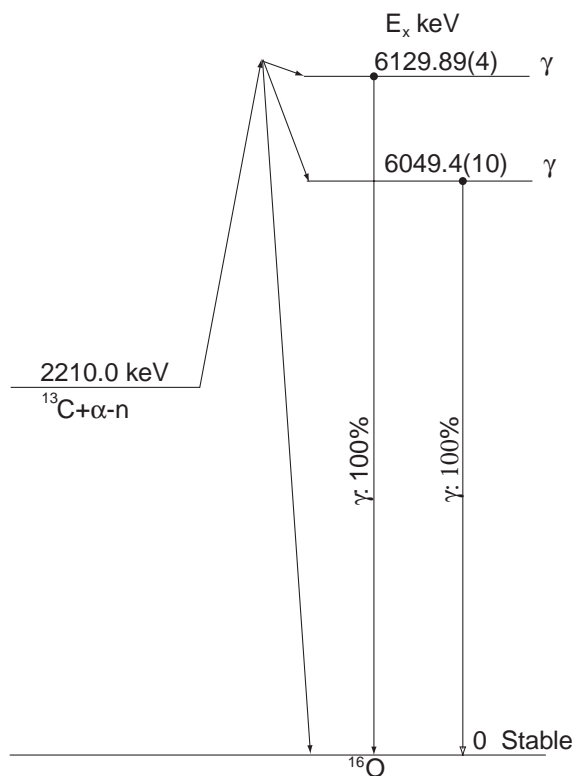


Figure 6.2: Gamma levels in the  $^{13}\text{C}(\alpha, n)^{16}\text{O}$  reaction [11]

cm from the detector on a mount which insured that the sources were centred axially over the detector face. The setup is shown in Fig. 6.3.

The detector used was a Harshaw “Integral Line” NaI(Tl) Type 12S12. The electronics (Fig. 6.4) for the setup consisted of an Ortec 572 shaping amplifier, scintillator power supply, Nucleus MCA card and the Nucleus’s own data acquisition software. The MCA card had a 100MHz Wilkinson ADC on board. The positive unipolar output from the Ortec amplifier was connected directly to the MCA card, and 900 volts was applied to the detector from the power supply.

Measurements with four sources were taken. Two measurements used the  $^{244}\text{Cm}^{13}\text{C}$  6.13 MeV and  $^{241}\text{Am}^9\text{Be}$  4.44 MeV sources, and two additional measurements used well calibrated  $^{137}\text{Cs}$  662 keV and  $^{60}\text{Co}$  1.33 MeV sources to test the setup and analysis procedure. The measured activities of  $^{137}\text{Cs}$  and  $^{60}\text{Co}$  sources were compared to the manufacturer quoted source activities, corrected for radioactive decay lifetimes. The

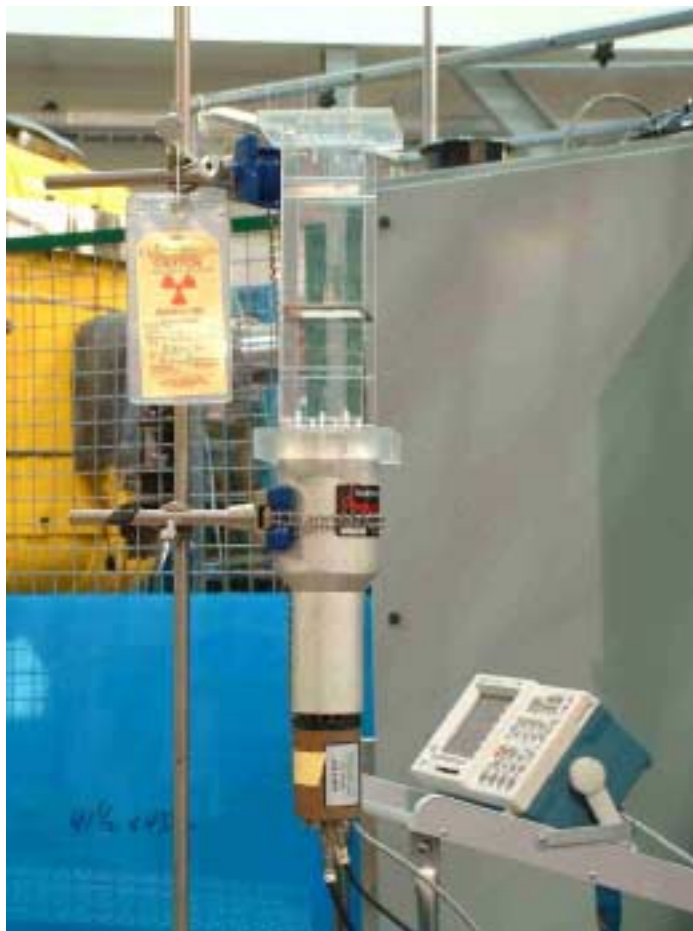


Figure 6.3: A photo of the source calibration setup showing the detector stand and source mount. The cylindrical source is visible on the shelf just to the right of the yellow radiation warning sign, 10 cm above the face of the 3" diameter detector.

quoted and measured activities were found to be in agreement within statistical errors as, shown in Table (6.1).

### 6.2.1 Fitting By Monte Carlo Methods

To extract efficiencies, gamma spectra fitting has usually been done using a sum of Gaussians to fit the full energy peak plus polynomials to fit to the continuum. For simple cases where the full energy peak is well separated from other peaks, and from the Compton continuum, this method is appropriate. Good separation of the peak



Source	Energy (MeV)	$N$ (Counts/s)	$N_{quoted}$ (Counts/s)	$\Delta N$ (Counts/s)
$^{137}\text{Cs}$	0.662	188474	-	4814
$^{137}\text{Cs}\dagger$	0.662	-	189020	6993
$^{60}\text{Co}$	1.33	13576	-	360
$^{60}\text{Co}\dagger$	1.33	-	14361	539
$^{241}\text{Am}^9\text{Be}$	4.44	24372	-	1786
$^{244}\text{Cm}^{13}\text{C}$	6.13	2618	-	286

Table 6.1: Source activities of various sources by NaI cross calibration technique. Source activities and their respective  $\sqrt{N}$  errors, denoted by  $\dagger$ , are as expected from activity quoted by the source manufacturer.

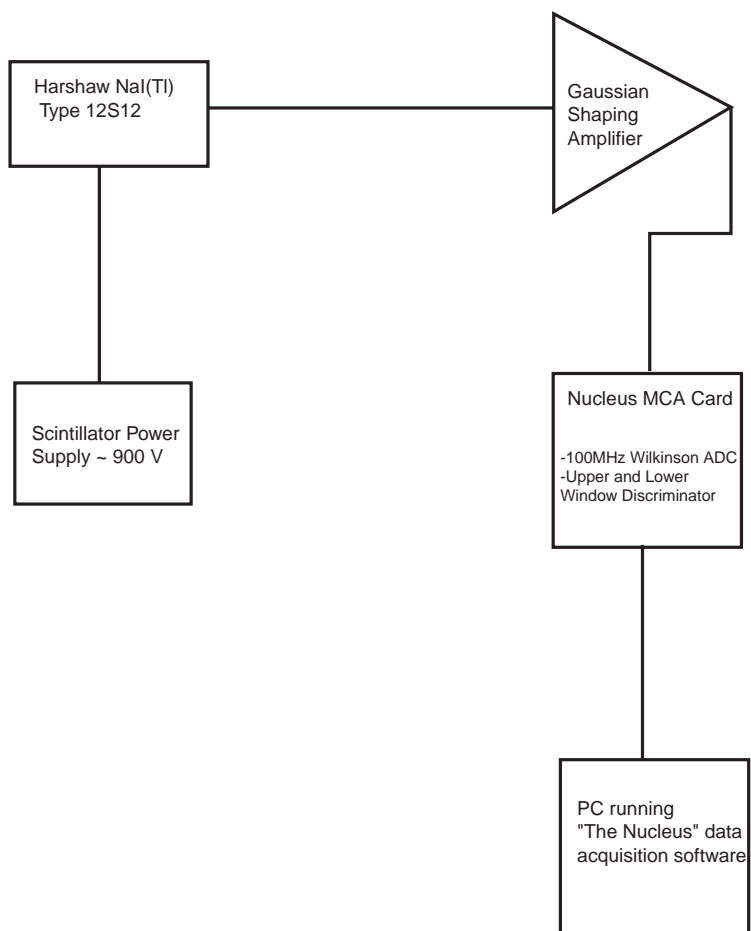


Figure 6.4: Electronics diagram for the NaI scintillator setup

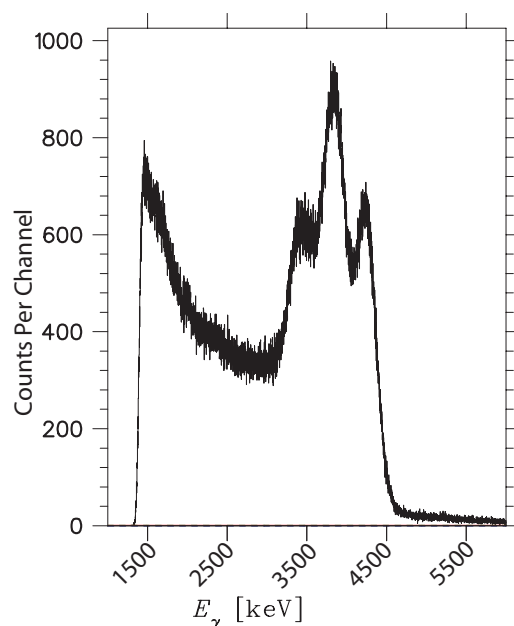


Figure 6.5: High energy sources produce a complicated spectrum of a sum of Gaussian and Compton edges

from Compton can be seen in scintillators for monoenergetic, low energy gamma sources such as  $^{137}\text{Cs}$ . In these cases it is sufficient to fit the peaks with a Gaussian and sum in a sloped line or quadratic polynomial to account for the background under the peak. A slightly more complicated situation arises if the fit is to include a fraction of the Compton continuum as well as the Compton edge and full energy peak. In this situation an additional polynomial is required to fit the continuum, the Compton edge, and the background, in addition to the Gaussian used for the full energy peak. In the analysis of high energy gamma sources a complication arises when pair production becomes possible. One or both of the pair may escape the detector producing secondary peaks separated by 0.511 MeV (first escape peak) and 1.022 MeV (second escape peak) below the full energy peak. In this situation, shown in Fig. 6.5, the Compton edges lie underneath the escape peaks creating a complicated sum of Gaussian peaks and Compton edges.

To fit such a spectrum one would need to fit 3 Gaussians plus a polynomial of high order to give a good  $\chi^2$ . This would be a “blind” type of fit because the shape of the

polynomial would be an approximation with no physical basis. Even so, a polynomial plus the Gaussians may still not give a reasonable fit and more importantly it would be impossible to tell if this arbitrary shape was approximating the correct physical processes. Because a high order polynomial could be virtually any shape there is no restriction to determine the ratio of the areas under the peaks, i.e. there are too many free parameters. To accurately find the areas under the peaks some restrictions must be placed on the fit from theory, by fixing certain parameters. The relative heights of the peaks, peak-to-Compton ratio, and shape of the Compton continuum/edge parameters can be fixed by running a Monte Carlo (GEANT in this case) simulation to predict the response of the detector. Monte Carlo methods have been proven to provide accurate response functions for NaI crystals to various gamma energies as shown by [79] and [80]. The response function of the Monte Carlo is in essence a complicated function (with definite physical basis) which can be adjusted to accurately represent the data to be fitted. If resolution is left out of the Monte Carlo (which it was initially) the result is the “pure” response of a detector to physical processes alone. Therefore, the fitting process can involve two parameters: (1) the overall normalization of the spectrum and (2) the resolution of the detector. Resolution, which was a free parameter and assumed to be purely Gaussian, was added during the fit by convolving the Monte Carlo with a Gaussian of specific width  $\sigma$ . Additional functions were also added to the fit to represent processes not modelled in the Monte Carlo, such as linear background to model neutron detection. Additional free/fixed parameters were included in the fit to represent detector gain and zero offset.

The quantity to be found by fitting is the data area under the full energy peak. The Monte Carlo spectrum predicts the relative areas of the full energy, escape peaks and Compton events from the ratios defined by the physics contained in GEANT. The lack of resolution effects in the simulation made the area under the full energy peak easy to find because it was contained in one single channel, therefore the *height of the Monte Carlo peak is its area*. To find the data area an overall normalization factor was fit which was dependent on the resolution of the detector. As each channel of the Monte Carlo was convolved by a Gaussian the overall normalization was changed to maintain the correct relative areas. Six stages in the fitting procedure are shown

in Fig. 6.6. The fit that minimizes  $\chi^2$  produces a value for the overall normalization. Multiplying the overall normalization by the single-channel peak area of the Monte Carlo gave the absolute full energy peak area of the data.

Fitting was done using a spectrum to spectrum fitting program [81]. The fitting program took, the data file, the Monte Carlo spectra, and additional functions used for background subtraction, as input. These were a linear function to represent neutron background and an exponential function to represent cosmic rays and other low energy gamma rays from the source. The program used a Levenberg-Marquardt [82], [83] algorithm to do the fitting. The fitting program convolved each of the Monte Carlo spectrum channels with Gaussian noise of appropriate sigma to represent resolution effects, and an overall normalization of the data. Other fitting parameters included detector gain and zero offset needed to avoid binning problems. The fitting results for the four different gamma sources are shown in Fig. 6.7.

## 6.2.2 Analysis of NaI Data

With the closest distance of (10 cm) and strongest source ( $^{137}\text{Cs}$ ) pile-up events, requiring analysis, occurred in the NaI detector. See Fig. 6.8. The region  $A_r$  to the right of the peak is only pile-up events. Within the region  $A_p$  are only pile-up events involving two full energy gammas. The rest of the region  $A_r$  includes both the pile-up of several Compton scattered gammas and Compton scattered gamma plus a full energy gamma. Pile-up also existed to the left of the region  $A_r$  but this cannot be accurately approximated. Pile-up was unavoidable because of the unavailability of a weaker source at TRIUMF. Because a fraction of the pile-up events in  $A_r$  were indeed good full energy events, it was necessary to make some estimate as to the number of these events which should be included in the area under the photopeak. The number chosen, which was added to the counts in the full energy peak, was the total counts in the pile-up peak which was fit with a Gaussian, plus one half of all events to the right of the full energy peak minus those in the pile-up peak. It must be the case that any event to the right of the full energy peak must be a pile up event but the mechanism for this pile up does not always include a full energy gamma. It may be the case that

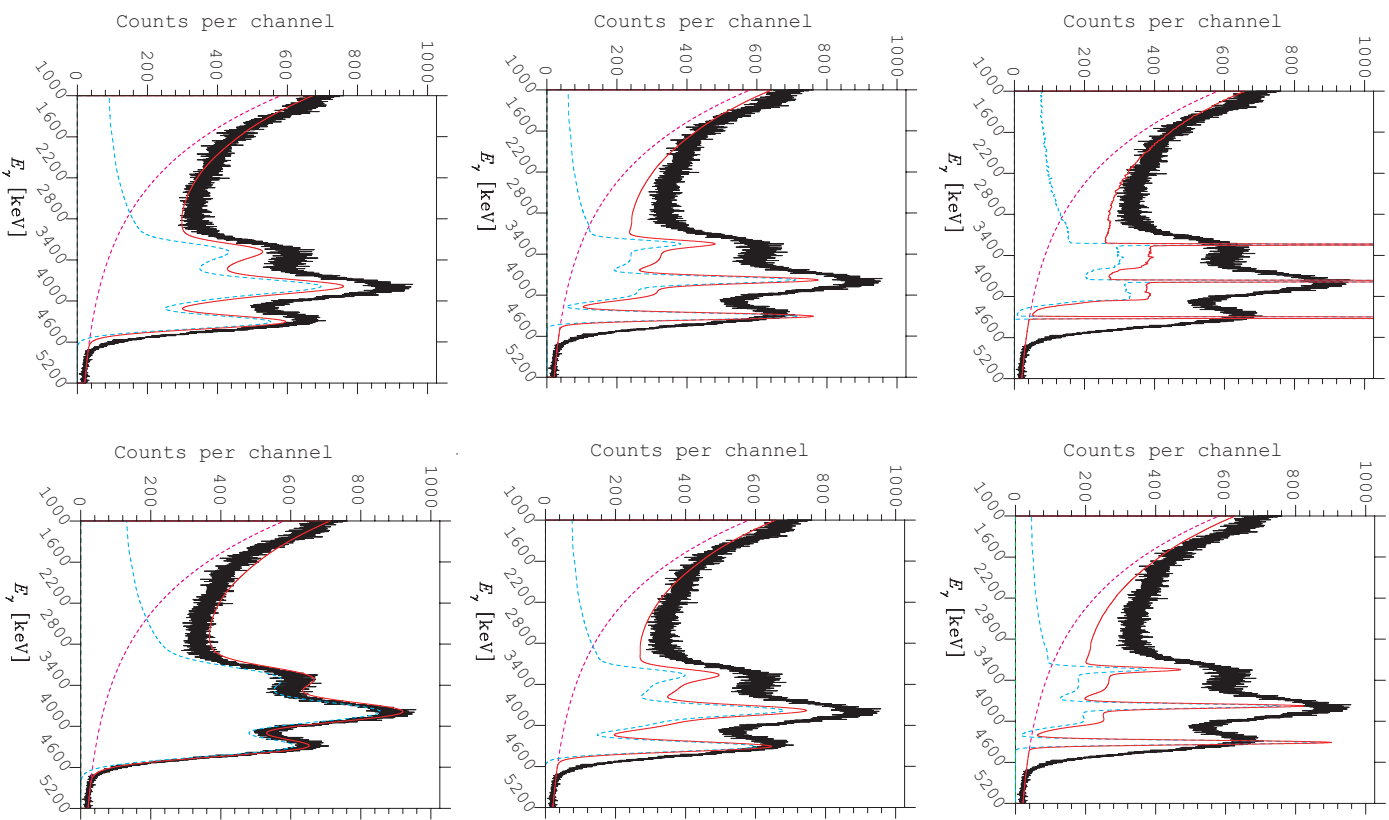
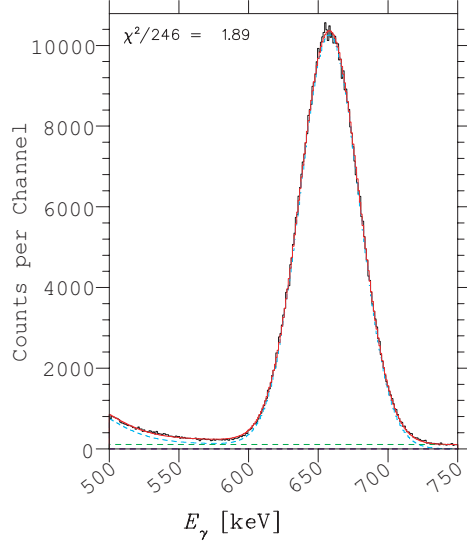
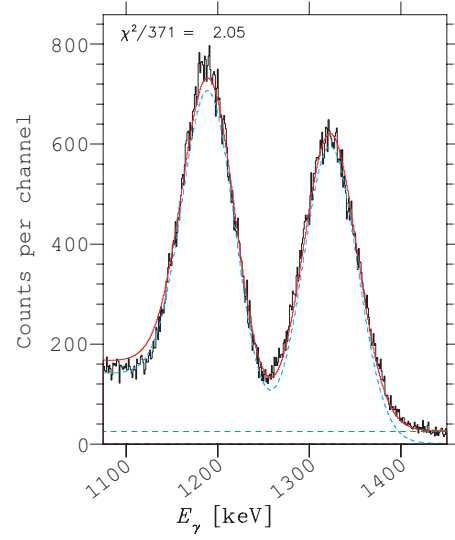


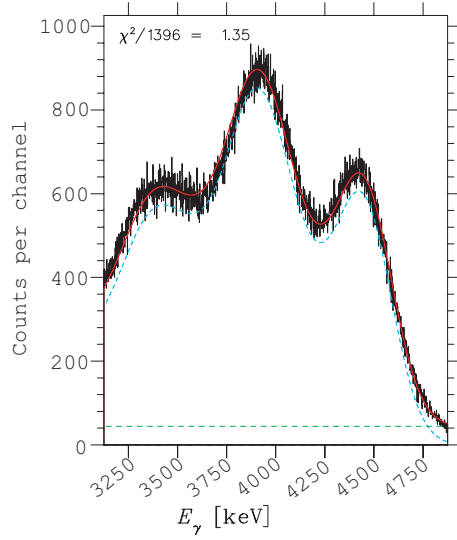
Figure 6.6: A Monte Carlo fitting example. Data(black) is overlaid by the Monte Carlo “fit function” (red) and an exponential function (magenta) to account for the low energy gammas, higher energy cosmic rays, and neutrons from the source.



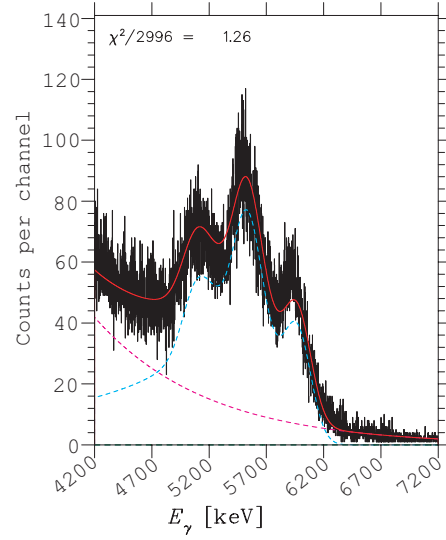
(a) Fit  $^{137}\text{Cs}$  10 cm from a single NaI detector



(b) Fit  $^{60}\text{Co}$  10 cm from a single NaI detector



(c) Fit  $^{241}\text{Am}^9\text{Be}$  10 cm from a single NaI detector



(d) Fit  $^{244}\text{Cm}^{13}\text{C}$  10 cm from a single NaI detector

Figure 6.7: Fitting results of the Monte Carlo fitting procedure for NaI source calibration

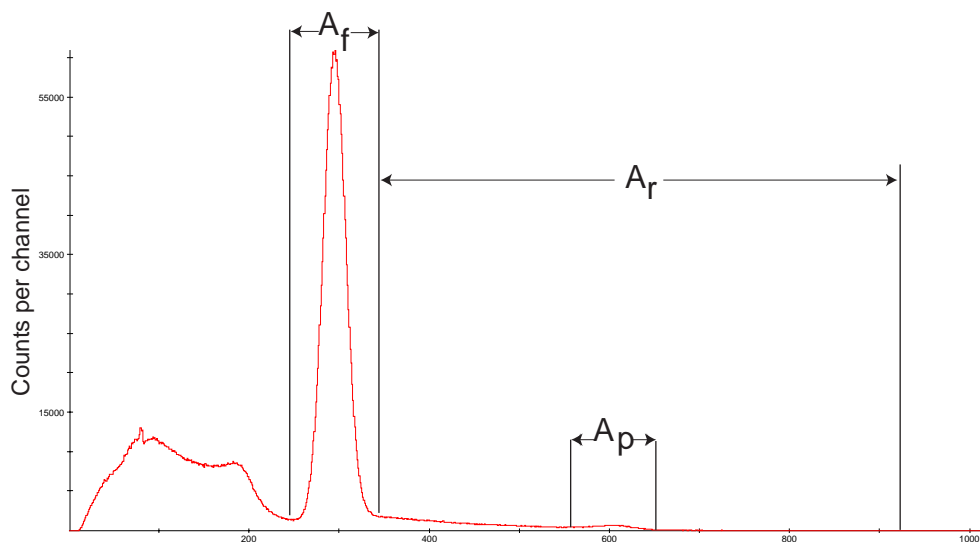


Figure 6.8:  $^{137}\text{Cs}$  spectrum showing regions used in the calculation of pile-up correction. See text for details.

some of these events came from the addition of several Compton scattered gammas or it may be a full energy gamma plus one or more Compton scattered gammas. The result is that some estimate of the fraction of events that included a full energy gamma must be made, so a number of one half was chosen to approximately omit the Compton pile-up which would normally occur outside the full energy peak. The source activity is then,

$$N = \frac{A_f + A_p + 0.5(A_r - A_p)}{t\tau\mathcal{E}_t\mathcal{R}} \quad (6.1)$$

Where,

- $A_f$  = Area under the full energy photopeak
- $A_p$  = Area under the pile-up peak(s)
- $A_r$  = Area to the right of the full energy peak
- $t$  = data collection time
- $\tau$  = fractional system live-time

$\mathcal{E}_t$  = NaI total detector efficiency

$\mathcal{R}$  = NaI simulated peak-to-total ratio

In principle, one could find the activity of an unknown source by measuring the area under the full energy peak with a NaI scintillator of known total efficiency and then, if it is well known, correct for the ratio of events in the peak compared to the rest of the spectrum (i.e. the peak-to-total ratio). It is normally more difficult to extrapolate a source spectrum to zero pulse height (i.e. to find the total activity directly) rather than measuring the area under the peak and then making a correction for the peak-to-total [12]. The measured peak counts represents only a fraction of the total source activity, therefore measuring *total source activity* using total efficiency must include the events in the peak *plus* all other source events to the left of the peak.

NaI has been studied by many groups and experimental total efficiency values have been published by Green and Finn [84], Coop and Grench [85], and Heath et al. [86] for energies up to 3 MeV. Chinaglia and Malvano [87] have reported efficiencies for up to 4 MeV, Van Oostrum and Meijer [88] for energies up to 6 MeV, Lazar [89] [90] up to 7.5 MeV, and Waibel and Grosswendt [74] up to 12 MeV. Experimental peak-to-total ratios have also been published by Chinaglia and Malvano [87], Heath et al. [91], Vegors et al. [92], Leutz et al. [93], and Mishra and Sadasivian [94]. Efficiency calculations for 3"  $\times$  3" crystal coming from a point source 10 cm from the face of a bare crystal have been tabulated by Wolicki et al. and reported by Wolicki et al. [95], Zerby and Moran [96], Weitkamp [97], Giannini et al. [98], Berger and Seltzer [79], Seltzer and Berger [99], Miller and Snow [100], and by Grosswendt and Waibel [101] using Monte Carlo methods. Peak-to-total ratios can also be extracted from the works of these authors as well as from the tabulated values of Hornyak et al. [13]. Irfan and Prasad [102], and Selim et al. [103] [104] have made calculations of the efficiencies of various sizes of crystals and source geometries using analytical techniques.

The total efficiency of a 3"  $\times$  3" NaI bare crystal and aluminum encased crystal was calculated using GEANT and compared to the tabulated Monte Carlo calculations of Wolicki et al. [95], and analytical calculations of Selim et al. [103] (See Fig. 6.9). It was found that the calculations of [95] matched the bare crystal GEANT simulation. These



values deviated from the analytical calculations of [103] by 4-8%. The  $3'' \times 3''$  crystal used in these measurements was encased in aluminum which differed from the thin aluminum casing simulated in [103] and bare crystal of [95]. It was decided that the GEANT calculations that included an aluminum casing would be used, as this calculation best described the experimental setup. The excellent agreement between the two Monte Carlo bare crystal calculations (i.e. [95] and GEANT) gave further support to the correctness of the GEANT calculations.

The values describing the fraction of the events found in the full energy peak as compared to the rest of the spectrum, for various energies in a  $3'' \times 3''$  NaI crystal have been tabulated experimentally by Heath [12], and by Hornyak et al. [13] using Monte Carlo methods. These results were graphed in Fig. 6.10 along with the results of the GEANT NaI simulation. The peak-to-total values of Fig. 6.10 show a variance from one author to another. An average of these values was taken for the values of  $\mathcal{R}$  used in the calculation of the source activity. The error on  $\mathcal{R}$  was taken as the variance in peak-to-total values of Fig. 6.10. The total error in  $N$  (e.g. Table (6.1)) was found by adding in quadrature the statistical error of the areas in the numerator plus the error in  $\mathcal{R}$  (i.e. peak-to-total uncertainty) in quadrature. The error in  $N$  was dominated by the peak-to-total uncertainty,  $\mathcal{R}$ .

The activities and associated errors for the source measurements and simulations are summarized in Table (6.1). Included in the table are also the activities for the sources as quoted by the source manufacturer, after correcting for several half-life decays. The uncertainties in activity were 3.7% for both  $^{137}\text{Cs}$  and  $^{60}\text{Co}$  sources.

### 6.3 Efficiency of a Single BGO Detector

A comparison between simulation and data was done for a single BGO detector before performing similar measurements on the full gamma ray array. With the single detector system a comparison could be made between the measured and simulated results for the intrinsic detector efficiency and properties of the aluminum casing and reflector, while avoiding the complications of geometry effects and shielding by neighbouring detectors.

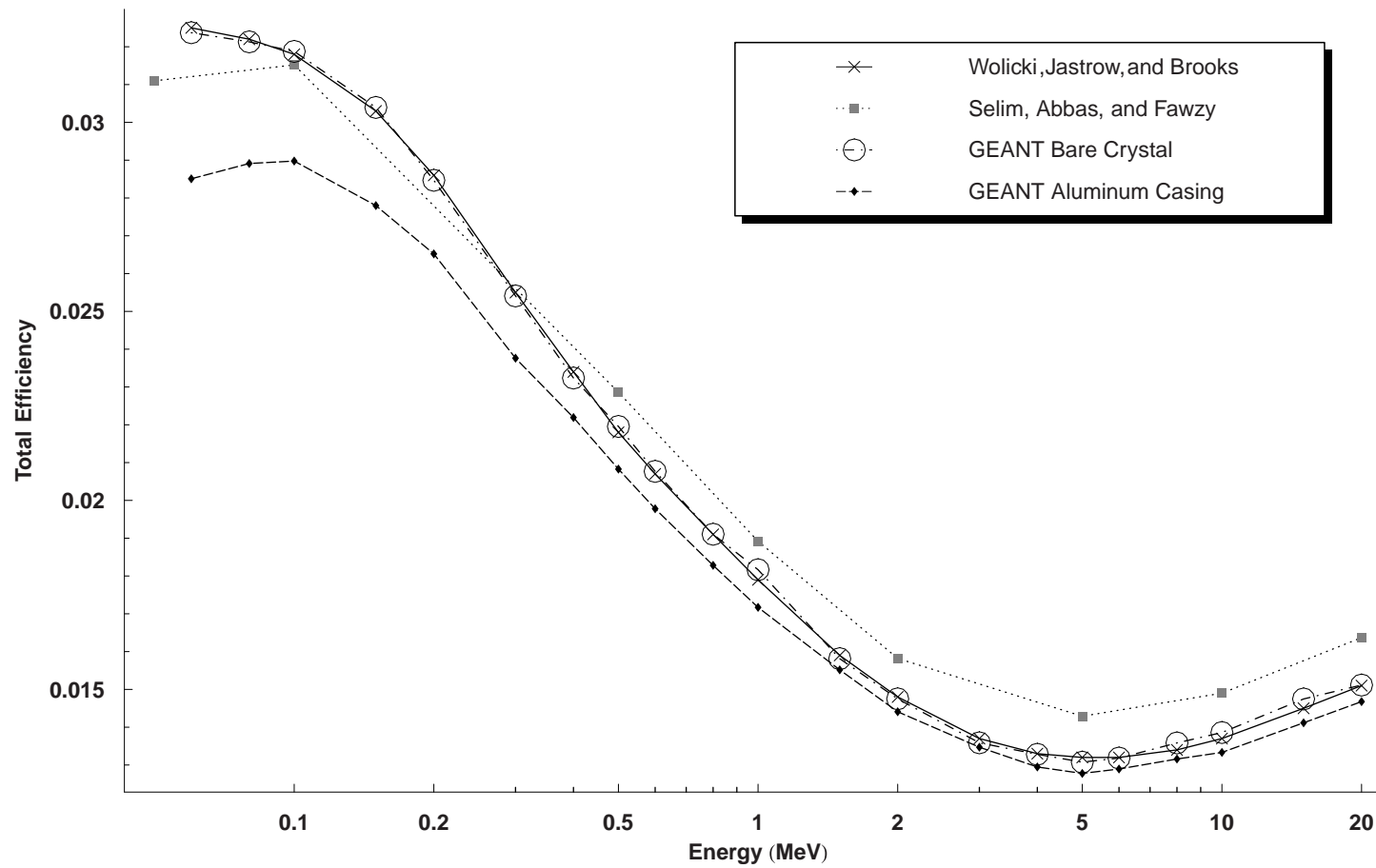


Figure 6.9: Comparison of published NaI *total efficiency* values of [95] and [103] to GEANT calculation. The values of [95] were measurements of a bare crystal while the measurements of [103] included a thin aluminum casing. The “GEANT bare” crystal resembled that of [95] while “GEANT aluminum” was more indicative of the actual detector used in the measurement

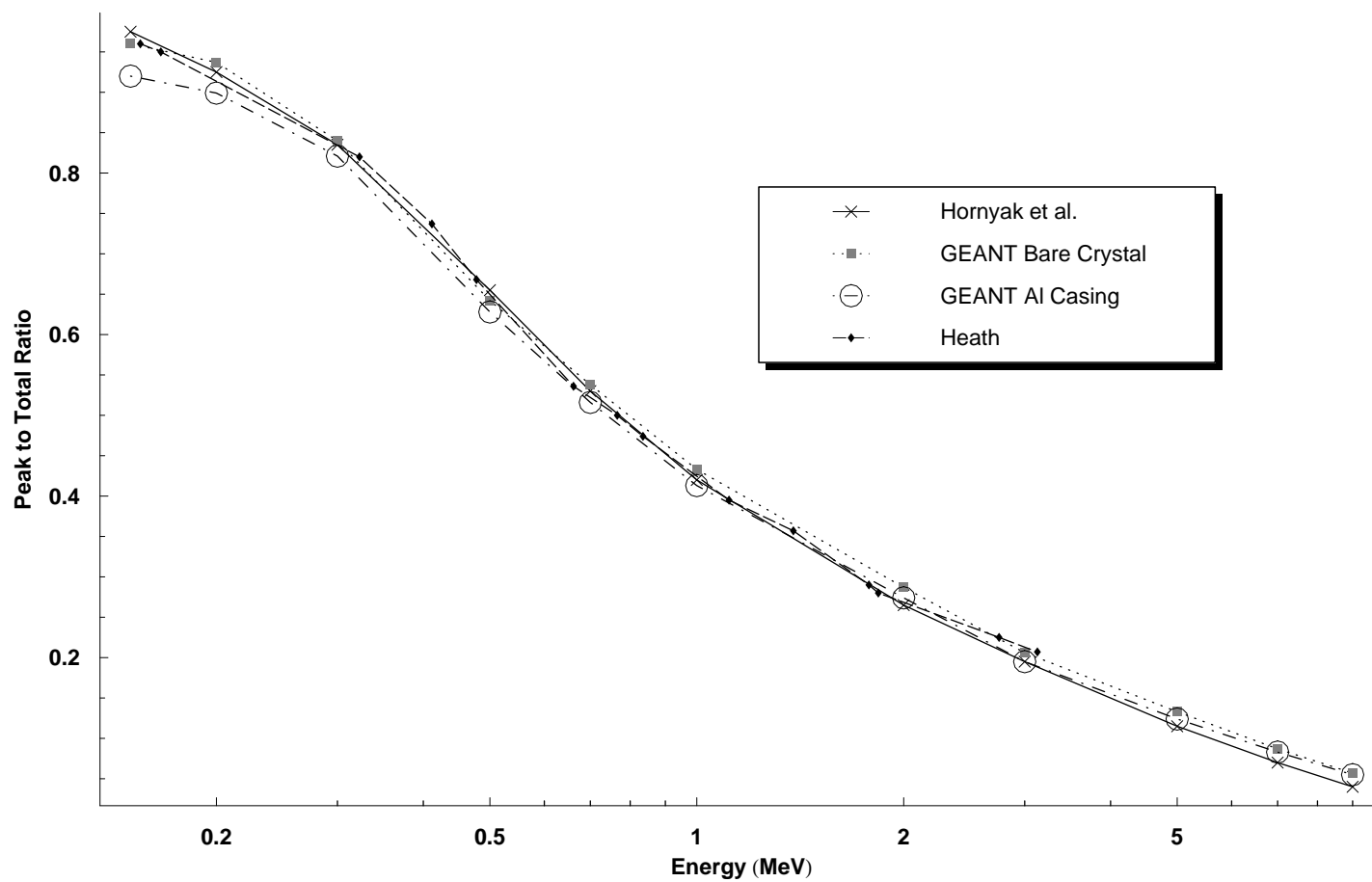


Figure 6.10: Comparison of published NaI *peak-to-total ratios* values of [12] and [13] to GEANT calculation.

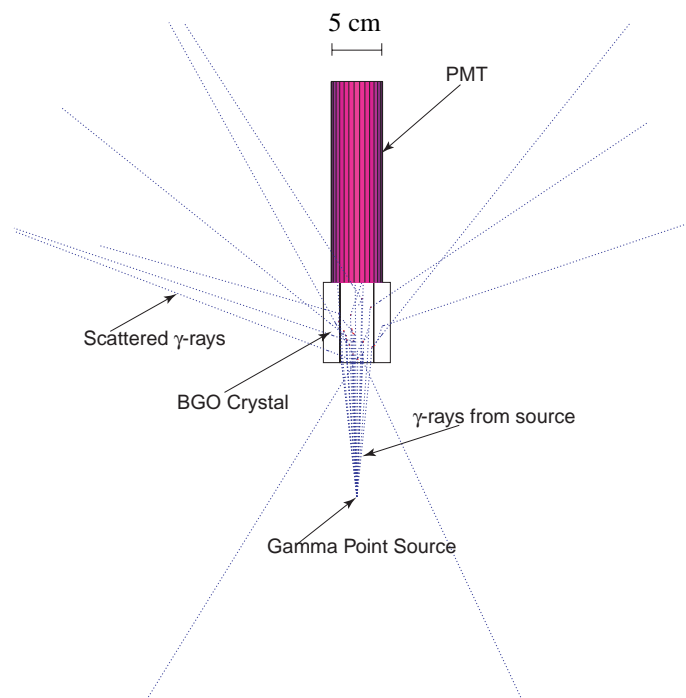


Figure 6.11: Simulated source centred 10 cm axially from the face of the detector. This figure is produced by the graphical interface of the GEANT simulation program. It shows the gamma point source, as well as the tracks (the dashed lines) produced by gammas which come from the source and scatter in the crystal.

### 6.3.1 Single Detector Simulation Data

To simulate a single detector the full gamma array simulation was modified by removing all other components and detectors from the system. The only modified file was the UGEOM.F Fortran source (See §5.1.8) file which determines geometry. All other routines were left untouched. Simulations of 100000 source emitted gamma rays were run for each point source (See §5.2.1) positioned 10 cm, axially from the detector face, in the geometry shown in Fig. 6.11.

Gamma sources of energy 662 keV, 1.33 MeV, 4.44 MeV and 6.13 MeV were used. PAW (Physics Analysis Workstation) [105], callable subroutines from the CERN library were used to histogram and analyze the simulated data. Detector resolution was deliberately left out to avoid the unnecessary complication of having to fit the simulated peaks with Gaussian functions. All necessary information regarding full

energy efficiency was extracted from a single channel whose area was therefore the height of the peak (See Fig. 6.12).

### 6.3.2 Single BGO Gamma Ray Photopeak Efficiency Measurements

One BGO detector was taken from the array and mounted in place of the NaI detector used in the source measurements of §6.2. The electronics used in this test were identical to those used in the NaI tests (See Fig. 6.4) except for high voltage values. Four sources ( $^{137}\text{Cs}$  ,  $^{60}\text{Co}$  ,  $^{241}\text{Am}^9\text{Be}$  ,  $^{244}\text{Cm}^{13}\text{C}$  ) were used to determine the efficiency of a single BGO detector at energies of 0.662, 1.33, 4.44 and 6.13 MeV. Each source was placed at a distance of 10 cm from the BGO detector face so that it was in line axially with the face of the detector. Data was collected to achieve statistics better than 1% in the full energy peak. The dead time and collection time were recorded.

Each source spectrum was fit using the same method described in §6.2.1 for fitting the NaI spectra. In addition to the Monte Carlo generated response function, an exponential function and linear function to represent possible background from neutrons or cosmic rays, which may be worse in the BGO detector, were added to the fit. The results of the fits are shown in Fig. 6.13. At these energies the contribution of neutrons turned out to be small compared to the gamma detection rate [106]. The area under the curve  $A$ , and the source activity  $N$  from Table (6.1) is used to find the efficiency of the detector,

$$\mathcal{E}_D = \left( \frac{A}{t\tau N} \right) \quad (6.2)$$

Where,

$A$  = Area under the photopeak

$t$  = data collection time

$\tau$  = fractional system live-time

$N$  = radioactive source gamma activity from Table (6.1)

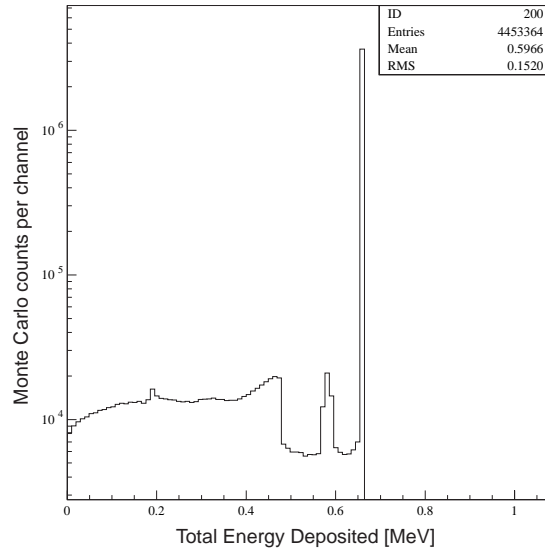
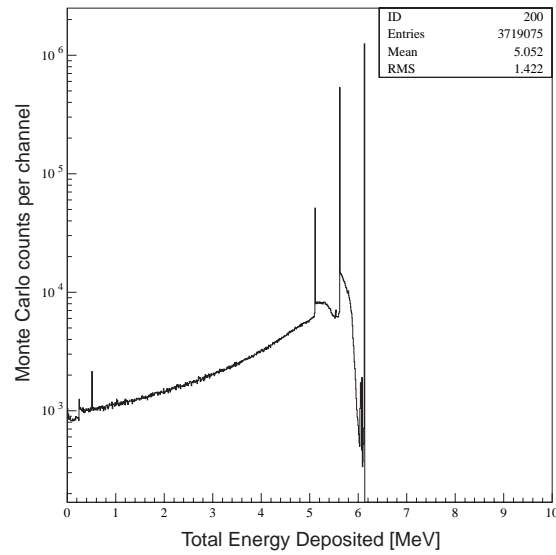
(a) Response from a 0.662 MeV source ( $^{137}\text{Cs}$ )(b) Response from a 6.13 MeV  $^{244}\text{Cm}^{13}\text{C}$ 

Figure 6.12: Simulated spectra of pulse height vs. energy for a single BGO detector. The height of the full energy peak represents the area under the peak.

Source	Energy (MeV)	$\mathcal{E}_D$ (%)	$\Delta\mathcal{E}_D$	$\mathcal{E}_S$ (%)
$^{137}\text{Cs}$	0.662	1.200	0.030	1.192
$^{60}\text{Co}$	1.33	0.851	0.019	0.841
$^{241}\text{Am}^9\text{Be}$	4.44	0.418	0.031	0.453
$^{244}\text{Cm}^{13}\text{C}$	6.13	0.349	0.039	0.390

Table 6.2: Efficiency of a single BGO detector for various gamma ray energies where  $\mathcal{E}_D$  denotes the efficiency found from the measurement,  $\mathcal{E}_S$  is the efficiency found by GEANT

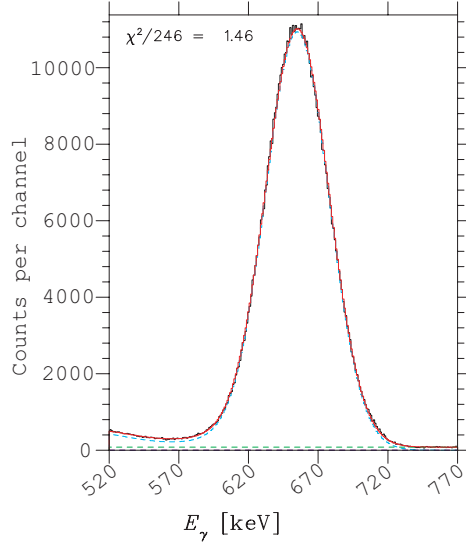
Errors in the measurements are due mostly to the uncertainty of the source activities found in §6.2. These measurements are then used to make a comparison to the efficiency produced by the GEANT simulation described in §6.3.1. Good agreement was found between simulation and measurement. The results are shown in Fig. 6.14 and summarized in Table (6.2).

## 6.4 Efficiency of the Full Gamma Ray Detector

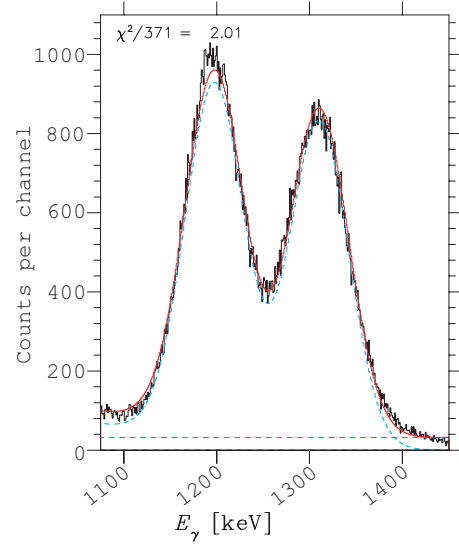
All data discussed involving the full array whether simulated or measured used the coordinate system shown in Fig. 6.15. Positive  $z$  coordinates are downstream of (away from) the DRAGON gas target. The detectors with positive  $x$  values comprise the west array. Detectors with negative  $x$  are the east array. Detectors with  $x = 0$  are the “crowning” detectors labelled 1-10 in Fig. 6.15. Beam height is at  $y = 0$ , with negative  $y$  values being closer to the floor.

### 6.4.1 Full Array Simulation

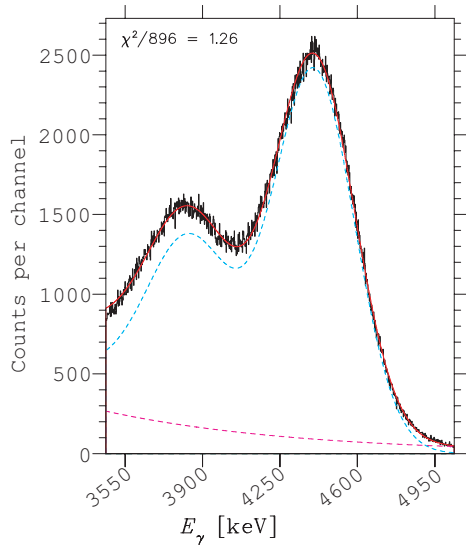
Point sources of 511 keV, 4.44 MeV and 6.13 MeV (See §5.2.1) were simulated in positions starting at the centre of the target ( $z = x = 0$ ) and at beam height in the  $y$  direction. A different simulation was run for point sources at  $z=0,1,3,5,7..21$  cm and  $z=-1,-3,-5,-7,..-21$  cm for each of the three energies. For each of the 30 detectors a histogram of pulse height versus deposited energy was produced using the CERN library histogramming package, HBOOK. A pulse height spectrum was collected for



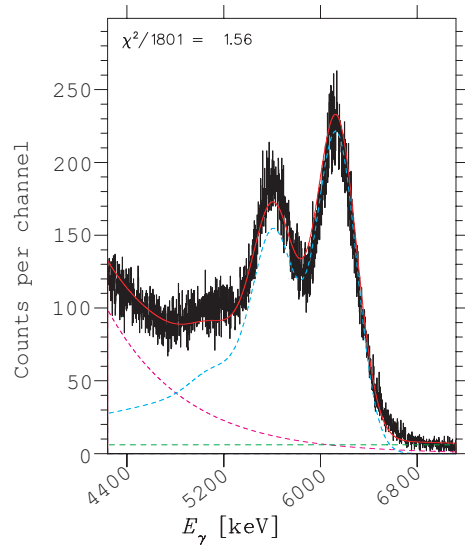
(a) Fit  $^{137}\text{Cs}$  10 cm from a single BGO detector



(b) Fit  $^{60}\text{Co}$  10 cm from a single BGO detector



(c) Fit  $^{241}\text{Am}^9\text{Be}$  10 cm from a single BGO detector



(d) Fit  $^{244}\text{Cm}^{13}\text{C}$  20 cm from a single BGO detector

Figure 6.13: Fitting results for efficiency comparisons of a single BGO detector



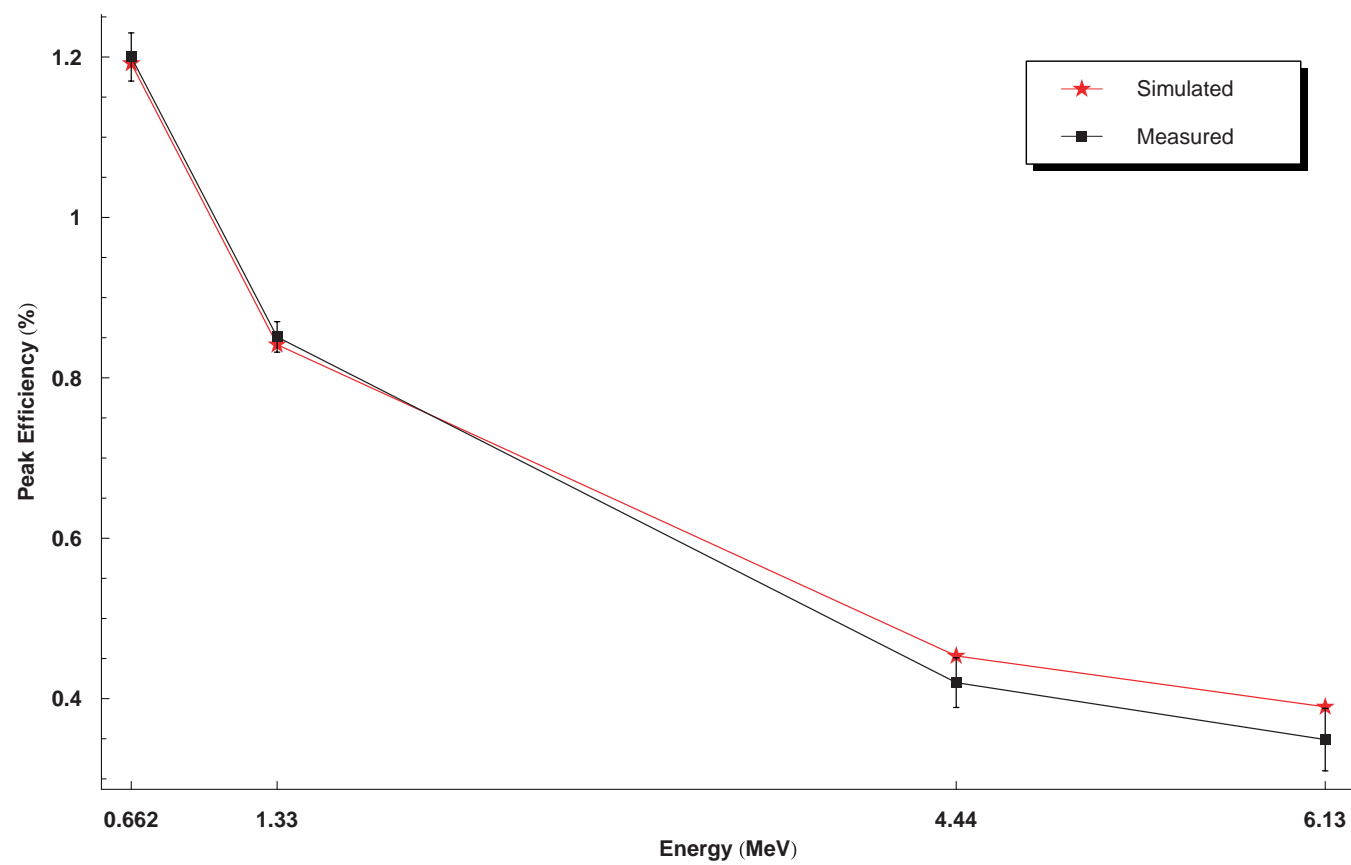


Figure 6.14: Single BGO efficiency measurement comparison between data and simulation

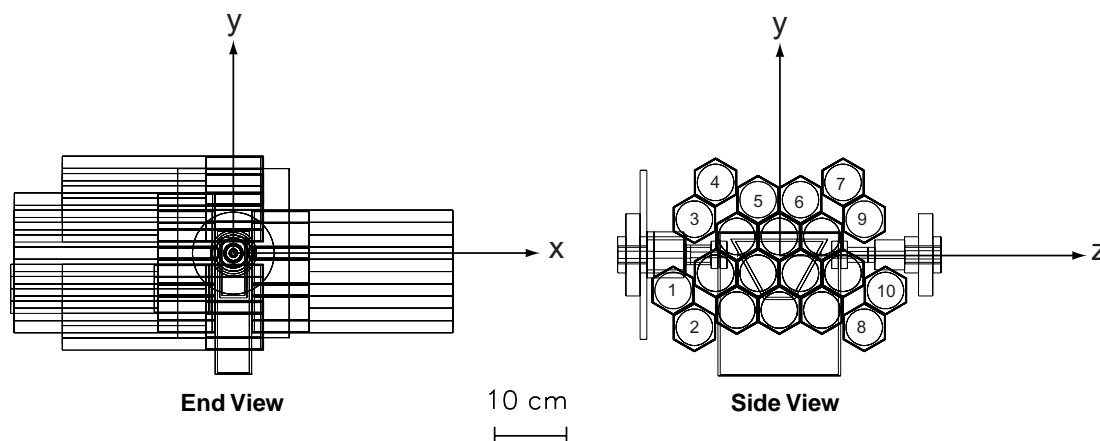


Figure 6.15: Coordinate system used for all measurements of the full array

each of the 30 detectors. Spectra similar to those simulated for an isolated BGO detector were obtained (e.g. using a low energy source Fig. 6.12(a) and a high energy source Fig. 6.12(b)). Fig. 6.12(b) shows the full energy photo peak, first escape peak and barely resolvable is the second escape peak. Also noticeable in the spectra is the lack of resolution effects. These effects were purposely left out to remove the unnecessary complication of having to fit the simulated peaks with Gaussian functions.

In total 1800 spectra were analyzed ( $3 \text{ sources} \times 20 \text{ positions} \times 30 \text{ detectors}$ ). The necessary photopeak count was extracted from the single channel photopeaks using PAW. This number was then divided by the total number of gammas emitted in the simulation (which was 100000 in each case), to find the photopeak efficiency for this detector. Fig. 6.16 illustrates the photopeak efficiency as a function of detector number for each of the 3 sources that were simulated. These results are plotted on a graph of photopeak efficiency as a function of position Fig. 6.17. Statistical errors in these calculations are of order the size of the data point (i.e.  $< 1\%$ ).

### 6.4.2 Photopeak Efficiency Measurements with the Full Gamma Ray Array

Once the simulation was confirmed for the simple case of a single detector at high energy, data was taken to confirm the simulation for the more complicated, full array

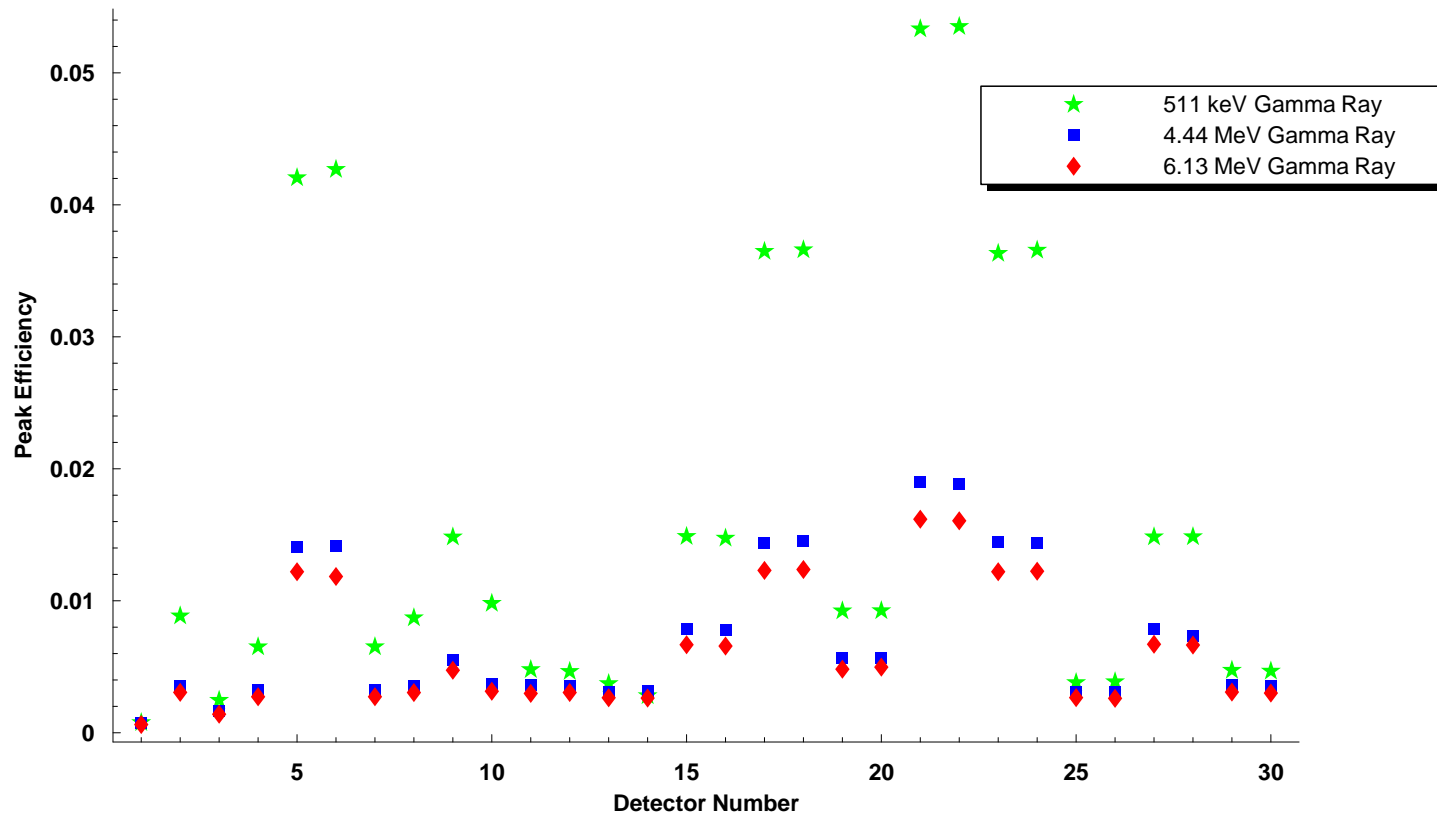


Figure 6.16: Simulated photopeak efficiency for the DRAGON gamma ray as a function of detector number, where  $z = 0$  is the the centre of the gas target

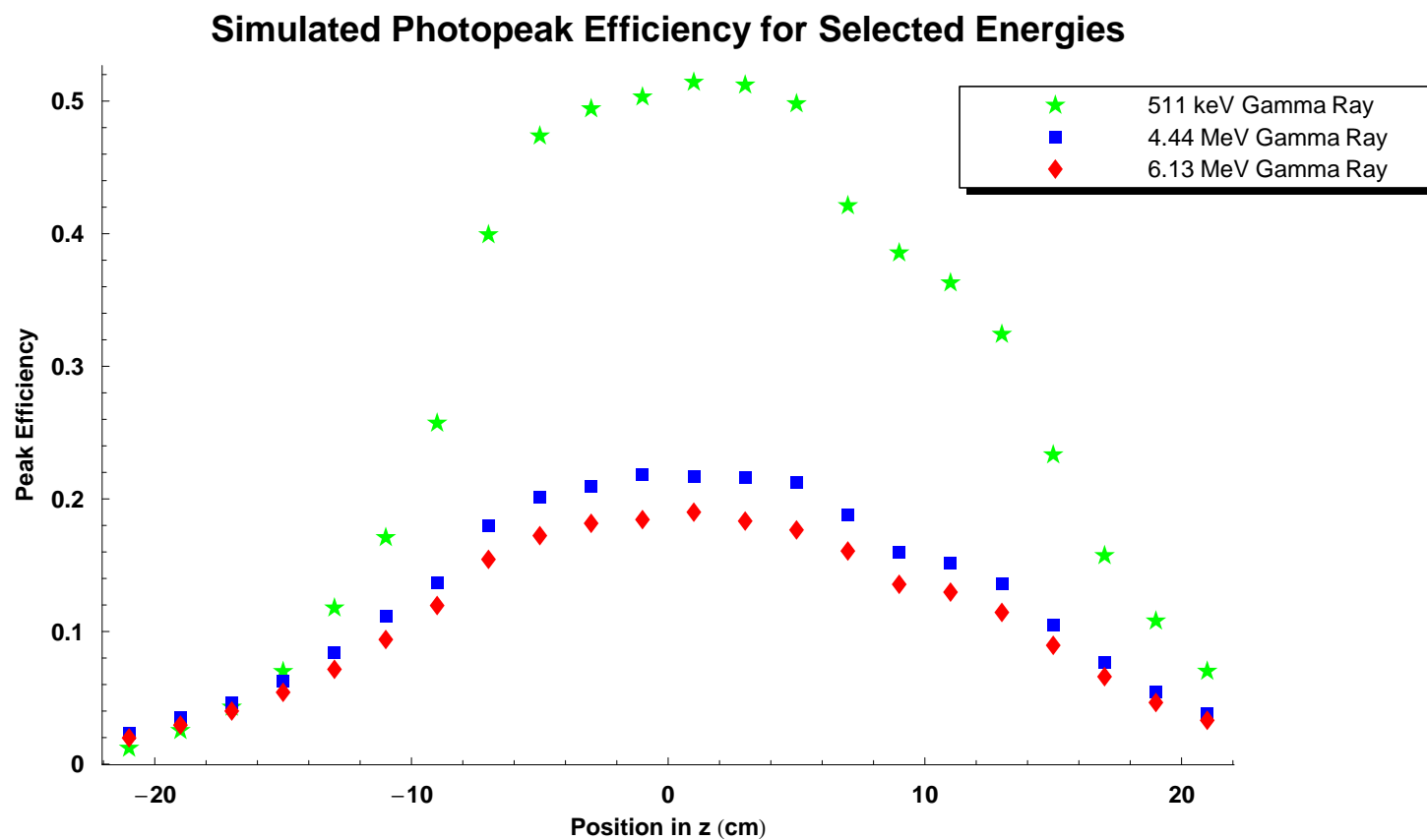


Figure 6.17: Simulated photopeak efficiency for the DRAGON gamma ray as a function of source position, where  $z = 0$  is the centre of the gas target

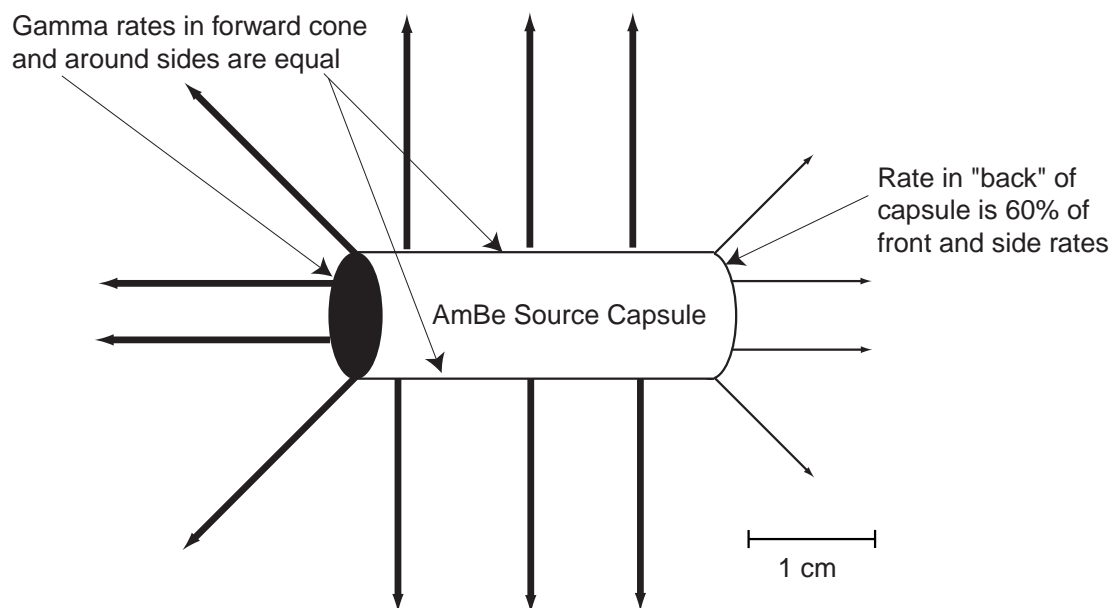


Figure 6.18: Lack of symmetry in gamma emittance in “back” of the capsule due to internal attenuation

geometry. To duplicate actual measurement conditions for the array, a small source was stepped through the DRAGON beam line pipe and into the gas target at beam axis. By this method the source was placed at each  $z$ -position along the beam axis and the array efficiencies were measured and compared to simulation for various  $z$ -positions. Initially, measurements differed from simulation by 35-40%. Subsequent source measurements revealed that the source had non-isotropic gamma ray emission, due to internal attenuation. The gamma emission rate was found to be similar for front and side faces but a reduction in rate of 40% was found between these faces and the “back” face, as defined in Fig. 6.18.

The source rate measurements showed the beam line measurements were flawed because the source was non-isotropic, as compared to the simulated source which was defined to be isotropic. If these sources were to be accurately simulated, measurements would need to be made to determine the angular distribution of the source activity. Due to time constraints these measurements were not done. The compromise was to redo measurements for  $z=0$  only and compare these to simulations. It may be

possible to return to the angular distribution measurements at a later time. The most important efficiency number is the  $z = 0$  measurement because most gamma rays will be emitted from this location during beam experiments [1]. Although it is possible that beam experiments may be sensitive to array response away from  $z = 0$ , due to a resonance not being perfectly centred in the target, simulations indicate that the efficiency response between  $z = -5$  to  $z = 5$  cm deviates from that measured at  $z = 0$  by less than 1% [68]. It is unlikely that a resonance will occur outside the range of the DRAGON inner gas target [8], since there is little target gas to interact. It is intended that these measurements will be extended for completeness at a later date.

The setup for measuring the full array at  $z = 0$  was to position a source in various positions outside the gas target and then to duplicate these conditions in the simulation. Measured and simulated data were then compared and assigned a systematic error to account for any difference between the results. This error would then become part of error estimates of reaction rates measured by future DRAGON experiments (See §4.1).

Analysis of the full array data used “leading gamma” analysis both in the simulation and in the measurements. As a gamma ray interacts with the BGO scintillation material it may deposit its energy in more than one detector through one of the three interaction processes. In leading gamma analysis, the detector which is credited as detecting the gamma event, is that detector which saw the most energy. That is to say if, for example, a 7 MeV gamma ray enters a crystal and deposits 5 MeV in one crystal, then exits that crystal and subsequently deposits its remaining 2 MeV in one of the other crystals, only the detector which detected the most energy, 5 MeV in this case, would be histogrammed. For another event it might be the case that energy was shared in four detectors, in the following steps, 2 MeV, 4 MeV, 0.5 MeV, 0.5 MeV. At the end of this event’s detection, the detector histogrammed would be the second detector of the four as it saw the most energy. This analysis is different from a summing analysis where after the event one would track the gamma ray through all the detectors which it deposited energy and sum all these interactions back into the leading gamma detector. Simulations indicate that for a monoenergetic gamma in energy range between 1-10 MeV, an average of 60% of the gammas deposit their full

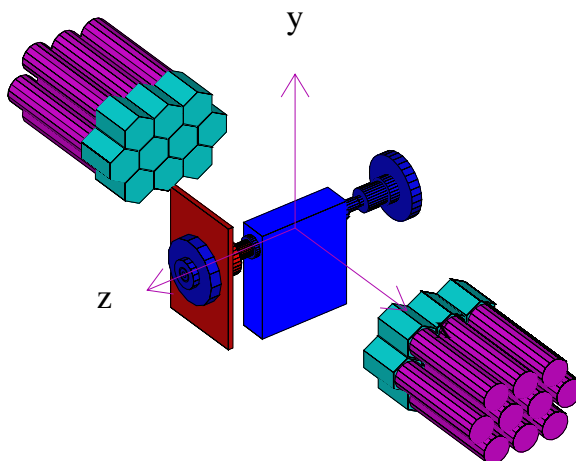


Figure 6.19: Removing the 10 crowning detectors yields an array symmetric in all three directions

energy in a single detector. So long as both data and simulation are analyzed by the same method the comparisons are valid. Leading gamma analysis was used because it produced more reliable energy spectra by rejecting 511 keV pile-up detections which are usually smaller than the main gamma's pulse-height.

### 6.4.3 $^{241}\text{Am}^9\text{Be}$ and $^{244}\text{Cm}^{13}\text{C}$ Measurement: Elevated Source

Source measurements were done in order of increasing complexity. By pulling the array back a distance of  $\approx 31.5$  cm, initial high dead time (50%) due to high source activity was reduced to a value easily tolerable by the electronics (5-10%) [8]. The geometry was made still simpler by removing the crowning detectors from the east mount so that the array became symmetrical in  $x$ ,  $y$  and  $z$  (See Fig. 6.19). Finally, for the “elevated source” runs the source was positioned 15 cm above the gas target (See Fig. 6.20). At this distance the source was more point-like and better approximated the isotropic point source used in the simulation, which improved agreement.

Before data was taken in this simpler geometry, a GEANT simulation test was

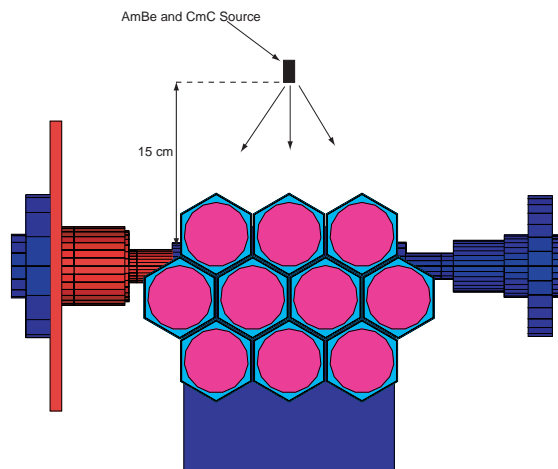


Figure 6.20:  $^{241}\text{Am}^9\text{Be}$  and  $^{244}\text{Cm}^{13}\text{C}$  sources were suspended 15 cm above the gas target

performed to show that indeed GEANT produced the anticipated result of equal efficiency for the east and west arrays (See Fig. 6.21).

The BGO detectors were gain-matched according to the procedure outlined in Appendix C.1 before any data involving the full array was taken. Analysis of the source data runs were done in a similar fashion to the analysis of the single BGO measurement in §6.3.2. A reduction in efficiency of the middle layer of detectors compared to the layer above is expected because the upper level provides shielding to the lower level. A sample fit of 1 out of the 20 detectors, for the  $^{241}\text{Am}^9\text{Be}$  source is shown in figure Fig. 6.22. This fit was representative of all the fits for the other 19 detectors. The results of the elevated source runs, Fig. 6.23 and Fig. 6.24, showed good agreement between data and simulation for all detectors and for both  $^{241}\text{Am}^9\text{Be}$  and  $^{244}\text{Cm}^{13}\text{C}$  sources.



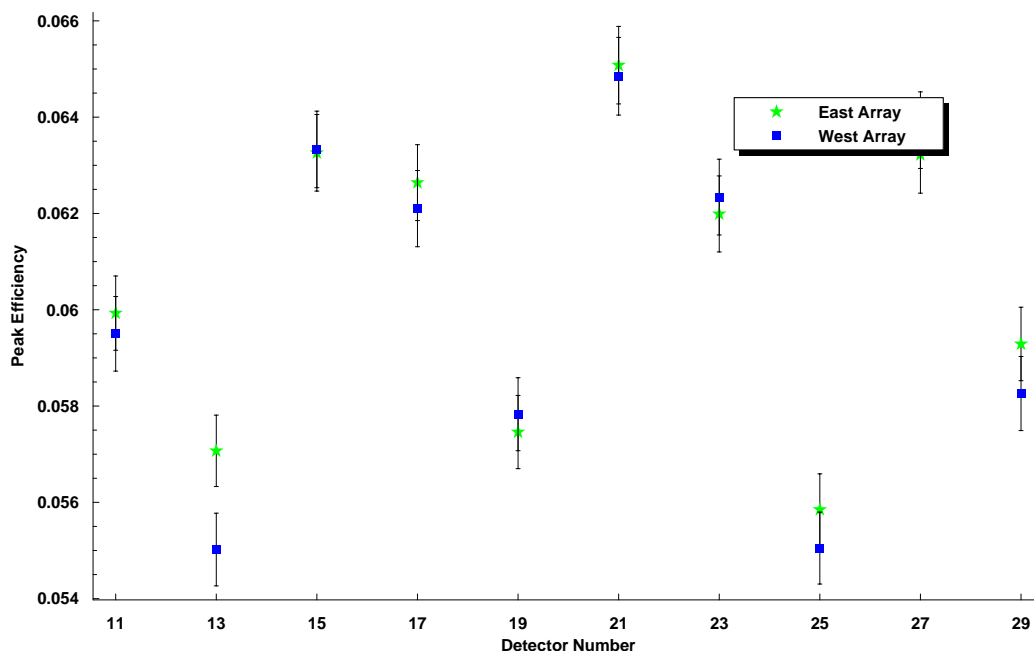


Figure 6.21: Simulated photopeak efficiency, of east and west halves of the array

#### 6.4.4 $^{137}\text{Cs}$ Source Low Energy Measurement

A measurement using a low energy gamma source was used to test the simulation's attenuators. Low energy gammas are attenuated much more than those coming from the high energy gamma sources, so any discrepancies between simulation and data for the attenuators should be amplified at low energy.

It was necessary to carry out two measurements for this source. This was needed to ensure that the incoming gamma rate on each side of the array was consistent. The source was always positioned so that its front face was in the direction of the array half being counted. The results of the low energy measurements, shown in Fig. 6.25, show good agreement.

#### 6.4.5 $^{241}\text{Am}^9\text{Be}$ Source Measurements with all 30 Detectors

The  $^{241}\text{Am}^9\text{Be}$  source was positioned on top of the gas target box facing each array half as in Fig. 6.26. The array halves were pulled back to reduce dead time. Data was

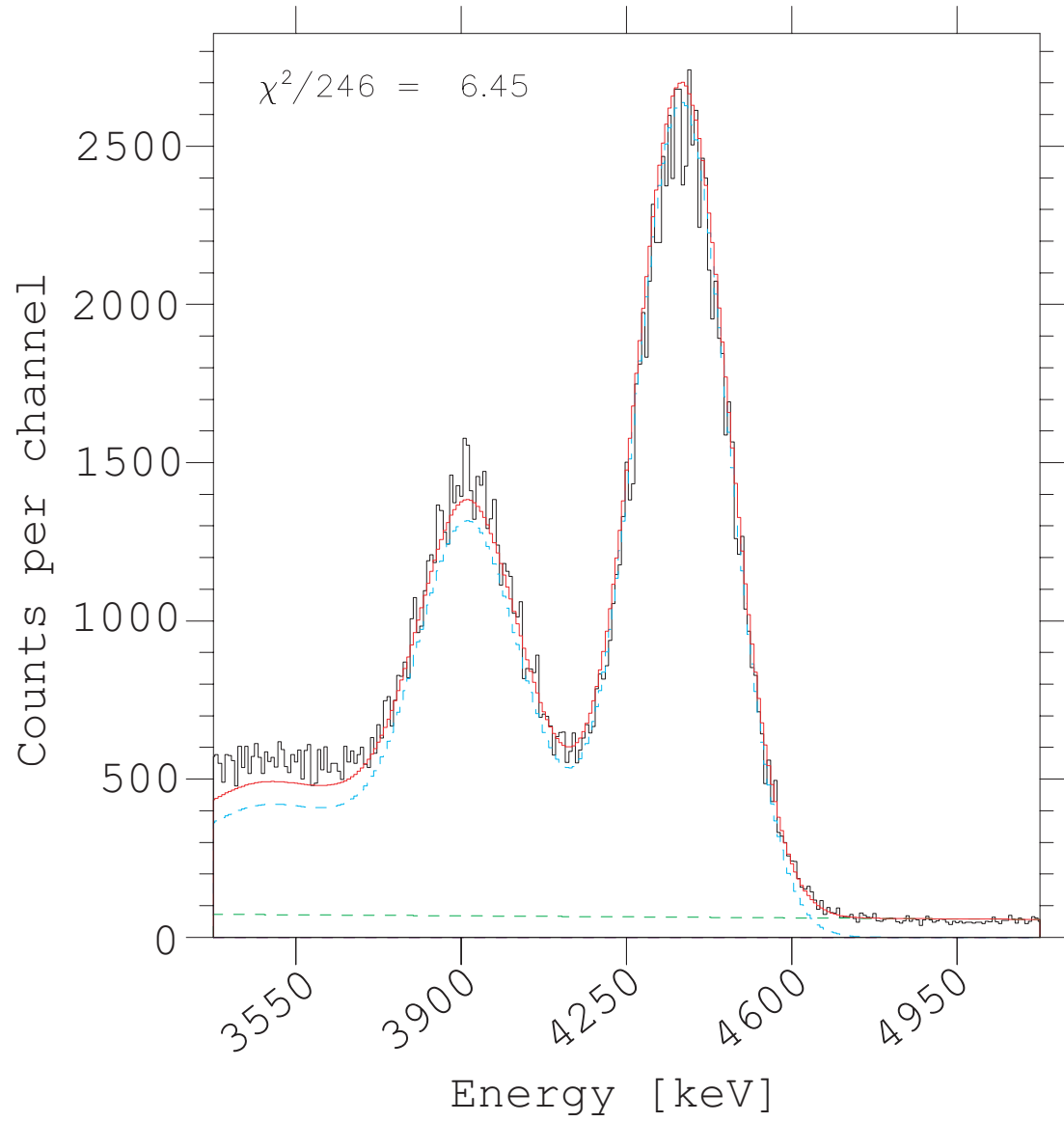


Figure 6.22: A sample Monte Carlo fitting result for the  $^{241}\text{Am}^9\text{Be}$  source.

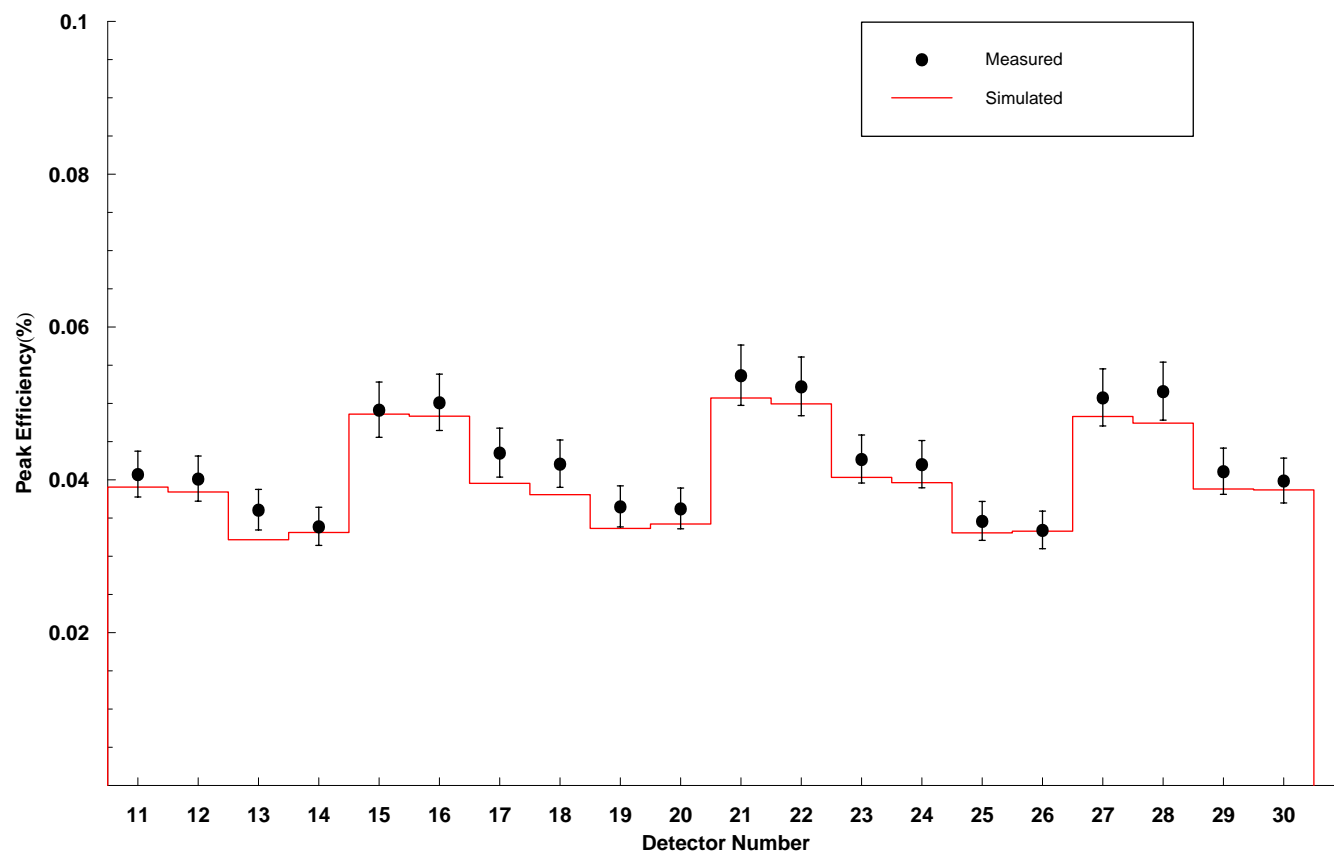


Figure 6.23: Detector by detector efficiency results for the  $^{241}\text{Am}^9\text{Be}$  source suspended 15 cm above the target. Each array half was pulled back by  $\approx 31.5$  cm from the face of the target. Each array half was exposed simultaneously to the source.

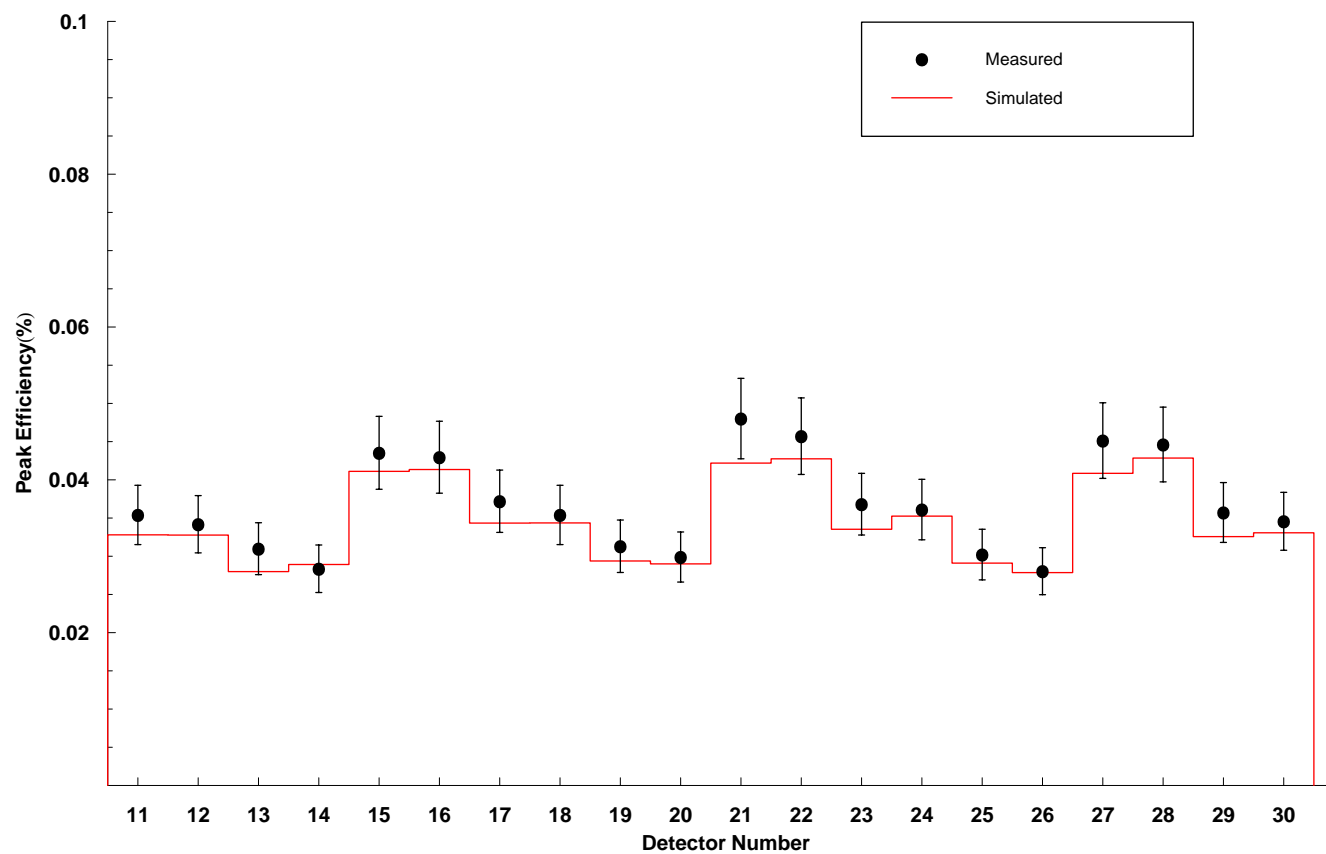
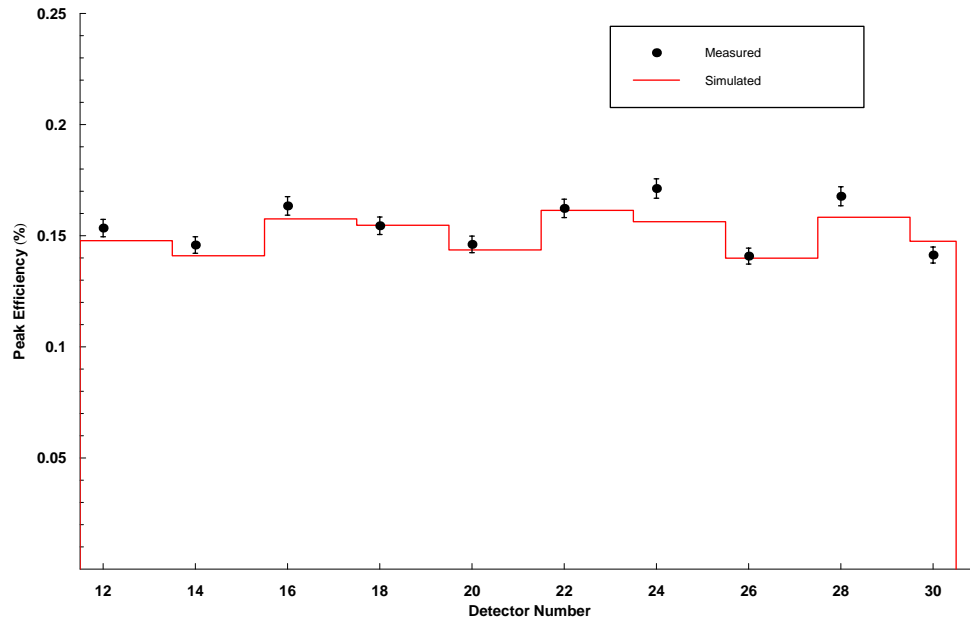
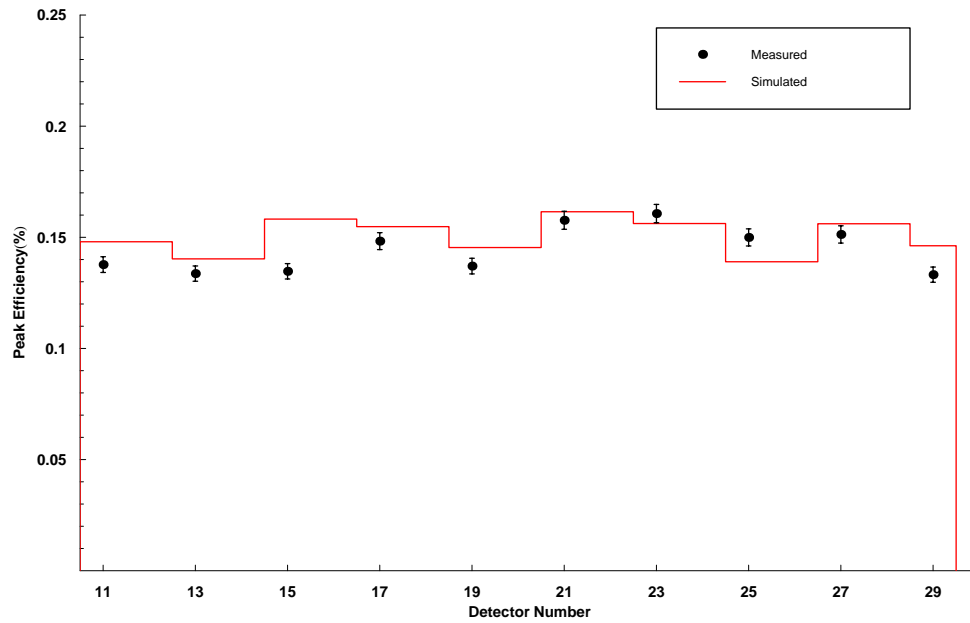


Figure 6.24: Detector by detector efficiency results for the  $^{244}\text{Cm}^{13}\text{C}$  source suspended 15 cm above the target. Each array half was pulled back by  $\approx 31.5$  cm from the face of the target. Each array half was exposed simultaneously to the source.



(a) Efficiency comparison between simulation and data for east detectors



(b) Efficiency comparison between simulation and data for west detectors

Figure 6.25: Detector by detector efficiency results for the  $^{137}\text{Cs}$  source facing each array half. Each array half was pulled back by  $\approx 31.5$  cm from the face of the target.

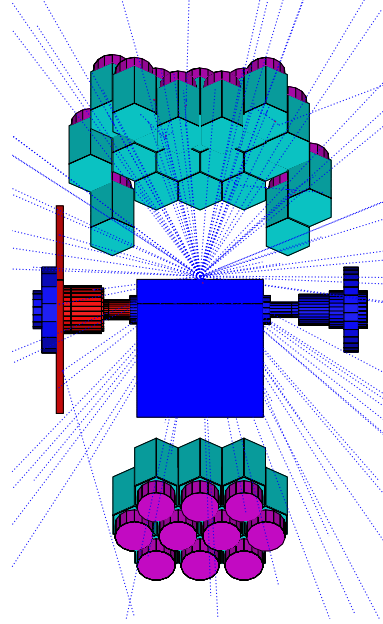
collected for 1% statistics in each detector, and the results were analyzed as described in §6.3.2. These measurements were then compared to the efficiency given by the GEANT simulation for this same setup. The results are plotted in Fig. 6.27. The measurements using the  $^{241}\text{Am}^9\text{Be}$  source showed a slight increase in simulated values over data for the east side. This discrepancy must be due to the presence of the crown detectors on the east but exactly why is not known.

#### 6.4.6 $^{244}\text{Cm}^{13}\text{C}$ Measurement: Source at Beam Position

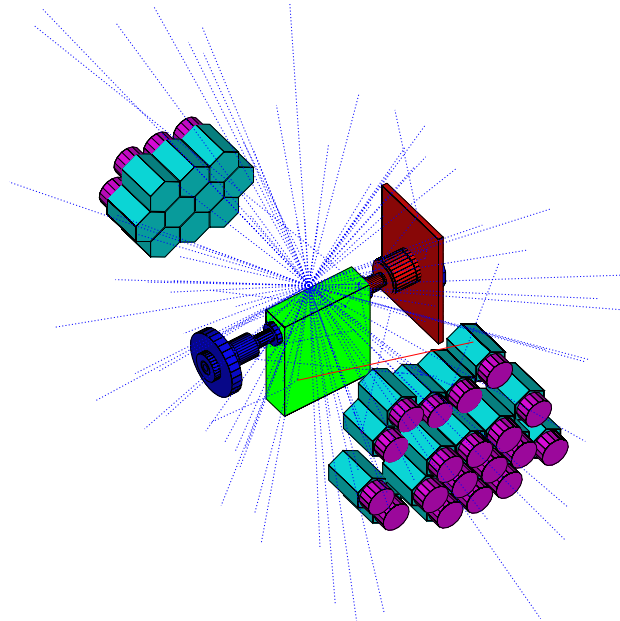
As a final test, the  $^{244}\text{Cm}^{13}\text{C}$  source was placed inside the gas cell and two more measurements were taken. The crown detectors of the array were in place and all detectors were moved to their normal operating positions close against the gas target. The source was positioned so that it was in the middle of the gas cell at beam height, (See Fig. 6.28). One measurement was taken with the source facing east and one west. The intention was to also perform the same test with the  $^{241}\text{Am}^9\text{Be}$  source but due to its size it did not fit in the same geometry as the  $^{244}\text{Cm}^{13}\text{C}$  source. Analysis was performed as in the previous measurements. A sample fit of 1 out of the 30 detectors, for the  $^{244}\text{Cm}^{13}\text{C}$  source is shown in figure Fig. 6.29. This fit was representative of all the fits for the other 29 detectors. Fig. 6.30 gives the comparison between data and simulation for this source and array geometry.

### 6.5 Summary of Error Analysis

The errors associated with the final efficiency numbers presented in this thesis are a combination of errors related to the measurements and errors related to the simulation. For both the measurement and the simulation statistical and systematic errors exist. In the measurement, statistical errors were kept to a minimum by collecting enough data so that this value was  $<1\%$ , and therefore was not significant in the final calculation of the errors. Similarly, in the simulation, enough events were triggered so that statistics were always better than 1%.

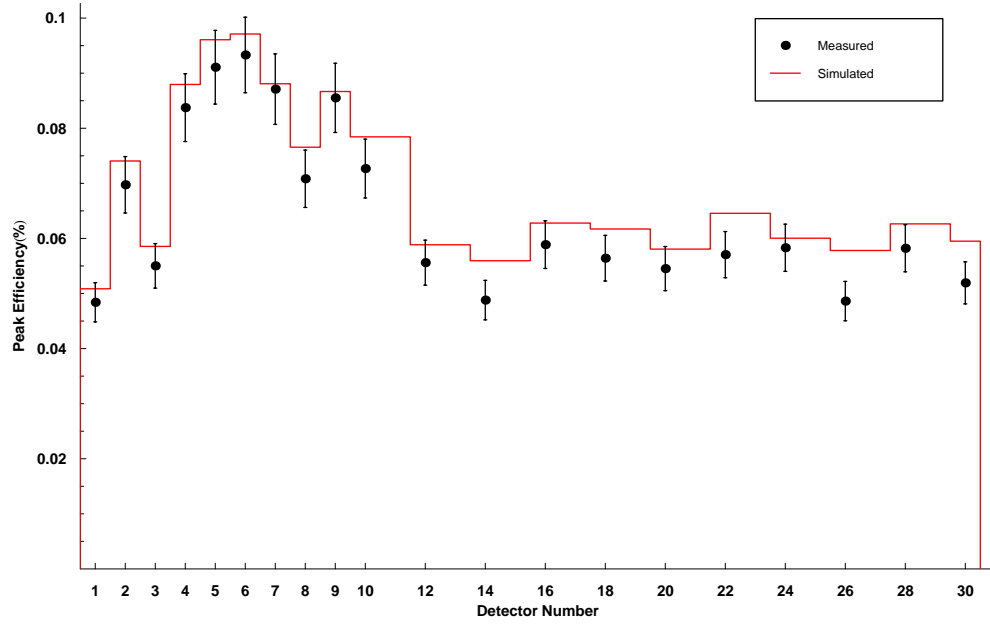


(a)  $^{241}\text{Am}^9\text{Be}$  source facing east detectors

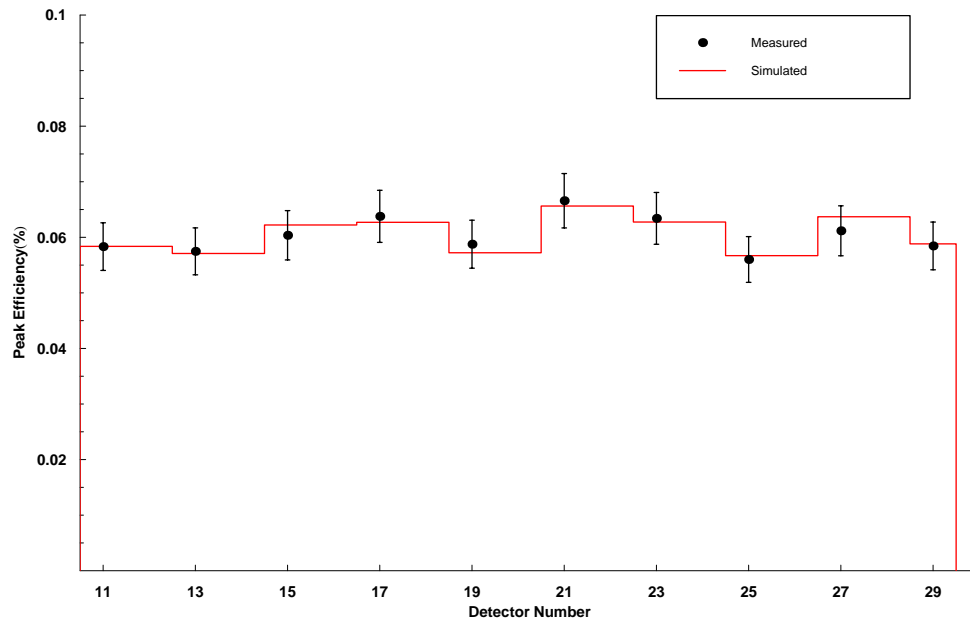


(b)  $^{241}\text{Am}^9\text{Be}$  source facing west detectors

Figure 6.26: Two measurements with the  $^{241}\text{Am}^9\text{Be}$  source were necessary. Array detectors have been pulled back by  $\approx 31.5$  cm to reduce dead time



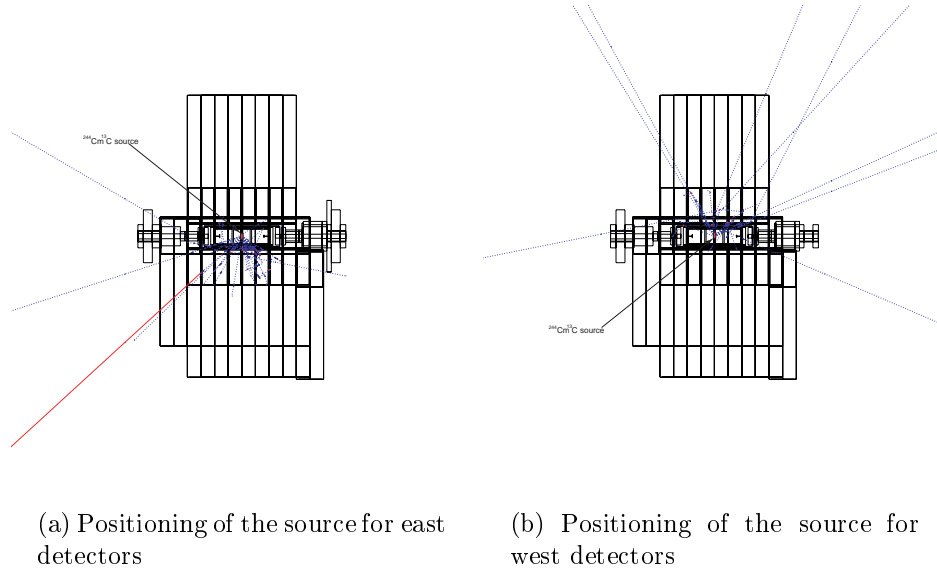
(a) Efficiency comparison between simulation and data for east detectors



(b) Efficiency comparison between simulation and data for west detectors

Figure 6.27: Detector by detector efficiency results for the  $^{241}\text{Am}^9\text{Be}$  facing each array half. Each array half is pulled back by  $\approx 31.5$  cm from the face of the target.





(c) Photo of the gas target showing the  $^{244}\text{Cm}^{13}\text{C}$  source positioned inside

Figure 6.28: The  $^{244}\text{Cm}^{13}\text{C}$  source was placed inside the gas target and two measurements were taken with the active face of the source facing the east and west sides of the array

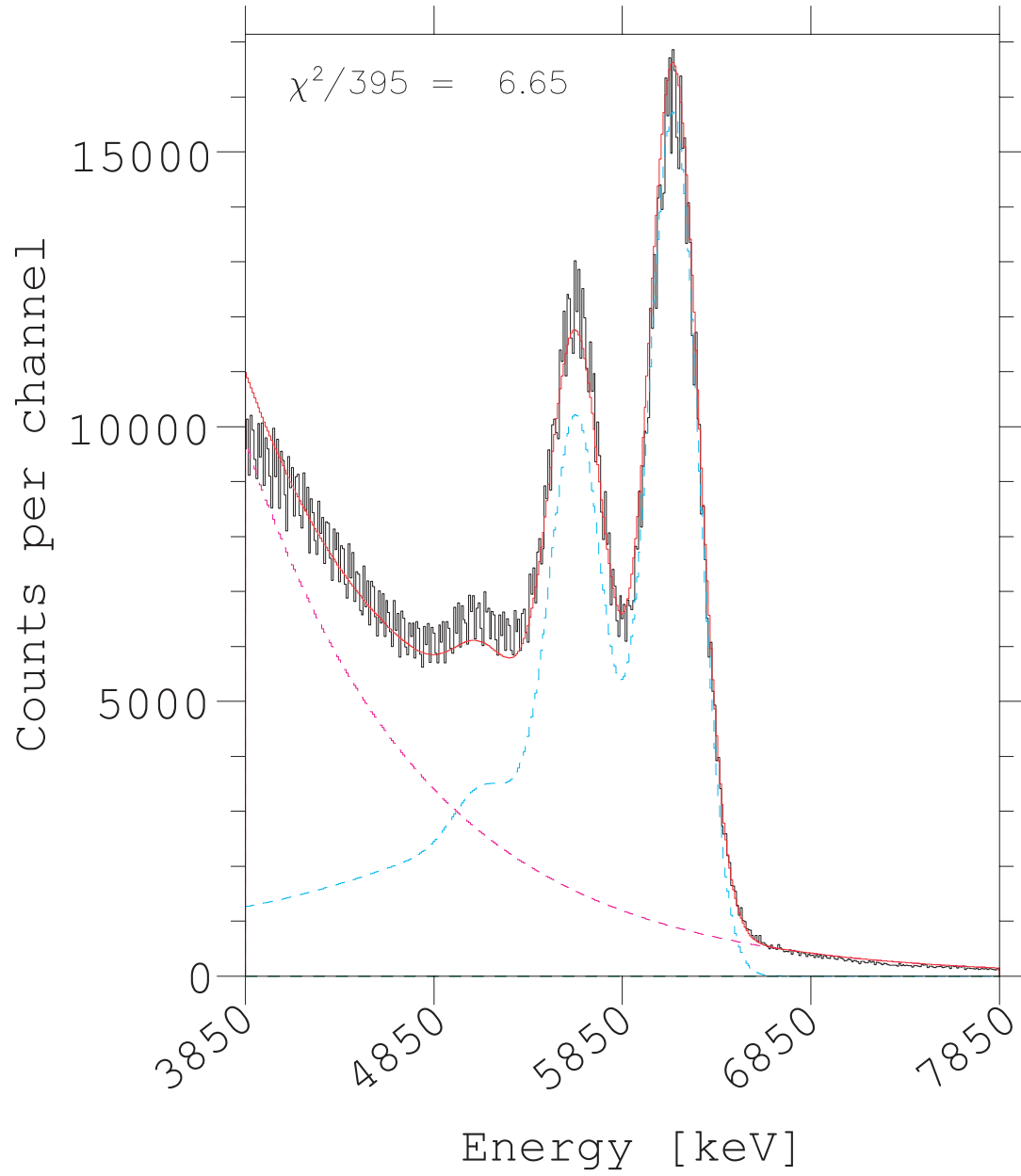
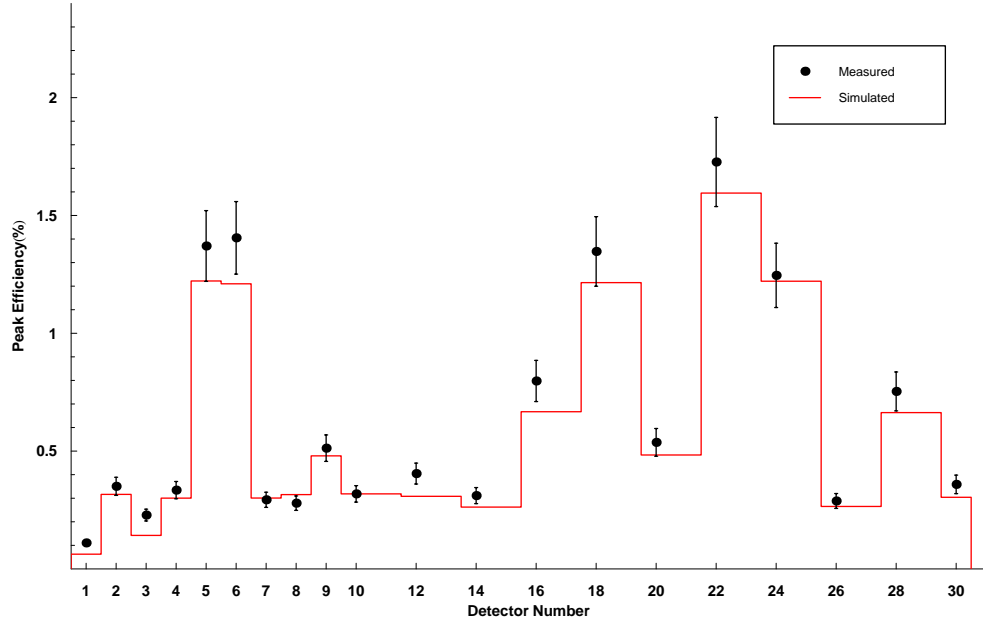
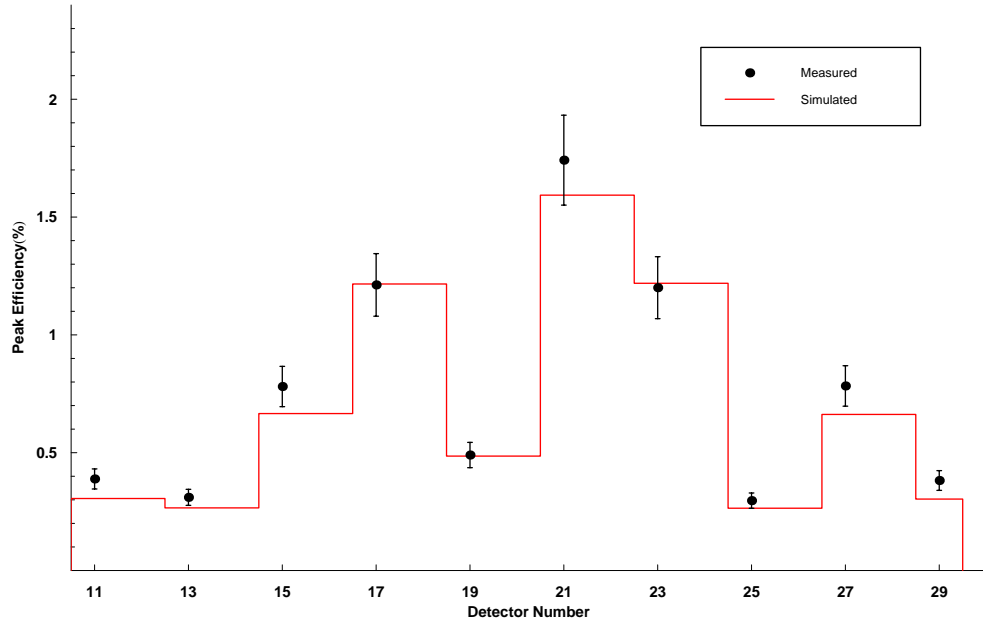


Figure 6.29: A sample Monte Carlo fitting result for  $^{244}\text{Cm}^{13}\text{C}$  source inside the gas target at  $z = 0$



(a) Efficiency comparison between simulation and data for east detectors



(b) Efficiency comparison between simulation and data for west detectors

Figure 6.30: Detector by detector efficiency results for the  $^{244}\text{Cm}^{13}\text{C}$  source positioned inside the gas target box at  $z = 0$ , and at beam height. Each array half is in its normal operating position against the gas target box.

### 6.5.1 Source Activity Error Analysis

Source strength measurements using the NaI crystal included small contributions from: the errors associated with the published values of the total efficiency of NaI crystals, measurement of distances and dead time, and inaccuracies that came from fitting. A much more significant limitation to the error analysis was due to the range of published values for the ratio between peak counts to total counts in a NaI crystal at various energies.

The source/detector holder was carefully constructed to reduce any errors coming from measuring the distance between detector face and source. Every attempt was made to limit the uncertainty in this distance to  $<1$  mm, which made the contribution to the total error by distance measurement inaccuracies insignificant.

Each source measurement also included a correction for two related quantities, the system dead time and detector pile-up. The Nucleus data acquisition system used in the single detector measurements recorded two times. The first time was the real computer clock time which is accumulated during a measurement and the second was the time during which the Wilkinson ADC was able to accept data. The ratio of these two times gives a measure of the system live time/dead time. The dead times ranged from 7% for the  $^{137}\text{Cs}$  source to 1% for the  $^{244}\text{Cm}^{13}\text{C}$  source. The dead time was accurately known so it was used to make a correction to the source activity measurement rather than factoring into the error. The only significant pile-up was observed in the  $^{137}\text{Cs}$  source and a correction to the total counts was made by adding a fraction of those counts to the right of the full energy peak by the method explained in §6.2.2. Any pile-up events occurring to the left of the peak cannot be accounted for but these do not contribute to the activity because only the full energy events were used in the calculation.

The analysis of the peak data was done using a Monte Carlo fitting technique described previously in §6.2.1. Each data spectrum was fit using a Monte Carlo spectrum that was gain matched to the data to avoid any binning problems. The limits for the fit were kept consistent by taking the range from the relatively flat Compton scattering region to the left of the full energy peak and escape peaks, to

a flat region to the right of the peak for each source's data. Moving the bounds of the fit by 50 keV anywhere along these flat regions made no significant change to the integrated peak counts. The chi-squared for the  $^{137}\text{Cs}$  data was 1.89, the  $^{60}\text{Co}$  was 2.05, the  $^{241}\text{Am}^9\text{Be}$  was 1.35 and the  $^{244}\text{Cm}^{13}\text{C}$  was 1.26. The quality of the fits determined that errors associated with fitting were an insignificant contribution to the final source activity error, compared to other sources.

To get the total source activity from a measure of the peak counts from each source's data the total efficiency of a NaI crystal for a specific geometry and the peak-to-total ratios are required. Data on the 3"  $\times$  3" NaI crystal used in the measurement is well published as outlined in §6.2.2. The total efficiencies, in the energy range of interest (i.e. 0.662-6.13 MeV), quoted by several authors are in agreement within few percent so the value of the total efficiency does not contribute significantly to the total source activity error. There is however, a range of values for the peak-to-total ratios published by several authors in this same energy range. Most of these published ratios are calculated and measured below 3.5 MeV but only calculated values can be accurately extracted from the literature above 3.5 MeV. In the region below 3.5 MeV the published values vary by as little as 1% for the  $^{137}\text{Cs}$  energy of 0.662, but by as much as 9% for the  $^{244}\text{Cm}^{13}\text{C}$  energy of 6.13 MeV. This range was the leading contributor to the uncertainty in the calculation of the source activity, and was reflected in the errors of the final source activities. These factors were combined into the final error  $\Delta N$ . The error in the source activity was then,

$$\Delta N = N \sqrt{(\Delta d)^2 + (\Delta F)^2 + (\Delta \mathcal{E}_t)^2 + (\Delta \mathcal{R})^2 + (\Delta A)^2} \quad (6.3)$$

Where,

$\Delta d$  = contribution due to source to detector distance measurements

$\Delta F$  = contribution due to variations in fitting

$\Delta \mathcal{E}_t$  = contribution due to uncertainty in published total efficiency values

$\Delta \mathcal{R}$  = contribution due to range of published peak-to-total values

$\Delta A$  = contribution due to statistics in the area under the full energy peak

As described previously,  $\Delta\mathcal{R}$  is the dominant factor , so then Equation (6.3) reduced to,

$$\Delta N \approx N\Delta\mathcal{R} \quad (6.4)$$

$\Delta N$  ranged between 2% for  $^{137}\text{Cs}$  , to 10% for  $^{244}\text{Cm}^{13}\text{C}$  .

### 6.5.2 Single BGO Error Analysis

The efficiency of a single BGO detector was calculated by dividing the number of gamma rays counted in the detector by the number of gamma rays released by the source. The number of gamma rays counted had errors which were similar to those of the NaI measurements because the experimental setup and data analysis were identical to the NaI crystal. Dead time corrections, pile-up, fitting errors and distance measurements were included in the uncertainty but were found to be insignificant contributors to the final error in the efficiency calculation. The only significant contribution to the error was the uncertainty in the source activity found during the analysis of the NaI data.

These factors were combined into the final error  $\Delta\mathcal{E}_D$ . The error in the efficiency of a single detector was then,

$$\Delta\mathcal{E}_D = N\sqrt{(\Delta d)^2 + (\Delta F)^2 + (\Delta N)^2 + (\Delta A)^2} \quad (6.5)$$

Where,

$\Delta d$  = contribution due to source to detector distance measurements

$\Delta F$  = contribution due to variations in fitting

$\Delta A$  = contribution due to statistics in the area under the full energy peak

$\Delta N$  = contribution due to the uncertainty in the source activity

As described previously,  $\Delta N$  is the dominant factor , so then Equation (6.5) reduced to,

$$\Delta\mathcal{E}_D \approx \mathcal{E}_D\Delta N \quad (6.6)$$

$\Delta\mathcal{E}_D$  ranged between 2.5% for  $^{137}\text{Cs}$  , to 11% for  $^{244}\text{Cm}^{13}\text{C}$  .

### 6.5.3 Full Array Error Analysis

The experimental setup for the efficiency measurements involving the full array are described in §3.2 and §3.3. Efficiencies were calculated by combining the analysis of single detectors in the array. The analysis of the single detectors was done in a method identical to that used for a single BGO efficiency measurement, so the associated uncertainties were also similar. Fitting errors and distance measurements were included in the uncertainty but were found to be insignificant contributors to the final error in the efficiency calculation.

Dead time corrections were made using the dual scalar technique explained in §3.4. Dead times ranged between 4% and 46%. The higher dead times occurred in measurements involving the  $^{137}\text{Cs}$  source. The two measurements involving the  $^{241}\text{Am}^9\text{Be}$  source gave dead times of 5% for the measurement where the source was positioned 15 cm above the box and 11% for the measurement where the detectors were pulled back. The measurement involving the the  $^{244}\text{Cm}^{13}\text{C}$  source inside the box had a dead time of 14%. The dead times of the  $^{241}\text{Am}^9\text{Be}$  and  $^{244}\text{Cm}^{13}\text{C}$  sources are within the range that was tested for using the method of §3.4, so an accurate correction is possible. Dead times for  $^{137}\text{Cs}$  were on the border of the range tested for, but the small discrepancy between simulated and measured efficiencies for  $^{137}\text{Cs}$  did not reflect any problems associated with this, high dead time, correction. This meant that the larger discrepancy seen between simulated and measured efficiencies for  $^{241}\text{Am}^9\text{Be}$  and  $^{244}\text{Cm}^{13}\text{C}$  were more likely to be due to other factors, rather than the dead time.

The uncertainties described above were combined and using Equation (6.5), the efficiency for a single BGO was found. Then, each single BGO, efficiency error was added in quadrature to the other 29 detectors to get the total error for the entire array. The total error  $\Delta\mathcal{E}_D$  was found by,

$$\Delta\mathcal{E}_D = (\mathcal{E}_{D_1})^2 + (\mathcal{E}_{D_1})^2 + \dots + (\mathcal{E}_{D_{30}})^2 \quad (6.7)$$

$\Delta\mathcal{E}_D$  for the full array, in different source geometries, is given in Table (6.4).

#### 6.5.4 GEANT Simulation Error Analysis

Any uncertainty due geometrical calculations were minimized in the simulation for the following two reasons:

1. Considerable effort was made to accurately determine the  $x,y$  and  $z$  positions of the gamma detectors in array and then transfer them to the simulation.
2. GEANT 3 has been tested in numerous applications that depend on it's ability to accurately determine distances and solid angles. The likelihood that simple, mathematical algorithms in GEANT 3 are wrong are nil.

There were two factors in the simulation that were not tested extensively and therefor were probably the leading contributors to the systematic differences shown between measured and simulated efficiencies.

The first being that the simulated detectors were constructed using a uniform thickness of aluminum casing, and crystal volume. The real detectors may have varied in crystal volume somewhat but it was not possible to measure this. Also, the array consisted of detectors produced by two manufacturers and the thickness of the aluminum casing were different between the two.

The second, probably more significant contributor to the systematic error was the geometry of the source used in the simulation. The simulation used a point source to represent the gamma sources used in the measurement. This representation was an accurate model of the  $^{137}\text{Cs}$  and  $^{60}\text{Co}$  sources but not the  $^{241}\text{Am}^9\text{Be}$  and  $^{244}\text{Cm}^{13}\text{C}$  sources.

All possible errors, either known or unknown, associated with the simulation are lumped into a single error,  $\Delta\Psi_{DS}$ , such that the *discrepancy between between measured and simulated data is taken as the systematic error in the simulation*. The rationale for this is that if all sources of errors are taken into account in the measurement then the simulation must lack some component of the real experimental setup to account for the discrepancy. Values for  $\Delta\Psi_{DS}$  are given in Table (6.4).



## 6.6 Re-fitting the Monte Carlo Data

The analysis of the data in the previous sections yielded a systematic difference between measurement and simulation in the range of <1% to 10%. The data was reanalyzed in an attempt to determine if a pattern existed which may explain some the differences found between the data and the simulation. A normalization factor  $A$  was calculated by fitting the existing Monte Carlo data to the measured data using the standard deviation error in the data points to limit the factor.

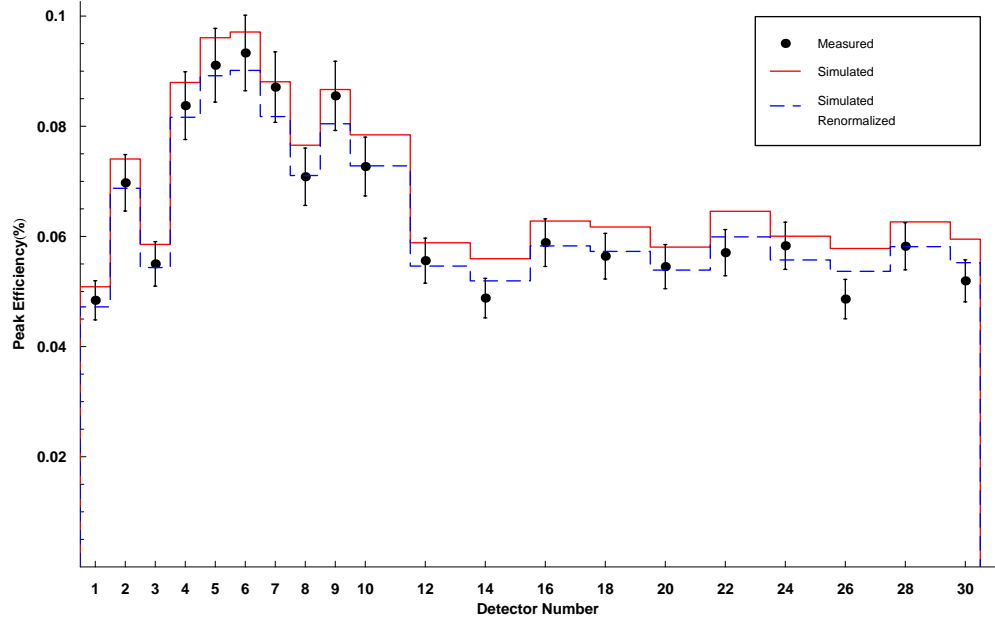
$$y'_i = Ay_i \quad \text{for each data point } i \quad (6.8)$$

Using Equation (6.8), the refit Monte Carlo data points  $y'_i$  were found by multiplying each original data point  $y_i$  by the same value of  $A$ . A final data set of  $y_i$  was determined by: varying  $A$ , fitting the  $y'_i$  to the measured data points using the error in the data points as a constraint for the fit, and minimizing  $\chi^2$ . The result is the overall normalization factor which moves the Monte Carlo data up or down to best fit the measured data. The values of  $A$  resulting from the fitting procedure for the various runs is shown in Table (6.3).

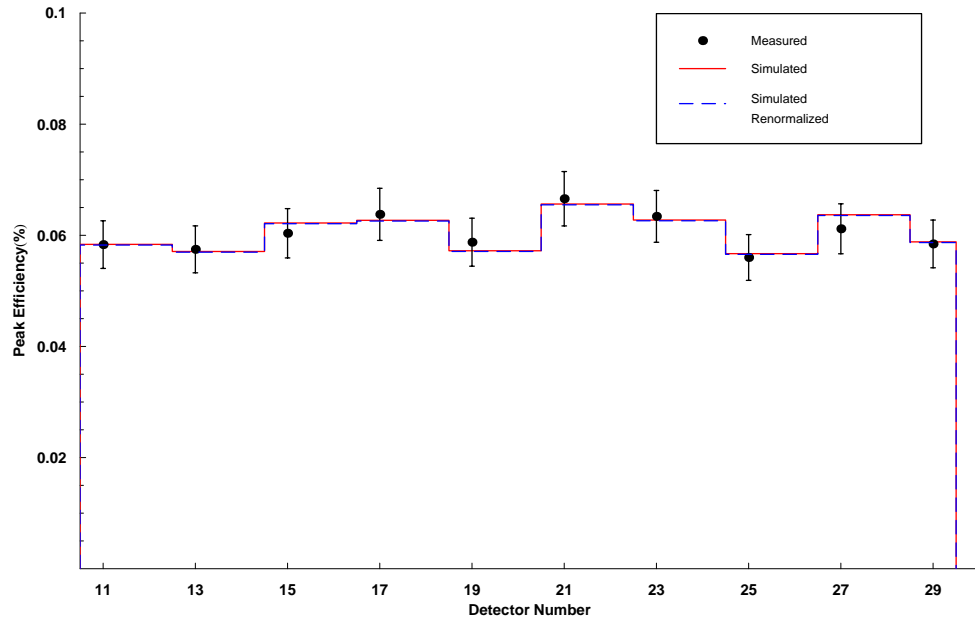
Run #	Source	Source Position	$A$	$\pm\Delta A$
8182	$^{244}\text{Cm}^{13}\text{C}$	inside box, east	1.113	0.028
8188	$^{244}\text{Cm}^{13}\text{C}$	inside box, west	1.108	0.039
8106	$^{241}\text{Am}^9\text{Be}$	on box top, east	0.928	0.015
8112	$^{241}\text{Am}^9\text{Be}$	on box top, west	0.998	0.023
8136	$^{241}\text{Am}^9\text{Be}$	15 cm above box	1.056	0.017
8170	$^{244}\text{Cm}^{13}\text{C}$	15 cm above box	1.056	0.026
8160	$^{137}\text{Cs}$	on box top, east	1.023	0.008
8157	$^{137}\text{Cs}$	on box top, west	0.953	0.008

Table 6.3: The resulting values of  $A$  from refitting the Monte Carlo data to the measured data points

Plots of the renormalized fit against the original simulation data and measured data gives are shown in Figs. 6.31-6.35.



(a) Efficiency comparison between simulation and data for east detectors



(b) Efficiency comparison between simulation and data for west detectors

Figure 6.31: Re-fit detector by detector efficiency results for the  $^{241}\text{Am}^9\text{Be}$  facing each array half. Each array half is pulled back by  $\approx 31.5$  cm from the face of the target. The red line is the original simulation data and the dashed blue line is the renormalized simulation data.

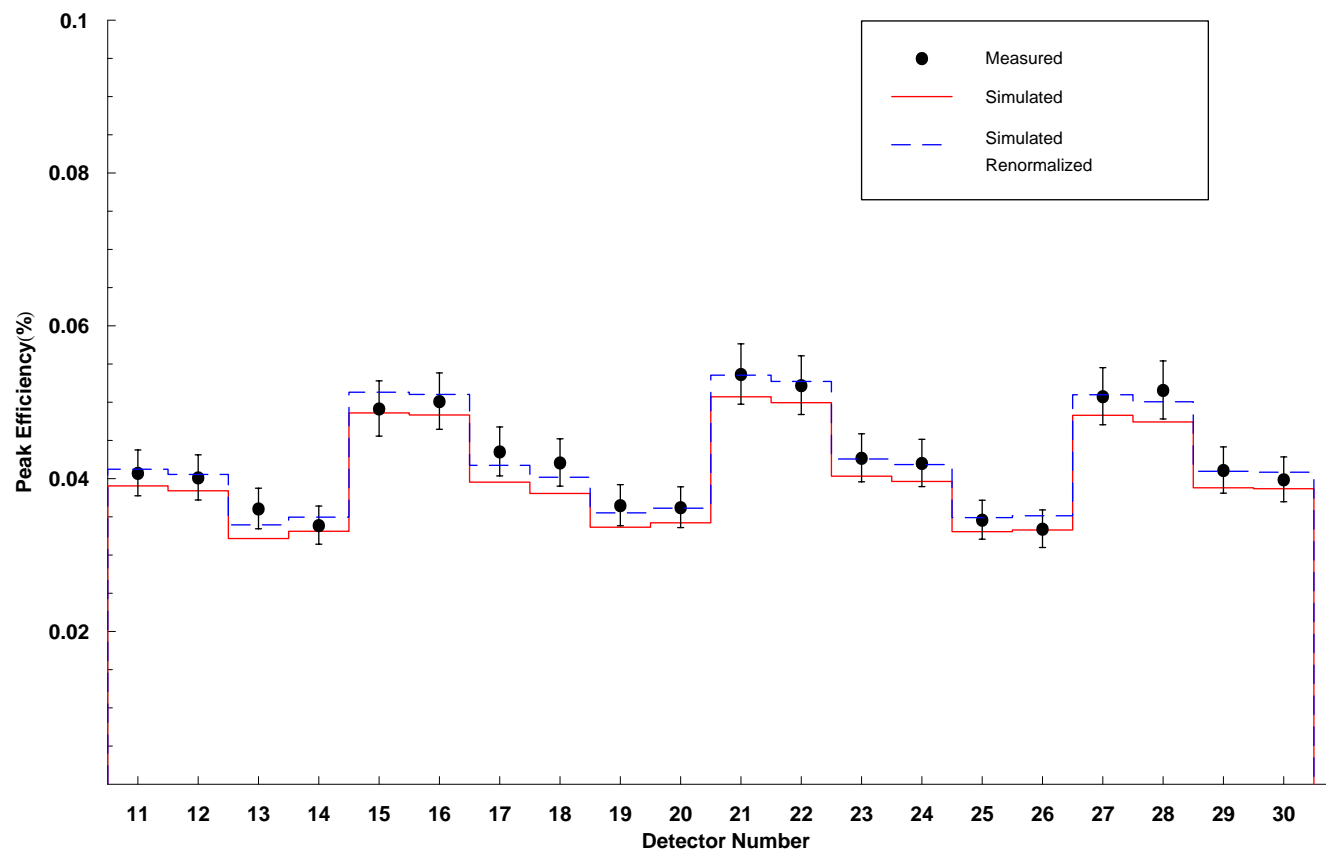


Figure 6.32: Re-fit detector by detector efficiency results for the  $^{241}\text{Am}^9\text{Be}$  source suspended 15 cm above the target. Each array half is exposed simultaneously to the source. The ten crowning detectors have been removed. The red line is the original simulation data and the dashed blue line is the renormalized simulation data.

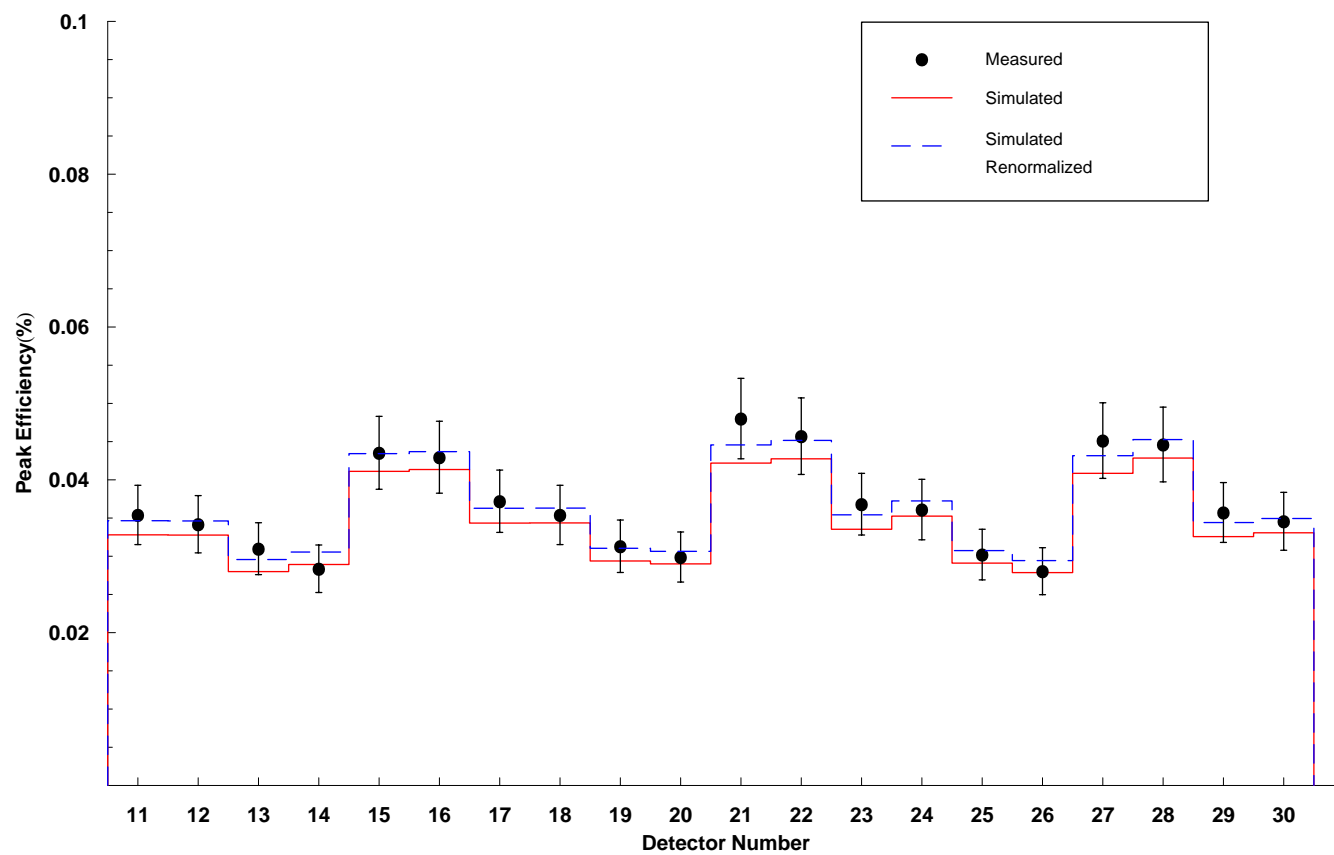
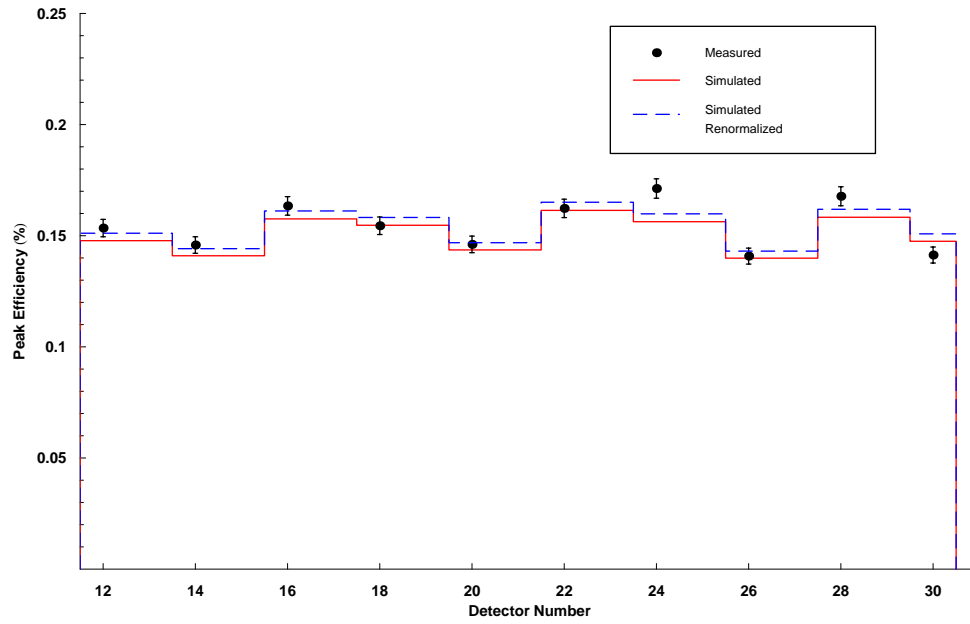
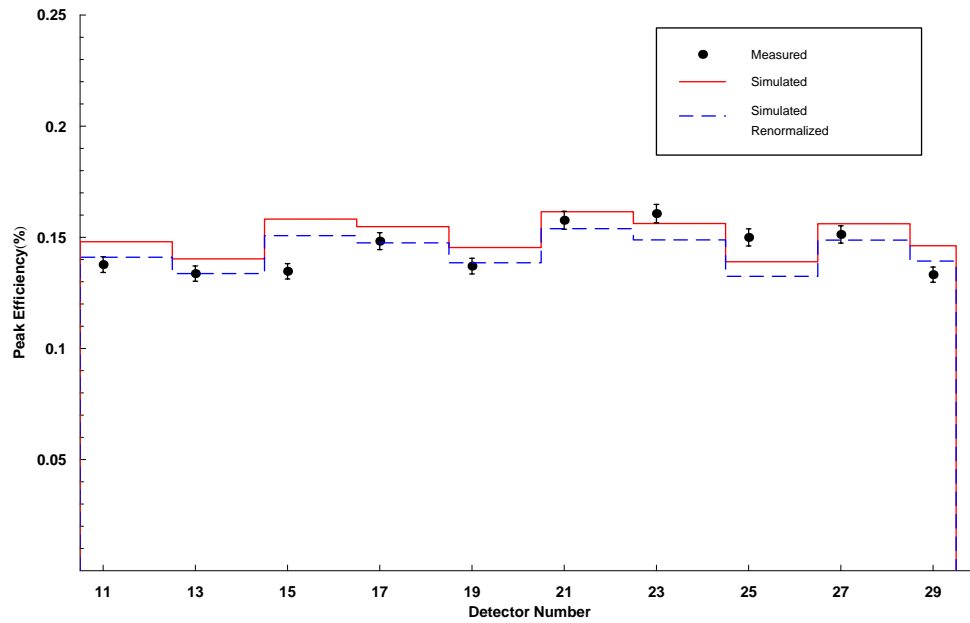


Figure 6.33: Re-fit detector by detector efficiency results for the  $^{244}\text{Cm}^{13}\text{C}$  source suspended 15 cm above the target. The red line is the original simulation data and the dashed blue line is the renormalized simulation data.

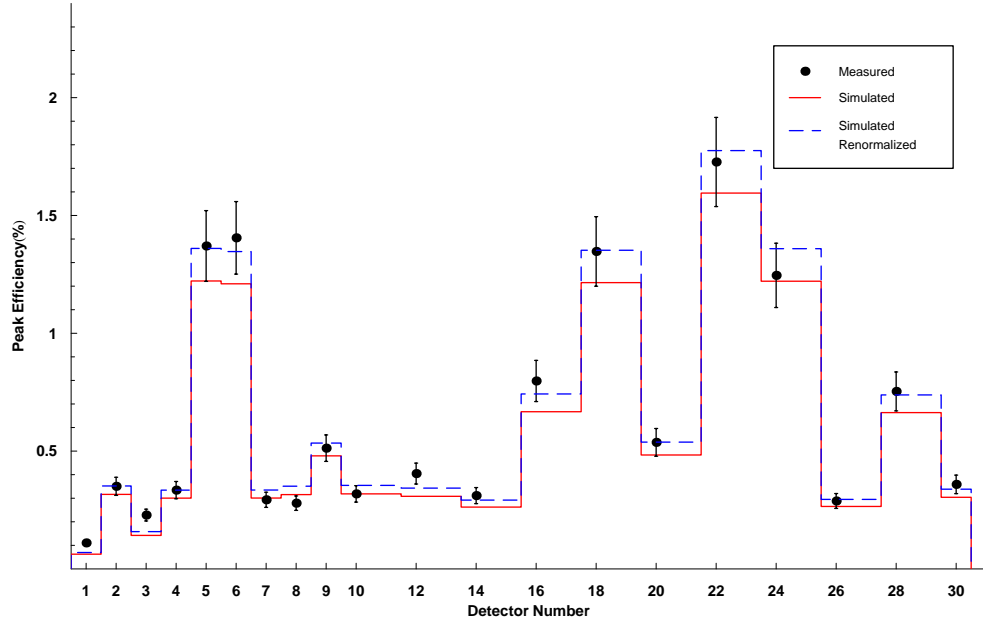


(a) Efficiency comparison between simulation and data for east detectors

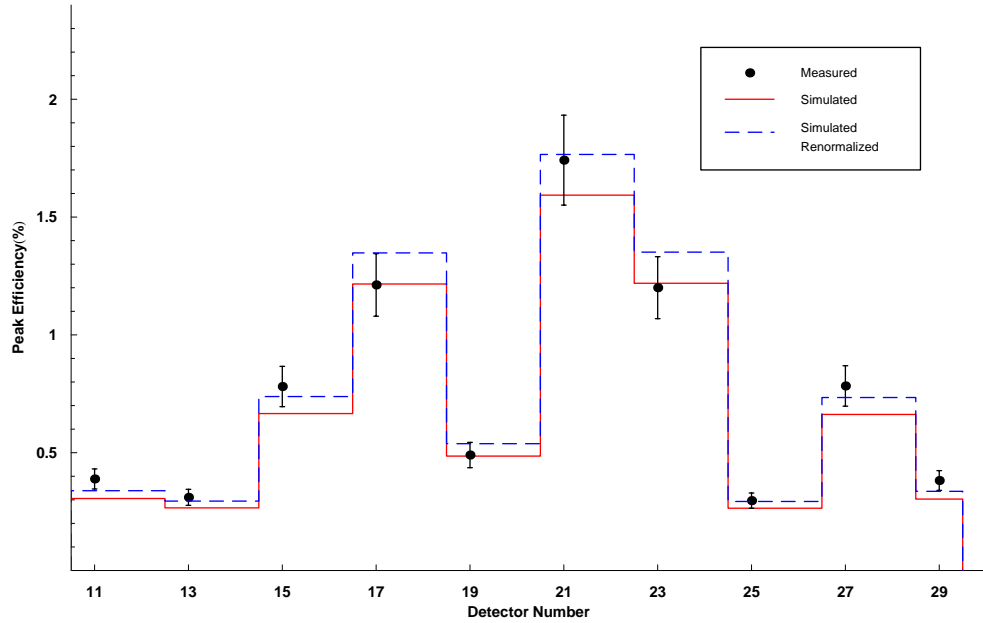


(b) Efficiency comparison between simulation and data for west detectors

Figure 6.34: Re-fit detector by detector efficiency results for the  $^{137}\text{Cs}$  source facing each array half. The red line is the original simulation data and the dashed blue line is the renormalized simulation data.



(a) Efficiency comparison between simulation and data for east detectors



(b) Efficiency comparison between simulation and data for west detectors

Figure 6.35: Re-fit detector by detector efficiency results for the  $^{244}\text{Cm}^{13}\text{C}$  source positioned inside the gas target box at  $z=0$ , and at beam height. The red line is the original simulation data and the dashed blue line is the renormalized simulation data.

## 6.7 Summary of Results

A summary of the analysis of the various source position and geometries is presented in Table (6.4). The low energy  $^{137}\text{Cs}$  source measurements (Run #8157 and #8160) gave excellent agreement between simulation and measurement in the range  $0.05 - 0.31\%$ . This result gave a  $0.19\%$  difference for both array halves combined. This was the best agreement obtained for all sources and source positions. The two measurements which were taken for the high energy gamma sources positioned 15 cm above the target box (Run #8136 and #8170) showed the next best agreement. The difference between measurement and simulation was between  $5.67 - 6.10\%$  in these cases. The result of the  $^{241}\text{Am}^9\text{Be}$  positioned on top of the target box (Run #8106 and #8112) showed a difference between  $5.39 - 6.48\%$ . For both array halves combined, the difference was  $5.79\%$ . The worst agreement occurred with the  $^{244}\text{Cm}^{13}\text{C}$  source positioned inside the gas target box. The difference between simulation and measurement for Run #8182 and #8188 was between  $8.66 - 11.34\%$ . This gives a difference of  $10.43\%$  for both array halves combined.

Run #	Source	Source Position	$\mathcal{E}_D$ (%)	$\Delta\mathcal{E}_D$	$\mathcal{E}_S$ (%)	$\mathcal{E}_R$ (%)	$\Psi_{DS}$ (%)	$\Delta\Psi_{DS}$	$\Psi_{DR}$ (%)	$\Delta\Psi_{DR}$
8182	$^{244}\text{Cm}^{13}\text{C}$	inside box, east	12.974	0.316	11.653	12.970	11.340	0.276	0.031	0.001
8188	$^{244}\text{Cm}^{13}\text{C}$	inside box, west	7.586	0.308	6.981	7.738	8.664	0.351	1.967	0.078
8182+8188	$^{244}\text{Cm}^{13}\text{C}$	inside box, total	20.560	0.441	18.634	20.708	10.338	0.222	0.716	0.015
8106	$^{241}\text{Am}^9\text{Be}$	on box top, east	1.306	0.022	1.396	1.296	6.482	0.109	0.752	0.013
8112	$^{241}\text{Am}^9\text{Be}$	on box top, west	2.295	0.014	2.426	2.294	5.386	0.033	0.058	0.000
8106+8112	$^{241}\text{Am}^9\text{Be}$	on box top, total	3.601	0.026	3.822	3.590	5.786	0.042	0.309	0.002
8136	$^{241}\text{Am}^9\text{Be}$	15 cm above box	0.851	0.014	0.805	0.850	5.670	0.094	0.090	0.002
8170	$^{244}\text{Cm}^{13}\text{C}$	15 cm above box	0.734	0.018	0.692	0.731	6.096	0.151	0.427	0.011
8160	$^{137}\text{Cs}$	on box top, east	5.173	0.012	5.157	5.131	0.312	0.001	0.825	0.002
8157	$^{137}\text{Cs}$	on box top, west	2.589	0.012	2.590	2.580	0.055	0.001	0.352	0.002
8157+8160	$^{137}\text{Cs}$	on box top, total	7.762	0.017	7.747	7.711	0.190	0.001	0.667	0.001

Table 6.4: Measured photopeak efficiencies (denoted  $\mathcal{E}_D$ ) for different array and source geometries and their comparisons to simulation efficiency (denoted  $\mathcal{E}_S$ ) and re-fit simulation efficiency (denoted  $\mathcal{E}_R$ ). The last four columns describe the difference observed between data and simulation (denoted  $\Psi_{DS}$ ) as a percent difference and the error (denoted  $\Delta\Psi_{DS}$ ), and data and re-fit simulation (denoted  $\Psi_{DR}$ ) as a percent difference and the error (denoted  $\Delta\Psi_{DR}$ )



# Chapter 7

## Conclusion

The results of the measurements, given in Table (6.4), suggest agreement between simulation and measurement at the level of less than 1% in the best case and 10% at worst. *This error falls within the original design specifications of 20% intended for measurements performed by the DRAGON spectrometer [1].* The maximum systematic error of 10% introduced by the uncertainty in the efficiency of the gamma-ray array must be taken into account in the calculation of reaction rates found by DRAGON experiments. The DRAGON group has published [35] a result for the resonance strength for the  $^{21}\text{Na}(p,\gamma)^{22}\text{Mg}$  reaction of  $\omega\gamma = 1.03 \pm 0.16_{\text{stat}} \pm 0.14_{\text{sys}}$  where a value in the uncertainty of the gamma array efficiency of 12% was adopted, including uncertainty of efficiency calculations available at the time of publishing. The systematic uncertainty in the published measurement included also the separator transmission efficiency uncertainty (2%), end detector efficiency uncertainty (1%), charge state fraction uncertainty (3%), beam normalization uncertainty (4%), stopping power uncertainty (5%), and gamma array efficiency uncertainty (12%) [35]. Therefore, of the the total systematic uncertainty the array efficiency contributes 44% of the total systematic error of this measurement. To put this contribution into some perspective, if the uncertainty of the array was decreased by a factor of 2 the net effect to the overall uncertainty in  $\omega\gamma$  is a decrease from 21% to 19%. Another DRAGON paper [36] also adopts the 12% gamma efficiency uncertainty value in the data analysis.

## 7.1 Possible Improvements to the Simulation

The systematic difference between data and measurement is of greater concern and could be explained by two possible factors. First, the GEANT simulation was built using the specifications for the detectors from only one detector manufacturer. The Scionix and Bicron detectors have an aluminum casing which differs slightly in thickness and as a consequence could affect the absorption of gamma rays by aluminum (See §3.2). The simulation was built with the specifications of the Bicron detectors which have a thickness of 0.635 mm. The Scionix detectors have an aluminum wall thickness of 0.500 mm. A single aluminum thickness was used in the simulation since it was expected that such a change would produce a small effect in the photopeak efficiency. In the future, the varying detector aluminum thicknesses could be written into the simulation code and tested.

A second, possibly more significant factor, affecting the measurements was that both the  $^{244}\text{Cm}^{13}\text{C}$  and  $^{241}\text{Am}^9\text{Be}$  sources had dimensions of 1 cm and therefore were not point-like as simulated. The measurements which showed the greatest deviation from simulation were those taken with the source inside the gas target box. This would have made the source to crystal face distance on the order of a few cm's. The closest detectors, i.e. those against the gas target box, were within 5 cm of the source. At this distance the source cannot be considered point-like. Evidence that this effect might be important can be taken from the fact that the data to simulation difference decreased as the source was moved further away from the array, which would make the source more point-like. At 15 cm above the target box with the array halves pulled back by  $\approx 31.5$  cm, the overall difference between data and simulation was found to be 6% for the  $^{244}\text{Cm}^{13}\text{C}$  as compared to 10% for the same source positioned within the gas target. If a more point-like source could be obtained or if an extended source geometry were simulated this effect could be tested.

With regards to the renormalization procedure of §6.6, Table (6.3) does not show a single value of  $A$  for varying geometries which may suggest a possible correlation between error and geometry. The value of  $A$  for the  $^{244}\text{Cm}^{13}\text{C}$  source placed inside the target has a similar value for both the east and west measurements. This value

differs slightly from those where the source was placed at a distance 15 cm above the gas target box. At the same time the values of  $A$  agrees for the two different source measurements where the sources were placed 15 cm above the gas target box. Measurements using the  $^{244}\text{Cm}^{13}\text{C}$  and  $^{137}\text{Cs}$  sources placed on top of the target box do not indicate a clear correlation to geometrical effects. The renormalization procedure produces a result which will force the simulation to better agree with data for all cases except for the  $^{137}\text{Cs}$  measurements, but this alone is not helpful in indicating how to improve the simulation. It may be necessary to analyze more measurements with sources placed inside the gas target to determine if a consistent value of  $A$  arises which could be used to renormalize simulated efficiency predictions without modifying the simulation.

# Bibliography

- [1] The Recoil Group. The DRAGON facility for explosive nucleosynthesis at ISAC. TRIUMF Internal Report, 1997.
- [2] <http://csep10.phys.utk.edu/guidry/nc-state-html/cno.html>. This web page and the accompanying figures are maintained by Mike Guidry.
- [3] C.E. Rolfs and W.S. Rodney. *Cauldrons in the Cosmos*. The University of Chicago Press, 1988.
- [4] A.E Champagne and M. Wiescher. Explosive hydrogen burning. *Annual Review of Nuclear and Particle Science*, 42:39–76, 1992.
- [5] G.F. Knoll. *Radiation Detection and Measurement*. John Wiley and Sons, 1989.
- [6] S.M. Shafroth. *Scintillation Spectroscopy of Gamma Radiation*. Gordon and Breach, 1967.
- [7] B. M. Tissue, 1996. <http://elchem.kaist.ac.kr/vt/chem-ed/optics/detector/pmt.htm>.
- [8] D.A.Hutcheon, S. Bishop, L. Buchmann, M. L. Chatterjee, A. A. Chen, J. M. D’Auria, S. Engel, D. Gigliotti, U. Greife, D. Hunter, A. Hussein, C.C. Jewett, N. Khan, A. M. Laird, M. Lamey, W. Liu, A. Olin, D. Ottewell, J. G. Rogers, G. Roy, H. Sprenger, and C. Wrede. The dragon facility for nuclear astrophysics at TRIUMF-ISAC: design, construction and operation. *Nuclear Instruments and Methods in Physics A*, 498:190–210, 2003.

- [9] Application Software Group Computing and Networks Division. *GEANT Detector Description and Simulation Tool*, 1994. GEANT Manual.
- [10] S. Croft. The use of neutron intensity calibrated  $^9\text{Be}(\alpha, n)$  sources as 4438 keV gamma-ray reference standards. *Nuclear Instruments and Methods in Physics A*, 281:103–116, 1989.
- [11] J.K. Dickens and R.D. Baybarz. A monoenergetic 6130-keV gamma-ray source for detector calibration. *Nuclear Instruments and Methods in Physics A*, 85:143–145, 1970.
- [12] R.L. Heath. Scintillation spectrometry gamma-ray spectrum catalogue. Gamma Ray Spectrometer Center, Idaho National Engineering and Environmental Laboratory, 1997. Revised Edition of Report IDO-16880-1.
- [13] W.F. Hornyak, C.A. Ludemann, and M.L. Roush. Energy levels of  $^{10}\text{B}$ . *Nuclear Physics*, 50:424–449, 1964.
- [14] C.F. von Weizsacker. *Zeitschrift fur Physik*, 38:176, 1937.
- [15] C.F. von Weizsacker. *Zeitschrift fur Physik*, 39:633, 1938.
- [16] H. A. Bethe and C. L. Critchfield. The formation of deuterons by proton combination. *Physical Review*, 54:248–254, 1938.
- [17] E.A. Burbidge, G.R. Burbidge, W.A. Fowler, and F. Hoyle. Synthesis of the elements in stars. *Reviews of Modern Physics*, 29:547–647, 1957.
- [18] R.V. Wagoner. *Astrophysical Journal*, 179:343, 1973.
- [19] S.M. Austin. The creation of the rare light elements - cosmic rays and cosmology. *Progress in Particle and Nuclear Physics*, 7:1, 1981.
- [20] J.N. Bahcall, W.F. Huebner, S.H. Lubnow, N.H. Magee, A.L. Merts, P.D. Parker, B. Rozsnyai, R.K. Ulrich, and M.F. Argo. New solar-neutrino flux calculations and implications regarding neutrino oscillations. *Physical Review Letters*, 45:945–948, 1980.

- [21] J.N. Bahcall and R. Davis. *Essays in Nuclear Astrophysics*. Cambridge University Press, 1982.
- [22] J.D. Moldanado and F.X. Timmes. [http://www.cococubed.com/images/net\\_ppcno/ppcno\\_sdot\\_web.jpg](http://www.cococubed.com/images/net_ppcno/ppcno_sdot_web.jpg).
- [23] A. Formicola, H. Costantini, and G. Imbriani. A new study of the  $^{14}\text{N}(p, \gamma) ^{15}\text{O}$  reaction at low energy. *Nuclear Physics A*, 719:C94–C98, 2003.
- [24] E.E. Salpeter. *Physical Review*, 88:547, 1952.
- [25] J. Benn, E.B. Dally, H.H. Mueller, R.E. Pixley, H.H. Staub, and H. Winkler. *Physical Review Letters*, 20:43, 1966.
- [26] F. Hoyle, D.N.F. Dunbar, W.A. Wenzel, and W. Whaling. *Physical Review*, 92:1095, 1953.
- [27] D. Arnett. *Supernovae and Nucleosynthesis*. Princeton University Press, 1996.
- [28] R.A. Ward, M.J. Newman, and D.D. Clayton. *Astrophysical Journal Supplement*, 31:33, 1976.
- [29] P.P. Eggleton, S. Mitton, and J.J.A. Whelan. *Structure and Evolution of Close Binary Systems*. Reidel, 1960.
- [30] F. Hoyle and W.A. Fowler. *Astrophysical Journal*, 132:565, 1960.
- [31] R. Courant and K.O. Friedrich. *Supersonic Flow and Shock Waves*. Interscience, 1948.
- [32] D. Sugimoto K. Nomoto and S. Neo. *Astrophysics and Space Science*, 39:L37, 1976.
- [33] J. Isern, E. Bravo, A. Hirschmann, and D. Garcia-Senz.  $\gamma$ -ray emission from type ia supernovae. *New Astronomy Reviews*, 48:31–33, 2004.
- [34] M. Zelik, S.A. Gregory, and E.v.P. Smith. *Introductory Astronomy and Astrophysics*. Saunders College Publishing, 1992.

- [35] S. Bishop, R. E. Azuma, L. Buchmann, A. A. Chen, M. L. Chatterjee, J. M. D'Auria, S. Engel, D. Gigliotti, U. Greife, M. Hernanz, D. Hunter, A. Hussein, D. Hutcheon, C. Jewett, J. Jose, J. King, S. Kubono, A. M. Laird, M. Lamey, R. Lewis, W. Liu, S. Michimasa, A. Olin, D. Ottewell, P. D. Parker, J. G. Rogers, F. Strieder, and C. Wrede.  $^{21}\text{Na}(p, \gamma)^{22}\text{Mg}$  reaction and oxygen-neon novae. *Physical Review Letters*, 90:162501, 2003.
- [36] J. M. D'Auria, R. E. Azuma, S. Bishop, L. Buchmann, M. L. Chatterjee, A. A. Chen, S. Engel, D. Gigliotti, U. Greife, D. Hunter, A. Hussein, D. Hutcheon, C.C. Jewett, J. Jose, J.D. King, A. M. Laird, M. Lamey, R. Lewis, W. Liu, S. Michimasa, A. Olin, D. Ottewell, P. D. Parker, J. G. Rogers, C. Ruiz, M. Trinczek, and C. Wrede. The  $^{21}\text{Na}(p, \gamma)^{22}\text{Mg}$  reaction from  $e_{cm}$  200 to 1101 keV in novae and x-ray bursts. *Physical Review C*, 69:065803, 2004.
- [37] S. Bishop. *Direct Measurement of the  $^{21}\text{Na}(p, \gamma)^{22}\text{Mg}$  Resonant Reaction Rate in Nova Nucleosynthesis*. PhD thesis, Simon Fraser University, 2003.
- [38] R.K. Wallace and S.E. Woosley. Explosive hydrogen burning. *The Astrophysical Supplement Series*, 45:389–420, 1981.
- [39] W.R. Leo. *Techniques for Nuclear and Particle Physics Experiments*. Springer-Verlag, 1994.
- [40] C.D. Broyles, D.A. Thomas, and S.K. Haynes. *Physical Review*, 89:715, 1953.
- [41] R.D. Evans. *The Atomic Nucleus*. Krieger, 1982.
- [42] O. Klein and Y. Nishina. *Z.f. Physik*, 52:853, 1929.
- [43] O.H. Nestor and C.Y. Huang. *IEEE Trans*, NS-22:68, 1975.
- [44] R.E. Laxdal. Acceleration of radioactive ions. *Nuclear Instruments and Methods B*, 204:400–409, 2003.
- [45] Wenjie Liu. Charge state studies of heavy ions passing through gas. Master's thesis, Simon Fraser University, 2001.

- [46] Chris Wrede. A double sided silicon strip detector as an end detector for the dragon recoil mass separator. Master's thesis, Simon Fraser University, 2003.
- [47] Bicron corporation. 12345 Kinsman Road, Newbury Ohio 44065-9577, USA.
- [48] Scionix corporation. PO Box 143, 3980 CC Bunnik, The Netherlands.
- [49] Joel G. Rogers. A gamma ray detector array for dragon at ISAC. NSERC grant application, pre-print in appendix (unpublished), 1999.
- [50] L. Bonnet, M. Frederic, P. Leleux, I. Licot, and P. Lipnik. Optimization of NaI(Tl) detector performance in high-background counting rate environments. *Nuclear Instruments and Methods*, A292:243–350, 1990.
- [51] J.G. Rogers and C.J. Batty. Afterglow in lso and its possible effect on energy resolution. *IEEE Trans*, NS-47:438, 2000.
- [52] Midas is a general purpose data aquisition program maintained by Stefan Ritt (<http://midas.psi.ch>), and Pierre-Andre Amaudruz (<http://midas.triumf.ca>).
- [53] Joel Rogers. Internal minutes of the DRAGON meeting for March 4, 2003.
- [54] E. Segré. *Nuclei and Particles*. The Benjamin/Cummings Publishing Company, 1977.
- [55] Application Software Group Computing and Networks Division. *GEANT Detector Description and Simulation Tool*, 1994. PHYS section of the geant manual by M. Maire and F. Caminati.
- [56] Particle Data Group. Review of particle properties. *Physical Review D*, 45:11, 1992.
- [57] J.H. Hubbell, H.A. Gimm, and I. Overbo. Pair, triplet, and total atomic cross sections (and mass attenuation coefficients) for 1 MeV-100 GeV photons in elements Z=1 to 100. *Journal of Physical and Chemical Reference Data*, 9:1023–1147, 1980.



- [58] J.C. Butcher and H. Messel. Electron number distribution in electron - photon showers in air and aluminum absorbers. *Nuclear Physics*, 20:15, 1960.
- [59] J.M. Hammersley and D.S. Handscomb. *Monte Carlo Methods*. John Wiley and Sons Inc, 1964.
- [60] R. Ford and W. Nelson. The eggs code system - version 3. SLAC Report 210, UC 32, 1978.
- [61] Y-S. Tsai. Pair production and bremsstrahlung of charged leptons. *Reviews of Modern Physics*, 46:815, 1974.
- [62] Y-S. Tsai. Erratum: Pair production and bremsstrahlung of charged leptons. *Reviews of Modern Physics*, 49:421, 1977.
- [63] H. Messel and D.F. Crawford. *Electron-Photon Shower Distribution Function*. Pergamon Press, 1970. volume 3.
- [64] B. Rossi. *High Energy Particles*. Prentice Hall, 1952.
- [65] F. Biggs and R. Lighthill. Analytical approximations for x-ray cross sections 3. Sandia National Lab., SAND87-0070 UC-34, 1987.
- [66] Application Software Group Computing and Networks Division. *GEANT Detector Description and Simulation Tool*, 1994. TRAK section of the geant manual by F. Bruyant.
- [67] Peter Gumplinger. TRIUMF, Private Communication.
- [68] D.G. Gigliotti, J.G. Rogers, and A.H. Hussein. Calibration and simulation of a gamma array for DRAGON at ISAC. *Nuclear Instruments and Methods in Physics B*, 204:671–677, 2003. EMIS-14 Conference Proceedings.
- [69] M. Mehroff, M. Aliotta, I.J.R. Baumvol, H-W. Becker, M. Berheide, L. Borucki, J. Domke, F. Gorris, S. Kubsy, N. Piel, G. Roters, C. Rolfs, and W.H. Schulte. Gamma-ray detection with a  $4\pi$  NaI spectrometer for material analysis. *Nuclear Instruments and Methods in Physics B*, 132:671–684, 1997.

- [70] V.Kolle, U.Kolle, S.E. Braitmayer, P. Mohr, S. Wilmes, G. Staudt, J.W. Hammer, M. Jaeger, H. Knee, R. Kunz, and A. Mayer. Capture reactions at astrophysically relevant energies: Extended gas target experiments and GEANT simulations. *Nuclear Instruments and Methods*, 431:160–176, 1999.
- [71] Z. Elekes, T. Belgya, G.L. Molnar, A.Z. Kiss, M. Csatos, J. Gulyas, A. Krasznahorkay, and Z. Mate. Absolute full-energy peak efficiency calibration of a clover-BGO detector system. *Nuclear Instruments and Methods*, 503:580–588, 2003.
- [72] M. Yoshimori, H. Watanabe, and F. Shiraishi. Reponse of a 7.6 cm x 7.6 cm bismuth germanate spectrometer for solar gamma ray observations. *Nuclear Instruments and Methods*, 245:191–198, 1986.
- [73] D.M. Drake, L.R. Nilsson, and J. Faucett. Bismuth germanate scintillators as detectors for high-energy gamma radiation. *Nuclear Instruments and Methods*, 188:313–317, 1981.
- [74] E. Waibel and B. Grosswendt. Determination of detector efficiencies for gamma ray energies up to 12 mev i. experimental methods. *Nuclear Instruments and Methods*, 131:133–141, 1975.
- [75] P. Dryak, T. Novotny, P. Kovar, and M. Kralik. Determination of the 6.13 MeV photon emission from the  $\text{Pu}(\alpha, n)^{13}\text{C}$  source and half life of  $^{16}\text{N}$ . *Nuclear Instruments and Methods*, 369:441–444, 1996.
- [76] B.K. Kamboj and M.G. Shahani. Precise measurement of the gamma to neutron ratio of an Am- $\alpha$ -Be neutron source using an improved maganese bath technique. *Nuclear Instruments and Methods in Physics A*, 244:513–515, 1986.
- [77] K.W. Geiger and L. Van Der Zwan. Neutrons and  $\gamma$ -rays from radioactive  $^{13}\text{C}(\alpha, n)$  sources. *Nuclear Instruments and Methods*, 157:199–201, 1978.
- [78] AEA Technology Sources Catalogue, 2003. 329 Harwell, Didcot, OX, United Kingdom.

- [79] J. Berger and S.M. Seltzer. Response functions for sodium iodide scintillation detectors. *Nuclear Instruments and Methods*, 104:317, 1972.
- [80] Hu-Xia Shi, Bo-Xian Chen, Ti-Zhu Li, and Di Yun. Precise monte carlo simulation of gamma-ray response functions for an NaI(Tl) detector. *Applied Radiation and Isotopes*, 57:517–524, 2002.
- [81] Dan Melconian. TRIUMF, Private Communication.
- [82] K. Levenberg. A method for the solution of certain problems in least squares. *Quart. Appl. Math*, 2:164–168, 1944.
- [83] D. Marquardt. An algorithm for least-squares estimation of nonlinear parameters. *SIAM J. Appl. Math*, 11:431–441, 1963.
- [84] R.M. Green and R.J. Finn. *Nuclear Instruments and Methods*, 34:72, 1965.
- [85] K.L. Coop and H.A. Grench. *Nuclear Instruments and Methods*, 36:339, 1965.
- [86] R.L. Heath, R.G. Helmer, L.A. Schmittroth, and G.A. Cazier. *Nuclear Instruments and Methods*, 47:281, 1967.
- [87] B. Chinaglia and R. Malvano. *Nuclear Instruments and Methods*, 45:10, 1961.
- [88] K.J. Van Oostrum and A.C. Meijer. *Nuclear Instruments and Methods*, 10:31, 1961.
- [89] N.H. Lazar. *IRE Trans. Nucl. Sci.*, NS-5:138, 1958.
- [90] N.H. Lazar, R.C. Davis, and P.R. Bell. Peak efficiency of NaI. *Nucleonics*, 14:52, 1956.
- [91] R.L. Heath. Scintillation spectrometry, gamma-ray spectrum catalogue. *USAEC Report*, 16408, 1957.
- [92] S.H. Vegors, L.L. Marsden, and R.L. Heath. *USAEC Report*, IDO 16370, 1958.

- [93] H. Leutz, G. Schulz, and L. Van Gelderen. *Nuclear Instruments and Methods*, 40:257, 1966.
- [94] U.C. Mishra and S. Sadasivan. *Nuclear Instruments and Methods*, 69:330, 1969.
- [95] E.A. Wolicki, R. Jastrow, and F. Brooks. Calculated efficiencies of NaI crystals. NRL Report 4833, 1956.
- [96] C.D. Zerby and H.S. Moran. Calculation of the pulse-height response of NaI(Tl) scintillation counters. *Nuclear Instruments and Methods*, 14:115–124, 1961.
- [97] C. Weitkamp. *Nuclear Instruments and Methods*, 23:13, 1963.
- [98] M. Giannini, P.R. Oliva, and M.C. Ramorino. *Nuclear Instruments and Methods*, 81:104, 1970.
- [99] S.M. Seltzer and M.J. Berger. *ANS Trans*, 14:124, 1971.
- [100] W.F. Miller and W.J. Snow. ANL-6318, Argonne National Laboratory(unpublished), 1961.
- [101] B. Grosswendt and E. Waibel. Monte carlo calculations of the intrinsic gamma ray efficiencies of cylindrical nai(tl) detectors. *Nuclear Instruments and Methods*, 133:25–28, 1976.
- [102] M. Irfan and R.D.G Prasad. Relative photopeak efficiencies and photofractions of a 2" x 2" CsI(Tl) crystal. *Nuclear Instruments and Methods*, 88:165–176, 1970.
- [103] Y.S. Selim, M.I. Abbas, and M.A. Fawzy. Analytical calculation of the efficiencies of gamma scintillators. part I:total efficiency for coaxial disk sources. *Radiation Physics and Chemistry*, 53:589–592, 1998.
- [104] Y.S. Selim, M.I. Abbas, and M.A. Fawzy. Source-detector geometrical efficiency. *Radiation Physics and Chemistry*, 44:1–4, 1994.

- [105] Physics analysis workstation. PAW is maintained at CERN-European Laboratory for Particle Physics, <http://wwwasd.web.cern.ch/wwwasd/paw/>.
- [106] O. Hausser, M. A. Lone, T. K. Alexander, S. A. Kushneriuk, and J. Gascon. The prompt response of bismuth germanate and NaI(Tl) scintillation detectors to fast neutrons. *Nuclear Instruments and Methods*, 213:301, 1983.
- [107] D. Lang. *HVCALIB and CFDCALIB: Programmer's Manual*, 2000. TRIUMF Summer Student Report.
- [108] J.G. Rogers. TRIUMF, How to calibrate the DRAGON gamma array. <http://www.triumf.ca/dragon/gammaarray.html>.

# Appendix A

## Glossary of Selected Terms and Acronyms

**DRAGON** - Detector of Recoils And Gammas Of Nuclear reactions

**ISAC** - Isotope Separator and ACcelerator

**TRIUMF** - TRI University Meson Facility

**BGO** - scintillator crystals composed of bismuth(Bi), germanium(G) and oxygen(O) (i.e. bismuth germanate)

**EMS** - ElectroMagnetic Separator

**Leaky Beam** - beam which has made its way through the DRAGON separator and is detected in the end detector along with the recoil ions of interest

**GEANT** - GEometry And Tracking tool, is a simulation package used for tracking various particles through different media

**NaI** - scintillator crystals composed of sodium(Na) and iodide(I)

**CNO cycle** - a stellar burning reaction network that involves carbon, nitrogen and oxygen

**hot CNO cycle** - a stellar burning reaction network involving carbon, nitrogen and oxygen that occurs at temperatures above  $1-4 \times 10^8$  K

**alpha particle** - the nucleus of a helium atom consisting of two protons and two neutrons

**beta particle** - particle identical to the electron except that it originates from the nucleus of an atom rather than outside of the nucleus as with the electron

**gamma ray** - a high energy photon

**ADC** - Analogue to Digital Converter electronics module

**PMT** - PhotoMultiplier Tube is the part of a scintillation detector which collects and amplifies the scintillation light

**TDC** - Time to Digital Converter

## Appendix B

### Tabulated Efficiency Data

The following tables contain the data from which the efficiency figures in §6 were plotted. The first column is the detector number, the second column is the measured efficiency, the third column is the estimated error for the measured efficiency, the fourth column is the calculated efficiency by the GEANT simulation, the fifth column is the GEANT efficiency renormalized. The details of the this renormalization are described in §6.6



Detector #	$\mathcal{E}_{Data}$	$\Delta\mathcal{E}_{Data}$	$\mathcal{E}_{Simulation}$	$\mathcal{E}_{Refit}$
1	0.048404	0.003558	0.050860	0.047210
2	0.069735	0.005125	0.074060	0.068740
3	0.055021	0.004044	0.058550	0.054350
4	0.083741	0.006154	0.087950	0.081630
5	0.091079	0.006694	0.096070	0.089170
6	0.093306	0.006857	0.097110	0.090140
7	0.087101	0.006401	0.088080	0.081760
8	0.070829	0.005205	0.076560	0.071060
9	0.085518	0.006285	0.086670	0.080450
10	0.072683	0.005342	0.078440	0.072810
12	0.055600	0.004086	0.058850	0.054620
14	0.048803	0.003587	0.055950	0.051930
16	0.058870	0.004327	0.062790	0.058280
18	0.056411	0.004146	0.061710	0.057280
20	0.054519	0.004007	0.058060	0.053890
22	0.057055	0.004193	0.064560	0.059920
24	0.058304	0.004285	0.060040	0.055730
26	0.048623	0.003574	0.057810	0.053660
28	0.058213	0.004278	0.062640	0.058140
30	0.051931	0.003817	0.059500	0.055230

Table B.1: Measured and calculated detector efficiencies from the  $^{241}\text{Am}^9\text{Be}$  source at 4.44 MeV positioned on top of the gas target box at  $z=0$ , facing the east array half

Detector #	$\mathcal{E}_{Data}$	$\Delta\mathcal{E}_{Data}$	$\mathcal{E}_{Simulation}$	$\mathcal{E}_{Refit}$
11	0.058326	0.004287	0.058370	0.058250
13	0.057474	0.004224	0.057090	0.056970
15	0.060366	0.004437	0.062220	0.062090
17	0.063773	0.004687	0.062700	0.062570
19	0.058761	0.004319	0.057220	0.057100
21	0.066583	0.004894	0.065630	0.065490
23	0.063410	0.004660	0.062750	0.062620
25	0.056010	0.004117	0.056700	0.056580
27	0.061173	0.004496	0.063700	0.063570
29	0.058451	0.004296	0.058820	0.058700

Table B.2: Measured and calculated detector efficiencies from the  $^{241}\text{Am}^9\text{Be}$  source at 4.44 MeV positioned on top of the gas target box at  $z=0$ , facing the west array half

Detector #	$\mathcal{E}_{Data}$	$\Delta\mathcal{E}_{Data}$	$\mathcal{E}_{Simulation}$	$\mathcal{E}_{Refit}$
11	0.040753	0.002998	0.039050	0.041230
12	0.040161	0.002955	0.038410	0.040550
13	0.036093	0.002656	0.032160	0.033950
14	0.033914	0.002495	0.033110	0.034960
15	0.049181	0.003617	0.048600	0.051310
16	0.050147	0.003688	0.048330	0.051020
17	0.043561	0.003204	0.039540	0.041740
18	0.042115	0.003098	0.038060	0.040180
19	0.036524	0.002687	0.033640	0.035520
20	0.036260	0.002668	0.034220	0.036130
21	0.053691	0.003949	0.050710	0.053540
22	0.052232	0.003842	0.049940	0.052720
23	0.042725	0.003143	0.040320	0.042570
24	0.042051	0.003093	0.039630	0.041840
25	0.034625	0.002548	0.033060	0.034900
26	0.033446	0.002461	0.033280	0.035140
27	0.050787	0.003735	0.048290	0.050980
28	0.051608	0.003796	0.047420	0.050060
29	0.041127	0.003025	0.038800	0.040960
30	0.039908	0.002936	0.038680	0.040840

Table B.3: Measured and calculated detector efficiencies from the  $^{241}\text{Am}^9\text{Be}$  source at 4.44 MeV positioned 15 cm above gas target box at  $z=0$ , illuminating both array halves simultaneously

Detector #	$\mathcal{E}_{Data}$	$\Delta\mathcal{E}_{Data}$	$\mathcal{E}_{Simulation}$	$\mathcal{E}_{Refit}$
11	0.035405	0.003881	0.032800	0.034650
12	0.034189	0.003748	0.032770	0.034620
13	0.030988	0.003397	0.027990	0.029570
14	0.028363	0.003109	0.028920	0.030550
15	0.043536	0.004772	0.041110	0.043430
16	0.042960	0.004708	0.041350	0.043690
17	0.037198	0.004077	0.034340	0.036280
18	0.035405	0.003881	0.034360	0.036300
19	0.031308	0.003432	0.029380	0.031040
20	0.029899	0.003278	0.029000	0.030640
21	0.048018	0.005262	0.042190	0.044570
22	0.045713	0.005010	0.042750	0.045160
23	0.036814	0.004035	0.033530	0.035420
24	0.036110	0.003958	0.035250	0.037240
25	0.030219	0.003313	0.029100	0.030740
26	0.028043	0.003074	0.027860	0.029430
27	0.045137	0.004947	0.040850	0.043160
28	0.044625	0.004891	0.042850	0.045270
29	0.035726	0.003916	0.032570	0.034410
30	0.034573	0.003790	0.033070	0.034940

Table B.4: Measured and calculated detector efficiencies from the  $^{244}\text{Cm}^{13}\text{C}$  source at 6.13 MeV positioned 15 cm above gas target box at  $z=0$ , illuminating both array halves simultaneously

Detector #	$\mathcal{E}_{Data}$	$\Delta\mathcal{E}_{Data}$	$\mathcal{E}_{Simulation}$	$\mathcal{E}_{Refit}$
11	0.137724	0.003538	0.148000	0.141030
13	0.133674	0.003435	0.140300	0.133690
15	0.134708	0.003461	0.158200	0.150750
17	0.148279	0.003807	0.154800	0.147510
19	0.137054	0.003521	0.145400	0.138550
21	0.157662	0.004047	0.161500	0.153890
23	0.160678	0.004124	0.156200	0.148840
25	0.149955	0.003850	0.139000	0.132450
27	0.151295	0.003884	0.156100	0.148740
29	0.133200	0.003423	0.146200	0.139310

Table B.5: Measured and calculated detector efficiencies from the  $^{137}\text{Cs}$  source at 0.662 MeV positioned on top of the gas target box at  $z=0$ , facing the east array half

Detector #	$\mathcal{E}_{Data}$	$\Delta\mathcal{E}_{Data}$	$\mathcal{E}_{Simulation}$	$\mathcal{E}_{Refit}$
12	0.153439	0.003912	0.147770	0.151120
14	0.145814	0.003718	0.140980	0.144170
16	0.163408	0.004166	0.157570	0.161140
18	0.154474	0.003938	0.154700	0.158210
20	0.146096	0.003725	0.143600	0.146850
22	0.162287	0.004138	0.161400	0.165060
24	0.171230	0.004366	0.156300	0.159840
26	0.140825	0.003590	0.139900	0.143070
28	0.167747	0.004277	0.158300	0.161890
30	0.141312	0.003603	0.147500	0.150840

Table B.6: Measured and calculated detector efficiencies from the  $^{137}\text{Cs}$  source at 0.662 MeV positioned on top of the gas target box at  $z=0$ , facing the west array half

Detector #	$\mathcal{E}_{Data}$	$\Delta\mathcal{E}_{Data}$	$\mathcal{E}_{Simulation}$	$\mathcal{E}_{Refit}$
1	0.110443	0.012102	0.062560	0.069630
2	0.350553	0.038405	0.316300	0.352060
3	0.228547	0.025040	0.142200	0.158280
4	0.334407	0.036636	0.300400	0.334360
5	1.370494	0.150134	1.222000	1.360160
6	1.405077	0.153922	1.210000	1.346800
7	0.293345	0.032138	0.300800	0.334810
8	0.279061	0.030573	0.315400	0.351060
9	0.512476	0.056143	0.479800	0.534050
10	0.318500	0.034897	0.318500	0.354510
12	0.404647	0.044331	0.308100	0.342930
14	0.311173	0.034091	0.262400	0.292070
16	0.797623	0.087379	0.667100	0.742520
18	1.347331	0.147597	1.215000	1.352370
20	0.537107	0.058841	0.483500	0.538160
22	1.726954	0.189182	1.595000	1.775330
24	1.245767	0.136471	1.221000	1.359050
26	0.288369	0.031593	0.265100	0.295070
28	0.753303	0.082524	0.663400	0.738400
30	0.358787	0.039307	0.304000	0.338370

Table B.7: Measured and calculated detector efficiencies from the  $^{244}\text{Cm}^{13}\text{C}$  source at 6.13 MeV positioned inside the gas target box at  $z=0$ , facing the east array half, array is in the fully closed position

Detector #	$\mathcal{E}_{Data}$	$\Delta\mathcal{E}_{Data}$	$\mathcal{E}_{Simulation}$	$\mathcal{E}_{Refit}$
1	0.048404	0.003558	0.050860	0.047210
2	0.069735	0.005125	0.074060	0.068740
3	0.055021	0.004044	0.058550	0.054350
4	0.083741	0.006154	0.087950	0.081630
5	0.091079	0.006694	0.096070	0.089170
6	0.093306	0.006857	0.097110	0.090140
7	0.087101	0.006401	0.088080	0.081760
8	0.070829	0.005205	0.076560	0.071060
9	0.085518	0.006285	0.086670	0.080450
10	0.072683	0.005342	0.078440	0.072810
12	0.055600	0.004086	0.058850	0.054620
14	0.048803	0.003587	0.055950	0.051930
16	0.058870	0.004327	0.062790	0.058280
18	0.056411	0.004146	0.061710	0.057280
20	0.054519	0.004007	0.058060	0.053890
22	0.057055	0.004193	0.064560	0.059920
24	0.058304	0.004285	0.060040	0.055730
26	0.048623	0.003574	0.057810	0.053660
28	0.058213	0.004278	0.062640	0.058140
30	0.051931	0.003817	0.059500	0.055230

Table B.8: Measured and calculated detector efficiencies from the  $^{244}\text{Cm}^{13}\text{C}$  source at 6.13 MeV positioned inside the gas target box at  $z=0$ , facing the west array half, array is in the fully closed position

# Appendix C

## Pre Run Gamma Array Setup Procedure

### C.1 Gain Matching the BGO Detectors

The BGO scintillation detectors of the array need individual positive, high voltage values. The magnitude of the high voltage supplied to one PMT is proportional to the gain of the detector. The electronic components of the tubes vary enough that for a given fixed voltage applied to different PMT's the gain may be different than any other tube. Since it is desirable that the same gamma energy measured by any tube fall into the same ADC channel, it is necessary to adjust each voltage. For example, it would be preferable that the peak from a 4.44 MeV gamma source fall in the same ADC channel (e.g. channel 444). To gain match all 30 detectors a calibration program was written by Dustin Lang of TRIUMF [107]. The program requires two gamma spectra to be taken at different high voltage levels. A peak search and peak integration is then done for each of the gamma spectra to find the ADC channel that is the centroid of each peak. The two data sets then give two points (for each detector) which can be interpolated or extrapolated on a line to predict the voltage that places the peak in the required ADC channel.

A few useful definitions for further understanding of the calibration process follow:

***channel*** - The number (1-1023) produced by an ADC conversion.

***gate*** - The signal applied to the gate input, the width of which is typically 650-1000. This parameter is set in (/Equipment/gTrigger/Settings/ADC)\_gate\_width\_ns).

***pedestal*** - The channel number produced when a gate occurs with no signal, varies with gate-width and from ADC to ADC.

***offset*** - A number selected by ../Settings/Poffset, which is added by the Midas data acquisition software to the measured pedestals. In Autoload mode the offset and pedestals are acquired and stored in /Settings/Pedestals and also in hardware. The choice of Poffset value effects data compression by hardware-shifting channels less than Poffset to negative values which effectively suppresses them from the event record. A typical value of Poffset=25 seems to work for suppressing most of the pile-up gammas from RIB spills for gamma array rates up to 1000/s (above a 2 MeV CFD threshold).

***gain*** - The slope of the linear conversion from gamma energy to ADC-channel-number, adjusted to be the same (via ODB datum /Settings/HV) for all 30 ADC's by the calibration procedure. The conversion is:  $\text{channel} = \text{gain} * \text{energy} - \text{offset}$

***“valley” argument*** - [valley <fraction>] tells *hvcplib* how to determine if a valley has been found on the energy side of the photopeak. As soon as a channel is found scanning down from the peak, which contains fewer counts than *fraction* times the counts in the peak, then that channel is chosen as the beginning of the photopeak. The default value is 0.7. (Note that it is not sensible to set this value above 1.0) If the calibration peak has another peak nearby so that the valley between them is not well resolved, then it is possible that *hvcplib* will not “see” two peaks and will claim that the peak is located somewhere between the two peaks. This problem can be resolved by increasing *valley*. On the other hand, if *hvcplib* is getting “caught” on an incorrect (due to high statistics) high-energy peak which does not have significantly more counts than its neighbours, then decreasing *valley* may cause *hvcplib* to skip over

this false peak.

The procedure [108] to gain match the array follows. It should be noted that all commands should be typed in the Midas “odb window” unless otherwise stated.

1. Open a terminal window and ssh into midmes01
2. Start the odb by typing “odb” in this terminal window
3. Set the desired hardware threshold by following instructions in the section “Adjusting the Software Threshold”
4. In the odb window type “set /Equipment/gTrigger/Settings/Autoload\_Pedestals y”. This will establish the pedestal values for all the detectors. The values for the pedestals differ due to variance in gain of the PMT’s
5. Type “start” data acquisition, with all gamma sources far away.
6. Start another midmes01 terminal window and type “/home/dragon/calib/hvcontrol-1.8.3/hvcontrol”. The statement “HV Control ready” will appear at the bottom of the screen when hvcontrol has been started properly.
7. Type “stop”. This will stop data acquisition
8. Type “set /Equipment/gTrigger/Settings/Autoload\_pedestals n”.
9. Type “set /Logger/Data dir” /data/dragon/data0.
10. Tape the 9x20mm- $^{244}\text{Cm}^{13}\text{C}$  source capsule onto the target box at the “source” position (If this is not marked the position is approximately at  $z = 0$ , at beam height on the west side of the target). Move the West array to be positioned 10 mm from the box. CAREFUL not to crush the source between the array and the box. There should still be at least 1 mm clearance after the array is cranked in.
11. “start” and acquire data for 10 minutes, which should give at least 150 counts/channel at the full-energy peaks’ positions, i.e. on the line in Fig. C.1.



12. In the PAW++ “Executive” window: “hvsuggest valley 0.9 file eee”. file = /data/dragon/data0/runNNNNN.odt and NNNNN = the run number echoed by Midas following the last “start”. eee is an ADC channel number selected to be  $\approx 100$  more or less than the peaks’ average channel (See Fig. C.1), depending on whether it is desired to decrease or increase the gains.
13. Set the trial voltages with: “load suggested-after-hv.odt” and “set /Equipment/gTrigger/Settings/ChangeHV y”.
14. “start”, acquire data for 10 minutes, then “stop”.
15. In the “Executive” window: “hvcalib valley 0.9 file file1 EEE”, where file is as above, file1 contains the most recent run-number, and EEE is the channel-number desired for the 6.13 MeV, typically 613. This choice for EEE establishes the array gain, and by extrapolation, establishes the maximum measurable gamma ray energy at channel 1023.
16. Establish the final hardware voltages with: “load suggested-hv.odt” and “set /Equipment/gTrigger/Settings/ChangeHV y”.
17. Acquire a final spectrum, as in step 11 above, and see that the peaks line up all at the same channel, as in Fig. C.1. If not, repeat steps 11-15.
18. Remove the source and crank the array to its normal position.

When the gain matching is complete, spectrum 1000 should show output similar to Fig. C.1:

## C.2 Adjusting the Software Threshold

A software threshold can be applied to the gamma detectors for the purpose of offline and online analysis. The threshold for the gamma detectors can be done in three ways: predefined, custom defined or manually defined. The first can be made without knowing anything about the detectors except for the gain ratio. For example if the

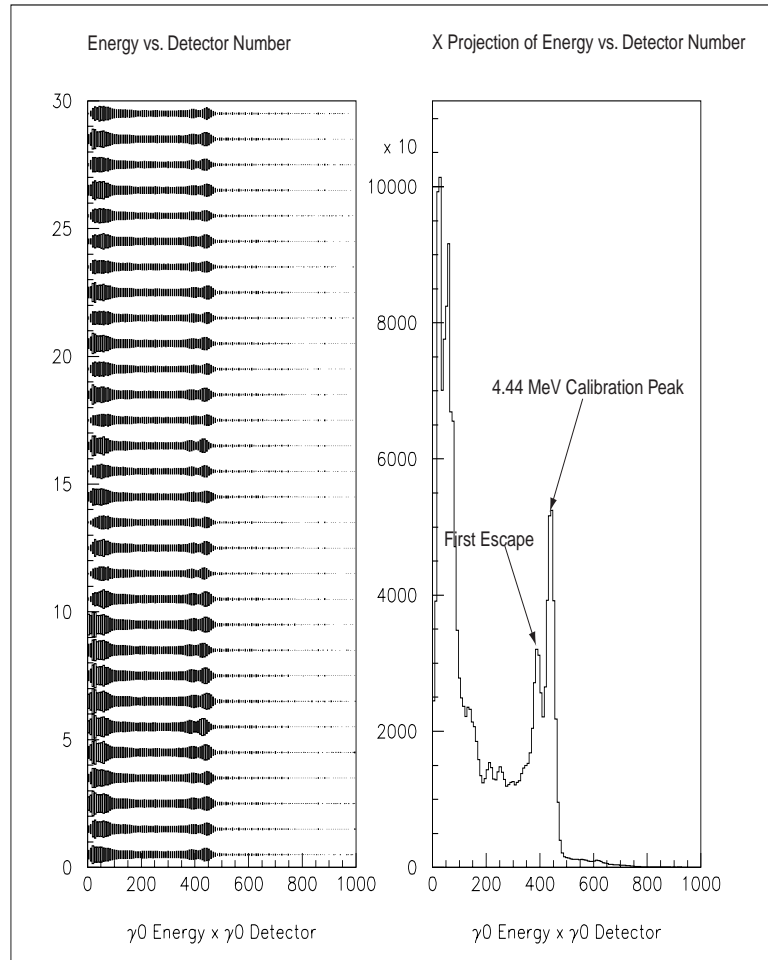


Figure C.1: Result of gain matching the 30 BGO detectors

ratio is 100 channels/MeV then predefined thresholds can be loaded by the following method:

1. Open a terminal window and ssh to midmes01.
2. Type: “odb” (this will open the odb controls)
3. Type: “load presetthreshold.odb”, where “presetthreshold” can be the following:
  - (a) 300thresh
  - (b) 200thresh

(c) 100thresh

(d) 50thresh

4. Once the threshold is set you may exit the odb by typing “exit” and close the terminal window.

The digits represent the threshold in units of MeV if a scale of 1MeV/100 bins is chosen. For example, 200thresh represents a threshold of 2.00 MeV.

The second method is to set a custom threshold by the following method:

1. Open a terminal window and ssh to midmes01.
2. Switch to /home/dragon/online/data0
3. Type: “paw++ &”
4. In the paw executive window (top left hand corner window) type “cfcalib cfdcalibpoint1.oddb cfdcalibpoint2.oddb <targetvalue>” where <targetvalue> is the value of the threshold you would like to set in units of MeV. For example, a <targetvalue> = 200 represents a threshold of 2 MeV.
5. Start another terminal on midmes01 and type “odb”
6. type: “load suggested-cfd.oddb” in the odb window. This will set the threshold value you entered in the previous steps.
7. Once the thresholds are set paw++ and the odb can be exited.

The third method is to produce the threshold settings manually. This only needs to be done for specific cases or if for some reason the files above are missing. The threshold settings are generated by a similar method to the gain matching technique. Two runs are taken at different threshold values and then the program produces a sloped line which can be used to interpolate or extrapolate the required threshold.

The following steps are taken to produce a manually set threshold.

1. Gain match the detectors as explained in Section 8.1 and then with the source still in place proceed to step 2.
2. Set all detectors to the same threshold value by typing “set /Equipment/gTrigger /Settings/CFD\_Threshold[\*] *<some-value>*”. Where *some-value* should be a number around the threshold setting you wish to set. (e.g. a setting of 2MeV would be a setting of somewhere between 15-20, so the first value could be 10)
3. Start a run by typing “start” in the ODB window and acquire until 100 counts or more are collected in the photopeak of all detectors
4. Stop the run and set all detectors to a different threshold value say 20 or 25. Acquire data again as in step 3.
5. In the paw++ “Executive Window” type “cfdcilib *<runn1.odb> <runn2.odb> <required-value>*”. Where *n1* is the the run number of the first run taken and *n2* is the second. *required-value* is the channel value you wish to place the threshold in. (e.g. if you wish to put a 2 MeV threshold in channel 200 then *required-value*=“200”. (e.g. cfdcalib *run10234.odb run10235.odb 200*)
6. In the ODB window type “load suggested-cfd.odb” to establish the software threshold. If the threshold is not at the required position then the value of *required-value* can be changed until the desired value is reached.

A figure showing a 2MeV software threshold is shown in Fig. C.2. It should be noted that this threshold is “soft” due to detector resolution.

## C.3 Gain Drift

### C.3.1 Temperature Fluctuations

During periods of beam running a drift in the established gains of the BGO detectors has been observed. It is hypothesized that this drifts are due to temperature changes around the detectors. More study is intended to determine if this is actually the case.

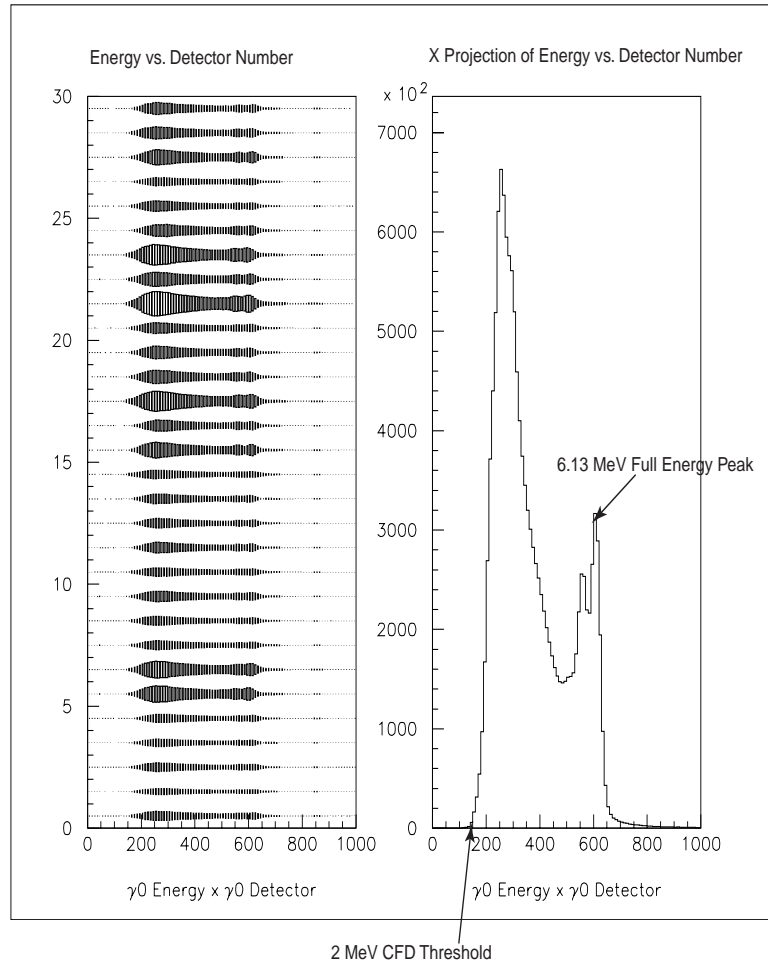


Figure C.2: 2 MeV software threshold placed on a sample spectra from  $^{244}\text{Cm}^{13}\text{C}$

The detectors are mounted on a platform which is close proximity to pumps which tend to give off heat as a function of pumping load. There are also temperatures fluctuations due to seasonal and diurnal cycles in the experimental hall. It is also possible that the position of the array halves when a calibration is performed may have a bearing on observed drifts. If the array was to be calibrated when the halves were apart one may notice gain drifts once the halves have been moving to their normal operating positions. This may due to the fact that air flow across the detectors, and therefor temperature, is different when the array is opened as compared closed. The consequence of this is that all calibrations should be done with the array as close to it's

normal operating position as possible. Also, all pumps that are normally operating during a run should also be turned on during calibration. Because there may be seasonal weather changes during one running period and the next it is suggested that the calibration should be checked before each new run period and if possible and regular intervals during the run period.

### C.3.2 Operating Voltages

As discussed in Chapter 4, the voltage applied to the PMT's is proportional to the gain of the detectors. The gain matching program discussed in Section 8.1 is dependent on the fact that any extrapolation and interpolation of gains to the required value is a linear dependency. The PMT's do respond linearly in a certain range but outside this range will deviate slightly from this approximation. It has been observed that when calibrating the array a more reliable result is achieved when the calibration ratio is such the on average all detectors operate at voltages around 1000 V. As an example, the calibration ratio giving 100 channels/MeV sets the PMT voltages to values averaging around 1500 V. When the gain matching program interpolates or extrapolate for this ratio the user may find that the match is not entirely satisfactory whereas a ratio giving 50 channels/MeV does provide an excellent match. This is probably due to the fact the voltage to gain ratio is outside the linear range. Voltages set for the higher ratio may also show more extreme drifts if the response of the detectors is now non linear. More study is intended for this issue. It should also be considered if difficulties are encountered in pre-run gain calibration.

# Appendix D

## Sample Code

### D.1 Sample .FFCARDS GEANT Input File

```
GHEX Photon Detector Monte Carlo: P.G.
C
LIST
C
C **** Geant FFKEYs: see GEANT manual for more details ****
C
C ===== RUNG: IDRUN IDEVT [1,0]
C == IDRUN ==    User run number
C == IDEVT ==    User event number
C
RUNG 111 0
C
C ===== TRIG: NEVENT =====
C
C == NEVENT ==    Number of events to be processed
C
TRIG 1
C
C ===== TIME: TIMINT TIMEND ITIME      =====
```

```

C == TIMINT == Time used for initialization
C          NOTE: FFCARD input for TIMINT is ignored/overwritten
C == TIMEND == Time required for termination [10.]
C == ITIME  == Test every ITIME events
C          NOTE: User must optimize TIMEND/ITIME so that ITIME is
C                as large as is save! - Program termination is
C                initiated as soon as the time left on a particular
C                queue is smaller than TIMEND.
TIME 0.0 100. -1
C
C ===== RNDM: NRNDM(1) NRNDM(2) =====
C
C == NRNDM == Initial value of random number seeds NRNDM(1), NRNDM(2).
C          If NRNDM(2) is 0, the independent sequence NRNDM(1) is used.
C          If NRNDM(1) is 0, the default sequence is used. (9876, 54321)
C
RNDM 1432742791 1138921113
C ===== HADR: IHADR =====
C
C          0 = no hadron interactions effect
C          1 = hadron interactions with generation of secondaries (default)
C          2 = same without generation of secondaries
C
C          GHEISHA hadronic shower code if IHADR = 1
C          FLUKA   hadronic shower code if IHADR = 4
C          FLUKA/MICAP had. shower code if IHADR = 5
C
HADR 0
C
C ===== ANNI: IANNI =====
C
C          0 = no positron annihilation effect
C          1 = positron annihilation with generation of secondaries

```



```

C          2 = same without generation of secondaries
C
ANNI 1
C
C ===== BREM: IBREM =====
C
C          0 = no bremsstrahlung
C          1 = bremsstrahlung with generation of secondaries
C          2 = same without generation of secondaries
C
BREM 1
C
C ===== PFIS: IPFIS =====
C
C          0 = no resonant photon absorption/photonfission
C          1 = photonfission with generation of secondaries
C          2 = resonant photon absorption/photonfission without secondaries
C
PFIS 2
C
C ===== SCNT: ISCNT =====
C
C          0 = no scintillation process enabled
C          1 = scintillation process enabled
C          2 = (limited) scintillation process [1% of yield]
C
SCNT 0
C
C ===== YILD: PHOTON_YIELD RESOLUTION_SCALE =====
C
C          photon_yield      = scintillation photons/MeV deposited energy
C          resolution_scale = > 1.0 => resolution worse than statistical
C

```

```

YILD 10000.0 1.0
C
C ===== THLD: TOT_THRSHLD PMT_THRSHLD =====
C
C      tot_thrshld = threshold on the total number of photons
C                      detected in all PMTs
C      pmt_thrshld = threshold on the number of photons detected
C                      in each PMT (only the PMTs above pmt_thrshld
C                      contribute to the sum to which tot_thrshld is
C                      applied, and only those PMTs are used in the
C                      reconstruction)
C
THLD 0.0 0.0
C
C *** The ENERGY RANGE of the cross section and energy loss tables can
C      be fixed by the user with the new data card :
C          'ERAN'   EKMIN  EKMAX   NKBIN
C      which defines nkbin bins from Ekmin to Ekmax in a logarithmic scale.
C      The default is, as before, 90 bins from 10 Kev to 10 Tev but in
C      logarithmic scale. NKBIN must be 50<NKBIN<200.
C
ERAN 0.00001 10.0 180
C
C *** GEANT 3.21 global Cerenkov photon production flags
C
C ===== CKOV: ITCKOV =====
C
C == CKOV = 0 No Cerenkov photon production [0]
C == CKOV = 1 Sequential parent particle tracking
C == CKOV = 2 Interrupted parent particle tracking
C
CKOV 0
C

```

```

C ++++++
C
C      **** Geant User FFKEYs for debugging purposes ****
C
C ===== DEBU: IDEMIN IDEMAX ITEST =====
C == IDEMIN == First event to debug. If negative the debug flag IDEBUG
C              is set for the initialization phase
C == IDEMAX == Last event to debug.
C == ITEST == Print control frequency (for all events!)
C
DEBU -1 100000 1000
C
C      *** The convention for GDEBUG is followed (see GEANT manual) ***
C
C == ISWIT(1) = 2: the content of the temporary stack for secondaries in
C                  the common /GCKING/ is printed;
C == ISWIT(2) = 1: the current point of the track is stored in the JDXYZ
C                  bank via the routine GSXYZ;
C                  = 2: the current information on the track is printed via
C                  the routine GPCXYZ;
C                  = 3: the current step is drawn via the routine GDCXYZ;
C                  = 4: the current point of the track is stored in the JDXYZ
C                  bank via the routine GSXYZ. When the particle stops
C                  the track is drawn via the routine GDTRAK and the
C                  space occupied by the track in the structure JDXYZ
C                  released;
C                  = 5: print GEANT vertex information via GPVERT at the end
C                  of the event (in GUOUT)
C == ISWIT(3) = 1: the current point of the track is stored in the JDXYZ
C                  bank via the routine GSXYZ;
C == ISWIT(4) = 0: write NO output information
C                  = 1: ASCII output for analysis to unit 22
C                  = 2: PAW Ntuple output : nt# 998, 999;

```

```

C
SWIT 0 0 0 0
C
C ===== HSTA: LHSTA
C == LHSTA ==   NHSTA names of required standard histograms
C
C HSTA 'TIME' 'SIZE' 'MULT' 'NTRA' 'STAK'
C
C ===== PRIN: LPRIN
C == LPRIN ==   NPRIN names of GEANT data structures to be printed
C
PRIN 'PART' 'MATE' 'TMED' 'VOLU' 'SETS'
C
C ===== RGET: LRGET
C == LRGET ==   NRGET names of GEANT data structures to fetch from RZ
C
C RGET 'INIT'
C
C ===== RSAV: LRSV
C == LRSV ==   NRSV names of GEANT data structures to fetch from RZ
C
C RSAV 'INIT'
C
C ++++++
C
C          ***** GBOX Photon Detector Run directives *****
C
C ===== KINE: IKINE PKINE(10) =====
C
C          (generation of photons)
C          -----
C KINE card:  IKINE      : number of photons at initial vertex (if > 0)
C              : GEANT particle type (if < 0)

```

```

C          -> 1: gamma, 2: e+, 3: e-, etc.          *
C          PKINE 1 : x of photon origin distribution [cm] *
C          2 : y of photon origin distribution [cm] *
C          3 : z of photon origin distribution [cm] *
C          4 : half length of photon origin x-dimension [cm] *
C          5 : half length of photon origin y-dimension [cm] *
C          6 : half length of photon origin z-dimension [cm] *
C          PKINE 7 : particle energy [MeV]          *
C          8 : theta [degree]                      *
C          9 : phi [degree]                        *
C          10 : emittance [mrad]                   *
C
C KINE -2 0.0 0.0 0.0 0.0 0.0 0.0 4.44 0.0 0.0 0.0
C KINE 2 0.0 0.0 0.0 0.0 0.0 0.0 0.511 0.0 0.0 0.0
KINE 1 0.0 0.0 0.0 0.0 0.0 0.0 4.44 0.0 0.0 0.0
C
C ===== EGAM: egamma(10) =====
C
C          egamma(i) == energy of ith gamma [MeV]
C
C EGAM 3.44 1.0
C
C
C ===== DMAT: n_detmate =====
C DMAT 8 is NaI
C DMAT 10 is BGO
DMAT 10
C
C ===== FSID: s_finger z_finger air_gap d_air(1) d_air(2) d_mtl =====
C
C          s_finger == side of scintillator finger [cm]
C          z_finger == length of scintillator finger [cm]
C          air_gap == air gap between hexagons [cm]

```

```

C          d_air(1) == MGO gap/film around the finger side [cm]
C          d_air(2) == MGO gap/film around the finger front [cm]
C          d_mtl    == metal/aluminium sheet thickness [cm]
C
FSID 5.588 7.620 0.1270 0.0355 0.3175 0.0635
C
C ===== WALL: wall(3) =====
C
C          wall(1) == steel    beam box wall thickness [cm]
C          wall(2) == aluminum beam box wall thickness [cm]
C          wall(3) == pumping collimator wall thickness [cm]
C
WALL 0.1 0.3175 0.4978
C
C ===== BGAP: box_width =====
C
C          box_width == 'pizza' box width [cm]
C
BGAP 5.08
C
C ===== HOLE: aprt =====
C
C          aprt == radius of beam pipe
C
HOLE 0.4496
C
C ===== MPMT: mtype_pmt =====
C
C          mtype_pmt == 1 : circular
C          mtype_pmt == 2 : square
MPMT 1
C
C ===== PMTR: pmt_size pmt_length =====

```

```

C
C          pmt_size  == half size or radius of PMT [cm]
C          pmt_length == length of PMT [cm]
C
PMTR 2.54 2.5
C PMTR 4.0 27.559
C
C ===== BLKA: bulk_absorption =====
C
C          bulk_absorption == bulk absorption coefficient of LSO [cm]
C
BLKA 100.0
C
C ===== REFL: paint_absorption =====
C
C          paint_absorption == 1-reflectivity
C
C          paint_absorption(1) - crystal sides/ends
C
REFL 0.11
C
C ===== ANAL: E_threshold
C
C          E_threshold == Energy threshold for Photo Peak Efficiency [MeV]
C
ANAL 2.22
STOP

```

## Appendix E

### The GEANT Shapes



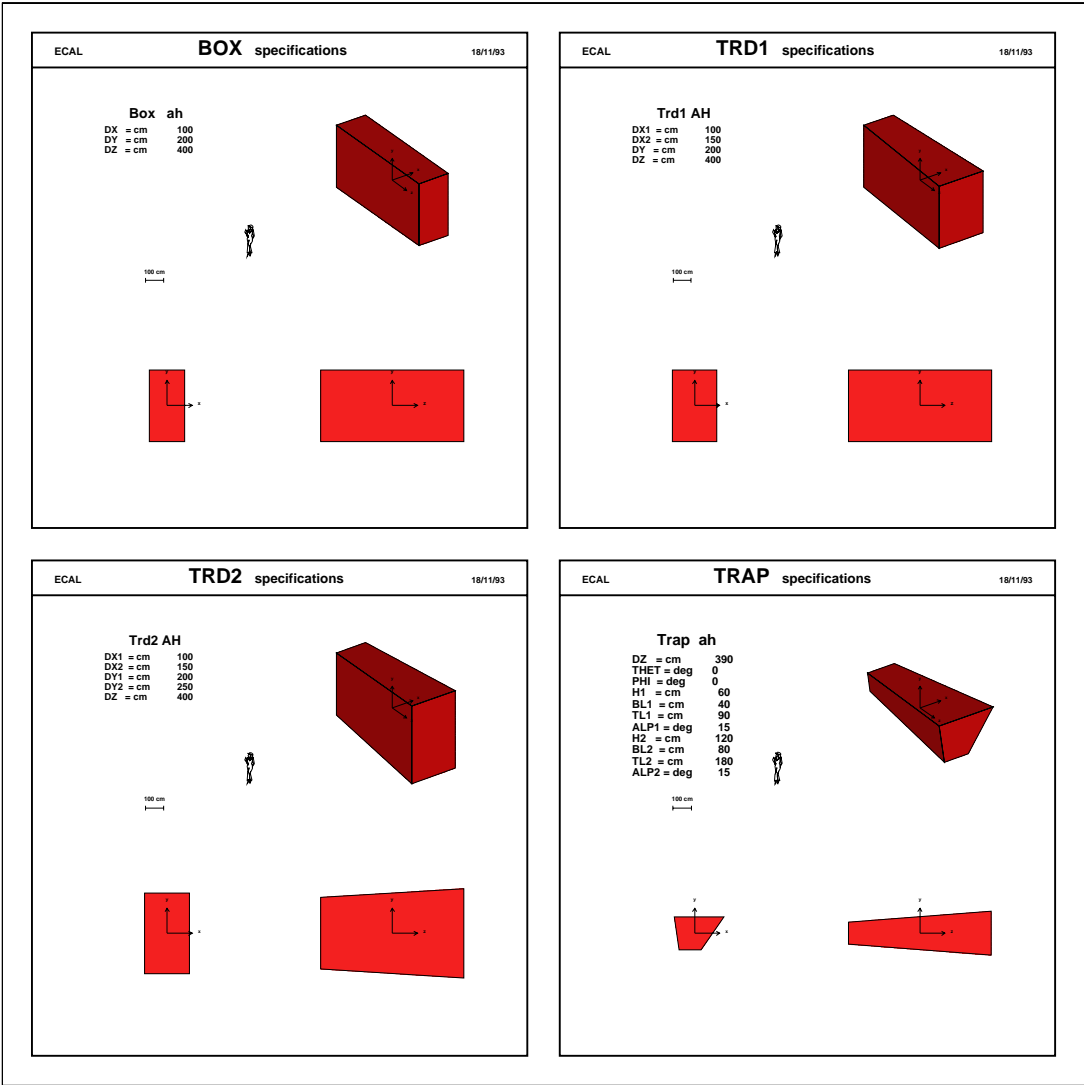


Figure E.1: BOX,TRD1,TRD2,TRAP

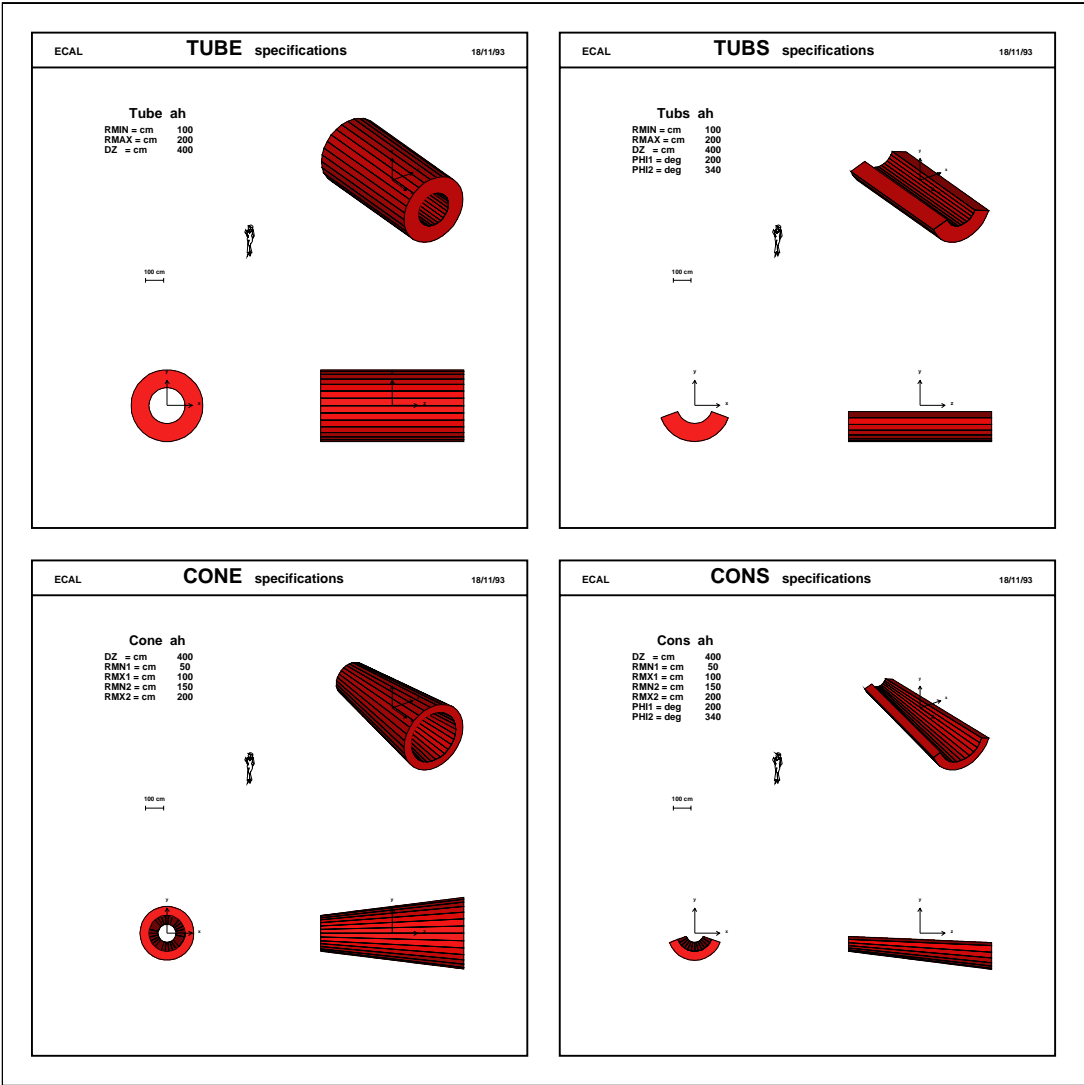


Figure E.2: TUBE,TUBS,CONE,CONS

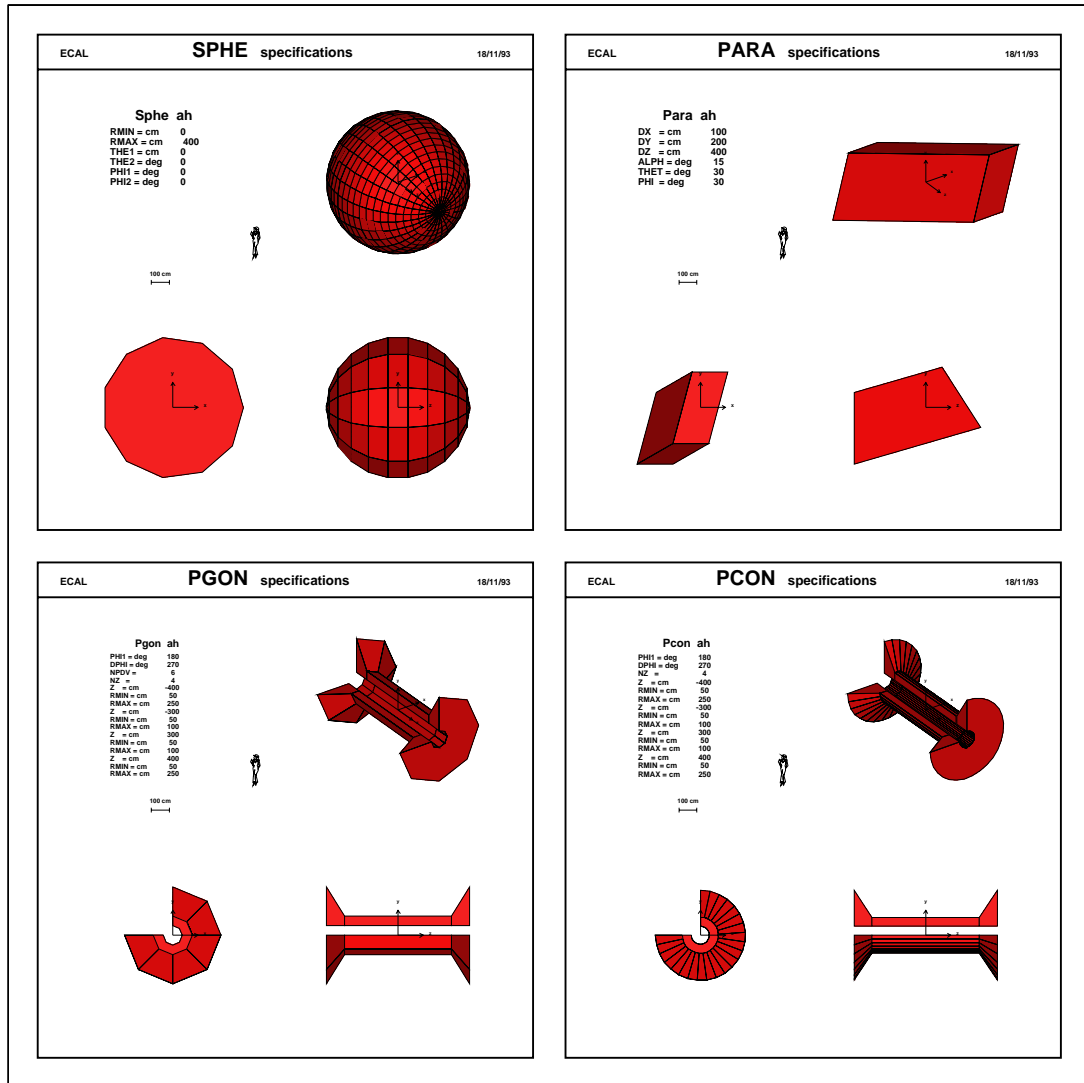


Figure E.3: SPHE, PARA, PGON, PCON

